Title
Improving a Priori Regional Climate Model Estimates of Greenland Ice Sheet Surface Mass Loss Through Assimilation of Measured Ice Surface Temperatures

Author
Navari, Mahdi

Publication Date
2015

Peer reviewed|Thesis/dissertation

UNIVERSITY OF CALIFORNIA

Los Angeles

Improving a Priori Regional Climate Model Estimates of Greenland Ice Sheet Surface Mass Loss Through Assimilation of Measured Ice Surface Temperatures

A dissertation submitted in partial satisfaction of the

requirements for the degree Doctor of Philosophy

in Civil Engineering

by

Mahdi Navari

2015

ABSTRACT OF THE DISSERTATION

Improving a Priori Regional Climate Model Estimates
of Greenland Ice Sheet Surface Mass Loss Through Assimilation of
Measured Ice Surface Temperatures

by

Mahdi Navari
Doctor of Philosophy in Civil Engineering
University of California, Los Angeles, 2015
Professor Steven Adam Margulis, Chair

The Greenland ice sheet has been the focus of climate studies due to its considerable impact on sea level rise. Accurate estimates of surface mass balance components - including precipitation, runoff, and evaporation - over the Greenland ice sheet would contribute to understanding the cause of the ice sheet's recent changes (i.e., increase in melt amount and duration, thickening of ice sheet interior, thinning at the ice sheet margins) and help to forecast future changes. Deterministic approaches provide a general trend of the surface mass fluxes, but they cannot characterize the uncertainty of estimates. The data assimilation method developed in this dissertation aimed to optimally merge the satellite-derived ice surface temperature into a snow/ice model while taking into account the uncertainty of input variables. Satellite-derived ice surface temperatures were used to improve the estimates of the Greenland ice sheet surface mass fluxes.

Three studies were conducted on the Greenland ice sheet. The goal of the first study was to provide a proof of concept of the proposed methodology. A set of observing system simulation experiments was performed to retrieve the true surface mass fluxes of the Greenland ice sheet. The data assimilation framework was able to reduce the RMSE of the prior estimates of runoff, sublimation/evaporation, surface condensation, and surface mass loss fluxes by 61%, 64%, 76%, and 62%, respectively, over the nominal prior estimates from the regional climate model. In the second study, satellite-derived ice surface temperatures were assimilated into a snow/ice model. The results show that the data assimilation framework was capable of retrieving ice surface temperatures with a mean spatial RMSE of 0.3 K which was 69% less than that of the prior estimate without conditioning on satellite-derived ice surface measurements. Evaluation of surface mass fluxes is a critical part of the study; however, it is limited by the spare amount of independent data sets. Several data sets were used to investigate the feasibility of verification of results. It was found that predicted melt duration is in agreement with melt duration from passive microwave measurements; however, more efforts are needed to further verify the results. In the third study, the feasibility of microwave radiance assimilation was investigated by characterizing the error and uncertainty in predicted passive microwave brightness temperature from the radiative transfer model. We found significant uncertainty between the predicted measurement and satellite-derived passive microwave brightness temperature due to error in snow states, coarse resolution of the passive microwave and also an imperfect coupled snow/ice and radiative transfer model. Based on our findings, radiance assimilation requires more accurate snow grain size parameterization to take into account temporal and spatial variability of snow grain size. Furthermore, coarse resolution of both passive microwave brightness temperature and snow/ice model and attribute uncertainties of both predicted and measured brightness temperature make the radiance assimilation unattractive.

This research demonstrates that ice surface temperature measurements have valuable information that can be extracted by a data assimilation technique to improve the estimates of the Greenland ice sheet surface mass fluxes.

The dissertation of Mahdi Navari is approved.

William W. Yeh

Keith D. Stolzenbach,

Laurence Smith

Marco Tedesco

Steven Adam Margulis, Committee Chair

University of California, Los Angeles

2015

DEDICATION

I would like to dedicate my dissertation to my parents who thought me to work hard and to my wonderful wife who support me and always encourage me to pursue my goals.

Table of Contents

ACKNOWLEDGMENTS

I would like first of all to acknowledge my adviser Steve Margulis for his consistent support and instruction and guidance throughout my Ph.D. It has been an honor and privilege to work with him and learn from him. I owe gratitude to PI of my project and a committee member Marco Tedesco for his comments on my publication and dissertation. I would like to thank William Yeh, how support my Ph.D. application. I would like to thank my committee members William Yeh, Keith Stolzenbach, and Laurence Smith for all of their time, advice and constructive comments. Thanks to Christian Matzler, Samuel Morin (Météo-France) and Dorothy Hall (NASA Goddard Space Flight Center) for input on the MEMLS, CROCUS model and IST product. Thanks to my professors, Steve Margulis, William Yeh, Terri Hogue, Don Kendall, Sayed M. Bateni, Kuo-Nan Liou, David Neelin, Yongkang Xue. Thanks to my wonderful former and current officemates how provided great support both academically and socially including: Manuela Girotto, Laurie Huning, Gonzalo Cortés, Elisabeth Baldo, Brianna Pagán, Zelalem Mekonnen, Rike Becker, Che Chuan Wu, James McPhee, Solomon Demissie, Xinyue Li, Akash Kappa, David Navar. Thanks to the National Science Foundation under Grant Numbers 0909388 for providing financial support toward the realization of this dissertation.

MAHDI NAVARI

Department of Civil and Environmental Engineering 5732, Boelter Hall
UCLA, Los Angeles, CA 90095, 949-502-1694
E-mail: navari@ucla.edu

EDUCATION

University of California Los Angeles
Ph.D. candidate, in Civil Engineering — Expected Dec. 2015

Sharif University of Technology, Tehran, Iran
Master of Science, in Water Resources — Dec. 2001
Bachelor of Science in Civil Engineering — Sep. 1998

RESEARCH EXPERIENCE

UCLA, Department of Civil and Environmental Eng., Graduate Student Researcher
Sep. 2010-Present

Adviser: Professor Steven A. Margulis
Developed and implemented an Ensemble Batch Smoother data assimilation framework to integrate MAR-CROCUS outputs with ice surface temperature to generate a posterior reanalysis estimates of the Greenland surface mass fluxes. The developed framework includes the following tasks: 1) Modified the surface module CORCUS, 2) Programmed and implemented Ensemble batch smoother and Ensemble particle smoother, 3) Processed land surface temperature, albedo, ice surface temperature, and Brightness temperature, 4) Implemented the radiative transfer model, MEMLS, to transfer the snow states to brightness temperature, and 5) Parallelized the algorithm to be executable over the UCLA cluster

PUBLICATIONS

Navari M., Margulis, S.A., Bateni S.M., Tedesco M., Alexander P., Fettweis X., 2015, "Feasibility of improving a priori regional climate model estimates of Greenland ice sheet surface mass loss through assimilation of measured ice surface temperatures", Accepted as a discussion paper in The Cryosphere (TCD).
Navari M., Margulis, S.A., Bateni S.M., Tedesco M., 2015, "Characterization of the Greenland Ice Sheet Surface Mass Balance via assimilation of Ice surface temperature into the CROCUS snow ice model", in Preparation.
Navari M., Bateni S. M., Margulis S., Alexander P., Tedesco, M. 2013, "Estimating Greenland Ice Sheet Surface Mass Balance Using a Novel Data Assimilation Framework: An Observing System Simulation Experiment", AGU
Navari M., Bateni S. M., Margulis S., Alexander P., Tedesco, M., 2012, "Characterizing Greenland ice sheet surface mass balance via assimilation of spaceborne surface temperature, albedo, and passive microwave data into a physically-based model" , AGU
Patrick M Alexander, Marco Tedesco, Xavier Fettweis, Steven A Margulis, **Navari** M., Jason E Box, Christine Chen, 2012,"Assessment of modeled albedo and bare ice extent (2001-present) in the regional climate model MAR using satellite data", AGU
Ataie-Ashtiani B., **Navari**.M, 2003, "Influence of Seaward Boundary Geometry on Seawater Intrusion in Coastal Aquifers", International Conference on Soil and Ground Water Contamination and Cleanup in Arid Countries, Sultan Qaboos University, pp. 17.

TEACHING EXPERIENCE

UCLA, Department of Civil and Environmental Engineering
Introduction to Water Resources Engineering — **Winter 2013, and 2014**
Responsible for teaching weekly recitation sections, preparing homework solution, and tutorial for water distribution piping system (EPA-Net). Responsible for helping students for their design project.

Applied Numerical Computing and Modeling Lab instructor — **Spring 2013**
Responsible for teaching lab sessions, preparing lab materials, lab assignments, holding office hour, and grading the exams. Taught Matlab as an advance tool to enhance the student capability to solve the numerical problems.

Introduction to Hydrology **Fall 2013, and 2014**
Responsible for teaching weekly recitation sections, preparing weekly homework and solution, holding weekly office hour. Taught Matlab and helped student to use Matlab functions available in the "MOdular Distributed Watershed Educational Toolbox (MOD-WET)" to enhance students learning about different hydrological processes. Developed the Muskingum-cunge channel flow routing subroutine for the MOD-WET toolbox.

Hydraulic and Hydrologic Design **Spring 2014**
Responsible for teaching design concepts related to the course projects and consulting students to come up with an optimum design. The course included designing drinking water well, distribution pipeline system and also using rainfall-runoff model (HEC-HMS) to simulate the hydrological processes in a watershed and designing stormwater detention basin and outlet structures.

TECHNICAL SKILLS

Programming languages
MATLAB, R, FORTRAN, C-shell, Payton
Models and Software packages
CROCUS, MEMLS, MOD-WET, SSiB, MRT, 6S radiative transfer model, SACSMA, EdGCM, MODFLOW, , HEC-HMS, EPA-NET, Panoply, ABL-model, Hydrologic MODel (HyMOD), FEMWATER
Processing remote sensing and model output
Processed and used MODIS IST, LST, albedo, brightness temperature, surface reflectance, and Landsat surface reflectance. Processed and used meteorological data and products from regional climate model (MAR), Shuttle Radar Topography Mission (SRTM), PERSIANN-CCS, and NCEP Stage IV radar data
Algorithms
Diurnal amplitude variation (DAV), Shuffled Complex Evolution algorithm (SCE), Generalized likelihood uncertainty estimation (GLUE), Machin learning techniques (i.e. regression, logistic regression, K-mean clustering, PCA, neural network)

WORK EXPERIENCE

Mahab Ghods Consulting Engineering Co, Environmental Division, Tehran, Iran **2007-2009**
Integrated Water Resource Management in Iran, (Caspian Sea and Urumeye lake water basin) 2008-2009
- Worked with the project manager to plan and organize the related tasks
- Conducted meeting and training for the project engineers to fulfill the project requirements
- Quantified pollution from both point and distributed sources over the different sub-basins

Environmental impact assessment of material handling of Almahdi Alumina factory 2007-2008
- Conducted monthly based meeting with the client
- Provided the monthly progress report
- Worked closely with the project engineers to provide guidelines and direction for different part of the project and discuss about the challenges
- Reviewed and edited the project reports, documents, and drawings

Sazeh Pardazi Iran Consulting Engineers Co, Tehran, Iran **2001-2007**
Preparation of Shoreline and Environmental management plan for Kish Island 2006-2007
- Interviewed different stakeholders to understand their needs and requirements
- Worked with the project team to map current land use and plan for future development based on stakeholder need and feedback

Several port development studies 2001-2007
- Designed approach channel depth and width
- Designed number of berth, berth length and depth
- Designed maximum vessel DWT, TEU

LANGUAGES

Farsi (Native), English (Fluent)

1 Introduction

1.1 Background

Climate change is one of the greatest challenges of recent decades as it directly impacts the polar ice sheets and eventually sea level rise. The polar ice sheets hold enough water to raise sea level between 70-80 meters (e.g., IPCC, 2001; Schutz, 1998) and Greenland (Figure 1.1) alone contains 10 percent of the total land ice volume; which could potentially increase the sea level 7.2 meters (IPCC, 2001). A recent study showed that the global sea level has risen by an average rate of 2.9±0.4 mm/year during 1993 to 2014 (e.g., Watson et al., 2015). Using tide-gauge data during 1950 to 2000, Church and White (2006) showed that sea level rise has accelerated since 1993. Several factors can significantly influence sea level rise including ocean thermal expansion, plate tectonics, and most importantly melting of polar ice or high latitude ice caps. The key question is how to quantify the contribution of the polar ice sheets to mean global sea level rise. Accurate estimates of the polar ice sheets mass balance (MB: the net gain or loss of mass of an entire glacier over a certain time period, commonly a year) would begin to address this question and determines the contribution of the Greenland Ice sheet (GrIS) and the Antarctica Ice Sheet to mean global sea level rise.

Mass losses through ice dynamics (i.e., ice discharge from outlet glaciers) and surface mass balance (SMB: the net mass gain or loss of the ice sheet surface layers during one year) are two contributing mechanisms to the GrIS total mass loss. A recent study suggested that the mass loss via surface processes (i.e., SMB) accounts for about 70% of the GrIS's total mass loss (Enderlin

et al., 2014). Therefore, accurate estimates of surface mass fluxes could be used as input to net mass balance estimates and ultimately a sea level rise projection.

Early studies on the Greenland SMB components (i.e., precipitation, runoff, evaporation, sublimation, and condensation) dates back to early 1900s, during scientific expeditions wherein the main focus was on meteorological and geological measurements. Later in the 1990s, mathematical models began to play an important role in the GrIS climate studies (e.g. Reeh 1991). Parallel to modeling efforts, which began in the late 1970s, advances in remote sensing technology have significantly improved our understanding of ice sheet processes particularly in remote areas such as the Antarctica, Arctic, and Greenland.

In situ measurements from different sources (e.g., meteorological stations, glacio-meteorological expeditions) have provided opportunities to explore, verify, and validate models and remotely sensed products as well as retrieval algorithms. However, it should be noted that due to extreme climate conditions, darkness during winter time, instability and inaccessibility of the GrIS ablation zone, and high cost for installing and maintaining measuring stations, in situ measurements are limited and sparse. It is clear that these sparse in situ measurements cannot capture the spatial variability of the surface mass fluxes. Regarding this inability, surface remote sensing data/products suggest a further possibility to study mass balance.

Surface remote sensing data/products have been widely used to characterize certain aspects of the SMB (i.e. melt extent and duration (Tedesco et al., 2013; Hall et al., 2013), and model

verification (Fettweis et al., 2005; 2011). Indirect and implicit links between surface remote sensing (i.e., passive microwave, visible, and near-infrared) and the SMB terms make interpretation of these data difficult. For example, land surface temperature and passive microwave measurements can detect the melt signal, but they fail to quantitatively estimate the melt flux. Albedo products can detect new snow but cannot quantify snow accumulation. Saturation of passive microwave signals due to the presence of water in snowpack makes it impossible to diagnose whether water is refreezing or generating runoff. In addition, different components of SMB such as evaporation, condensation, sublimation, and runoff cannot be directly sensed. In any case, satellite-based observations suffer from uncertainties due to lack of perfect retrieval algorithms and the coarse spatial and temporal resolution of many data and products and such uncertainties should also be accounted for.

Using a simple model based on the degree-day method, which estimates the surface melt as a function of surface air temperature, was an early attempt to estimate the GrIS SMB using numerical models (e.g., Reeh 1991; Braithwaite and Olesen 1990). Developing more complicated energy balance models, which take into account the shortwave and longwave radiation, turbulent fluxes, and albedo parameterization has provided more reliable estimates of surface mass fluxes (e.g., Van de Wal and Oerlemans 1994). The advent of regional climate models (RCMs) was a key development in the study of remote areas like Greenland (e.g., Lefebre et al., 2003; Fettweis et al, 2005; Ettema et. al., 2009; Bromwich et al., 2001). The RCMs are physically-based models that dynamically downscale general circulation models

(GCMs) to provide a connection between larger scale models and observations. Modeling frameworks provide the ability to estimate the general trend of the surface mass and energy balance components over the GrIS. Physically based distributed models provide information about physical parameters such as snow grain size (used to estimate albedo), the density of snow/ice layers, surface temperature, and snow temperature profiles. These models can be used to analyze uncertainties related to states and fluxes based on model input uncertainties and also support assimilation techniques. Despite these advantages, fully coupled models still suffer from errors related to forcing and initial condition as well as modeling errors, which lead to significant uncertainties in the GrIS surface mass fluxes. A comprehensive comparison between the surface mass fluxes from different modeling frameworks has been provided in Fettweis (2007). Therefore, it is imperative to bring as many relevant data streams to bear on the problem of better spatial/temporal characterization of SMB. This dissertation is trying to fill some of these gaps and limitations (explained above) with respect to the GrIS SMB by extracting useful information from relevant surface remote sensing data streams through a rigorous data assimilation technique.

1.2 Motivation and science questions

In many of the previous studies, modeling methods, and remote sensing techniques have been mostly used individually to characterize the GrIS SMB or some aspect of the SMB. The sparseness of in situ data, coarse resolution of most satellite data/products, and considerable bias/uncertainty in modeling approaches are the main limitations of deterministic methods

causing less reliable estimates of SMB. To overcome the limitations of deterministic approaches and improve the ability of mapping, quantifying, and assessing SMB of the GrIS, innovative applications that integrate remote sensing measurements and modeling tools are needed.

Probabilistic approaches, such as data assimilation, can provide a rigorous framework for merging different sources of information in a consistent way to obtain an optimal SMB posterior estimate. Such an optimal merging can overcome the drawbacks of methods based solely on observation or modeling. It is hypothesized that additional information contained in surface remote sensing which has not been fully exploited in existing retrieval methods can be mined through the data assimilation process. It should be noted that data assimilation has already been used in some atmospheric models over the GrIS (e.g. Dee et al., 2011); however, such techniques have never been utilized with surface remote sensing datasets to improve the estimates of SMB over the GrIS and this is one key aspect of the proposed research.

The goal of this dissertation was to develop and test a new methodology that is capable of assimilating NASA earth observing system (EOS) data into a snow/ice model to improve the GrIS SMB estimates, better characterize and reduce the uncertainties and/or correct biases in the prior estimates of SMB, and gain a new insight into the SMB processes and their variability. In particular, the goal of this research was to evaluate the performance and information content of these data/products in the context of data assimilation. The following science questions provide a roadmap for the evaluation of the proposed methodology.

1. Can incorporation of remote sensing measurements overcome errors in the near-surface

meteorological forcing variables from a regional climate model?

2. To what extent do remote sensing data/products provide additional information to improve SMB estimates obtained from a regional climate model? And how does the information content vary by ice sheet zone (i.e. melt, percolation, and day snow zones)?
3. Do passive microwave measurements provide additional information that could improve SMB estimates?

The end results would not only prove valuable in addressing the questions described above, but should be useful to other scientists who are trying to address the current and future projections of sea level rise. The presented dissertation is therefore expected to promote better understating of the GrIS surface mass fluxes and underlying surface possesses.

1.3 Organization of the Dissertation

In chapter 2, the proposed methodology is evaluated in the context of an observing system simulation experiment using one-year synthetically generated ice surface temperature measurements with the temporal resolution of the satellite-derived ice surface temperature. In chapter 3, the methodology is applied to the satellite-derived ice surface temperature measurements to generate reanalysis estimates of the GrIS surface mass fluxes. Chapter 4 is an effort to understand and characterize errors and uncertainties associated with passive microwave predictions from radiative transfer models which is an important step in radiance assimilation. In Chapter 5, the major findings are summarized, and future directions for research are discussed.

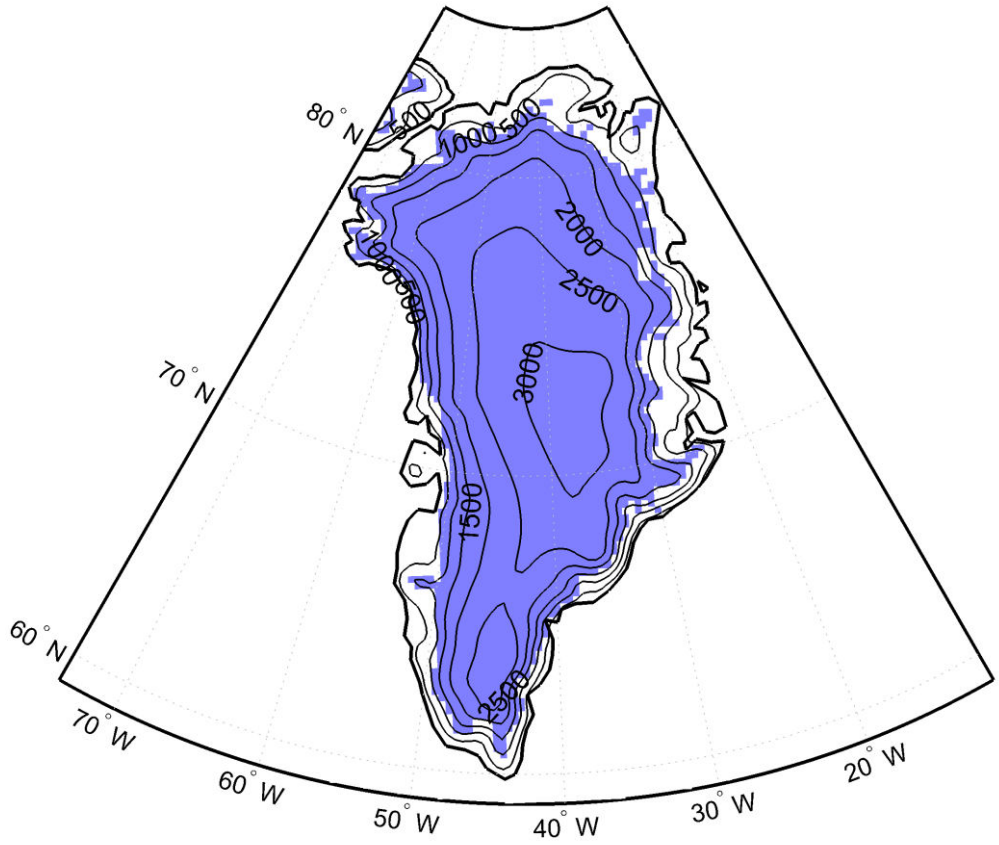

Figure 1.1 Greenland ice sheet mask and topographic contour

2 Feasibility of Improving a Priori Regional Climate Model Estimates of Greenland Ice Sheet Surface Mass Loss Through Assimilation of Measured Ice Surface Temperatures

2.1 Introduction and Background

The Greenland ice sheet (GrIS) has recently experienced thinning of the marginal ice (e.g. Straneo et al. 2013, Khan et al., 2014), thickening of its interior (e.g. Johannessen et al., 2005; Fettweis, 2007), acceleration and increase in ice discharge from many of Greenland's outlet glaciers (e.g. Rignot et al., 2008; Wouters et al., 2013), and enhanced surface melt (e.g. Tedesco et al., 2013; Vernon et al., 2013). The melting of the GrIS due to increased temperature has the potential to affect deep ocean circulation, and sea level rise (Hanna et al., 2005; Fettweis et al., 2007; Tedesco 2007, Rahmstorf et al., 2015). Van Angelen et al. (2012) and Fettweis et al. (2013) predict that meltwater runoff will be the dominant mass loss process in the future due to the retreat of the tidewater glaciers above sea level; a recent study showing that the dynamic mass loss was reduced from 58% before 2005 to 32% for the period between 2009 and 2012 (Enderlin et al., 2014).

Many studies (e.g. van de Wal et al., 2012) have taken advantage of in situ measurements to provide a direct point-scale estimate of the surface mass balance (SMB, i.e. the difference between accumulation and ablation). However, with these limited in situ measurements alone,

large-scale mapping of the GrIS surface mass fluxes (i.e. precipitation, evaporation, sublimation, condensation, and runoff) is impossible. The availability of remote sensing data and/or products has taken GrIS from a remote ‘‘data poor’’ region that is reliant mostly on sparse in situ measurements to a potentially ‘‘data rich’’ environment. In this regard, a key research objective is to better understand how such data can be optimally leveraged for quantitatively estimating the surface mass balance (SMB) and its associated fluxes.

Surface remote sensing data and products (i.e., surface or skin temperature, multi-frequency brightness temperature, and albedo) have been used to characterize various aspects of SMB such as snow melt, melt extent, melt duration, new snow, extreme melt events (e.g. Abdalati and Steffen, 1995; Tedesco et al., 2011; Box et al., 2012; Hall et al., 2013). However, the relationship between surface remote sensing data/products and surface mass fluxes are most often indirect and implicit. For example, ice surface temperature can be indicative of melt, but it fails to quantitatively estimate the volume of meltwater produced. More importantly, other surface mass fluxes such as evaporation, condensation, sublimation, and runoff cannot be directly quantified via remote sensing. This makes the possibility of quantitatively characterizing the surface mass fluxes from remote sensing retrieval algorithms difficult if not impossible. It can therefore be argued that the information content of remotely sensed data remains underutilized due to indirect and implicit links between the various data streams and surface mass fluxes.

Given the limitations of the observation-based methods, numerical models offer an alternative mechanism to quantify the GrIS surface mass fluxes. Several model-based approaches

have been used to characterize the spatio-temporal variability of the GrIS surface mass fluxes in both historical and future contexts (e.g. Hanna et al., 2011,2013; Box et al., 2006; Fettweis, 2011; Ettema et. al., 2009; Lewis and Smith, 2009; Vernon et al. 2013; Franco et al. 2013). Although the aforementioned methodologies have provided the ability to estimate the GrIS SMB and related fluxes, their estimates vary considerably, mainly due to the different physics parameterizations in the models and simplifying assumptions, the inherent uncertainty of each method, error in model and input data, and the length of data records (e.g. Rignot et al., 2011; Vernon et al., 2013; Smith et al., 2015). Therefore, it is imperative to design techniques that bridge the gap between different methods by merging relevant data streams with a physical model with the aim of better spatial-temporal characterization of the GrIS surface mass fluxes. In this study, we provide an example of taking advantage of information in the relevant data streams to provide a better spatial-temporal characterization of the model outputs (i.e., the GrIS surface mass fluxes). This can be done using a data assimilation approach which attempts to merge model estimates with measurements in an optimal way (Evensen, 2009)."

2.2 Motivation and science questions

To date, to the best of the authors' knowledge, there have been no attempts at merging surface remote sensing data with models using a data assimilation (DA) framework to fully resolve and quantify estimates of the GrIS surface mass fluxes. Data assimilation techniques have been heavily used in hydrology to estimate soil moisture (e.g. Reichle et al., 2002; Margulis et al., 2002; Al-Yaari et al., 2014), predict snow water equivalent (SWE) (e.g. Durand et al., 2008;

De Lannoy et al., 2012; Girotto et al., 2014a; Zhang et al., 2014), estimate runoff (e,g. Crow and Ryn 2009; Franz et al., 2014), improve estimates of radiative fluxes (e.g. Forman and Margulis 2010; Xu et al., 2011), and characterize snowpack properties and freeze-thaw state of the underlying soil (Bateni et al., 2013, 2015). DA so far has been underutilized in applications aimed at characterizing GrIS dynamics. Recently, Goldberg and Heimbach (2013), and Morlighem et al. (2013) used variational DA methods to characterize the interior and basal properties of ice sheets and ice shelves. Larour et al. (2014) assimilated surface altimetry data into the reconstructions of transient ice flow dynamics to infer basal friction and surface mass balance of the northeast Greenland ice stream. However, the use of DA for estimating GrIS SMB terms remains relatively unexplored. Assessing the feasibility of such approaches in providing a mechanism for improving quantitative estimates of SMB is the key motivation of this work.

This study utilizes an observing system simulation experiment (OSSE) framework to assess the feasibility of the proposed DA system. The OSSE framework uses synthetically generated ice surface temperature (IST) measurements consistent with a "true" realization of SMB evolution. This study addresses the following science questions: 1) Can assimilation of IST measurements overcome errors and uncertainties in the near-surface meteorological forcing variables for snow/ice modelling? 2) Can a DA framework be used to reduce the uncertainty and/or correct biases in a priori estimates of surface mass fluxes from a regional climate model?

This paper is arranged as follows: Sect. 2.3 contains the description of the models and methods used in this work. The experimental design is given in Sect. 2.4. The results and

evaluation of the proposed methodology are discussed in Sect. 2.5. Finally, key conclusions and future research directions are reported in Sect. 2.6.

2.3 Models and Methods

2.3.1 Study domain

The study domain covers the entire GrIS, which is discretized with a grid size of 25 km by 25 km to match the domain used in the regional atmospheric model described below. The focus is on fully snow/ice covered pixels. Figure 2.1 shows the different GrIS mass balance zones based on a forward simulation for the year 2010. The ablation zone is defined as the region of the GrIS where the annual surface mass balance is negative. The dry snow zone is defined as the region where the mean annual temperature is less than -25ºC (Cuffey and Paterson 2010) and melt generally does not occur. The area between the ablation zone and the dry snow zone is considered the percolation zone where surface meltwater percolates downward into the snow layers. It should be noted that the digital elevation model (DEM) over the ice sheet originates from a high-resolution map generated by Bamber et al. (2001). The elevation of the ice sheet increases from almost zero in the coastal regions up to about 3400 m at the summit.

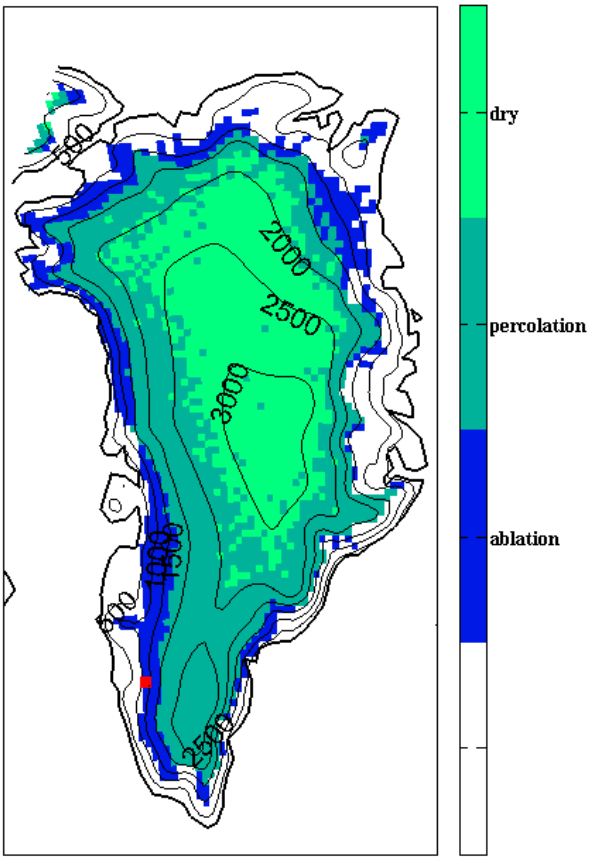

Figure 2.1 The Greenland ice sheet mask (filled area), including the ablation zone (blue), the percolation zone (dark green), and the dry snow zone (bright green) based on an offline CROCUS simulation for the year 2010. The contour lines show the topography of the ice sheet with an interval of 500 m. The red square show the location of pixel in the ablation zone where used to Figure 2.3

2.3.2 Data

Surface temperature plays an important role in the coupled GrIS surface energy and surface mass budget. It is the key factor that regulates partitioning of net radiation into the subsurface snow/ice, sensible and latent heat fluxes. Surface temperature also influences the generation of runoff, the temperature profile evolution, and even basal melt (Hall et al., 2013). Space-borne

instruments can provide estimates of IST. The retrieved IST is directly related to snow surface emissivity (Hook et al., 2007). The emissivity of the snow surface is a function of grain size and liquid water content, which both are under the influence of surface processes (Hall et al., 2009). These facts support the idea that clear-sky IST, of all remote sensing products available, may contain the most information about physical processes that drive the GrIS accumulation and mass loss. Therefore, this work focuses on testing the feasibility of using products such as Moderate Resolution Imaging Spectroradiometer (MODIS) IST as an extra source of information to enhance the utility of modelling techniques. The possibility of using additional remotely-sensed data streams (e.g. passive microwave brightness temperature and albedo) will be investigated in future studies.

The Greenland Ice Surface Temperature product (GrIS IST) is available from the MODIS Terra satellite (http://modis-snow-ice.gsfc.nasa.gov/?c=greenland) and provides up to one (clear-sky) measurement per day at a native resolution of 1.5 km and an accuracy of ~1° - 1.5°K (Hall et al., 2012). However, cloud contamination and occasional instrument outages play an important role in the availability of the MODIS IST measurements. These two factors along with some other technical and quality considerations can reduce the availability of the IST measurements to less than 10 high quality clear-sky measurements in some months (Hall et al., 2012). In the context of the OSSE used in this work, synthetic IST was generated based on the temporal resolution and acquisition time of the actual GrIS IST product by perturbing the modelled surface temperature with assumed measurement error described below.

2.3.3 Regional climate model

The a priori (or prior) estimate used in the DA framework in this study is based on output from the regional climate model Modèle Atmosphérique Régional (MAR; Gallée and Schayes (1994) and Gallée and Duynkerke (1997)). The version of the model used here (i.e. MARv2) has been applied extensively over the GrIS and is described in more detail in previous studies (Lefebre et al., 2003; Fettweis et al., 2005). This version has also been used to generate future projections for the ICE2SEA European project (Fettweis et al., 2013). For this study, MAR was used to generate hourly near-surface meteorological outputs (i.e., temperature, pressure, wind speed and direction, longwave and shortwave radiation, precipitation, pressure, humidity, etc.) at a horizontal spatial resolution of 25 km to force an offline snow/ice model. The ERA-Interim reanalysis from the European Centre for Medium-Range Weather Forecasts (ECMWF) was used to initialize the MAR meteorological fields at the beginning of the simulation (1979) and to force the atmospheric lateral boundaries as well as the oceanic conditions (surface temperature and sea ice extent) every 6 hours over 1979-2010. MAR was not reinitialized every day by the ECMWF reanalysis and its results were not recalibrated after the simulation to better compare with observations as in other approaches (e.g. Box et al., 2004; Box et al., 2006). The reader is referred to Fettweis et al. (2005), Lefebre et al. (2003) and Fettweis et al. (2011) for detailed information on the MAR setup used here.

2.3.4 Surface mass/energy balance and snow physical model

The key equations related to SMB are the water and energy balance of the near-surface ice

sheet. The bulk surface mass balance for each model pixel (i.e., integrated over the top ~10 meters of the ice sheet) can be written as:

$$SMB = P - E + C - R \tag{2.1}$$

where P is the surface precipitation, E is the surface evaporation/sublimation, C includes both liquid and solid condensation, and R is the meltwater runoff from the snow/icepack. Note that refreezing is implicitly included in the runoff term. Evaporation, sublimation, condensation and runoff are the key variables that drive the surface mass loss (SML), while precipitation is the key meteorological driver for GrIS surface accumulation.

The temporal evolution of snow temperature in a vertical snow column is constrained by the conservation of energy equation, i.e. (Brun et al. 1989):

$$\frac{\partial(\rho c_p T)}{\partial t} = \frac{\partial^2(\kappa T)}{\partial z^2} + q \tag{2.2}$$

where ρ is the snow density, c_p is the snow heat capacity, T is the snow temperature at depth z and time t, and κ is the snow heat conductivity, and q represents a sink (melt) and source (refreezing). It is worth noting that Eq. (2.2) is valid for T<273.15K; any energy inputs that would raise the temperature beyond freezing instead contribute directly to melt. Equation (2.2) is subject to the surface energy balance as a boundary condition, which is the key driver of the snowpack energy budget:

$$R_s^{\downarrow}(1-\alpha) + R_l^{\downarrow} - R_l^{\uparrow} = R_n = Q_{SH} + Q_{LH} + Q_G \tag{2.3}$$

where $R_s^{\downarrow}$ is the downward shortwave radiation, α is the (broadband) snow albedo, $R_l^{\downarrow}$ and $R_l^{\uparrow}$ are the downward and upward longwave radiation all terms are positive values. R_n is the net

radiation that is partitioned among the surface sensible (Q_{SH}), latent (Q_{LH}), and surface (Q_G) heat fluxes (into the snow). Q_{SH} and Q_{LH} are positive when directed toward the atmosphere and Q_G is positive when directed toward the snow/ice surface. The sensible/latent heat fluxes represent the turbulent heat/vapor exchange between the surface and overlaying air due to the temperature/water vapor gradient between the surface and the reference-level (i.e. meteorological forcing variables). The ground heat flux is driven by the temperature difference between the surface temperature and subsurface layers, and hence can have a significant impact on the ice/snow melt and runoff. Based on Eq. (2.3), $R_s^{\downarrow}$, $R_l^{\downarrow}$, α, and air temperature, specific humidity, and wind speed (embedded in Q_{SH} and Q_{LH}) are the key meteorological variables controlling the downward energy into the snowpack (Q_G), which ultimately contributes to runoff (R).

The above coupled surface mass/energy balance represented by the CROCUS snow physical model was used in this study to provide a prior estimate of the GrIS surface mass fluxes that is consistent with the nominal forcings provided by MAR. CROCUS is a 1D energy balance model consisting of a thermodynamic module, a water balance module taking into account the refreezing of meltwater, a turbulent module, a snow metamorphism module, a snow/ice discretization module and an integrated surface albedo module. CROCUS computes albedo and absorbed energy in each layer for three spectral bands (i.e. visible, and two near infrared bands). CROCUS derives the turbulent sensible and latent heat fluxes using a bulk method (Brun et al., 1989), which applies Monin-Obukhov similarity theory to estimate turbulent fluxes using the near-surface wind speed and the temperature and humidity differences between the surface and

the temperature at ~3 m, prescribed by MAR. CROCUS uses the bulk Richardson number to adapt the fluxes for stable and unstable atmospheric conditions, respectively. Note that a similar approach has been used by Van den Broeke et al., (2009). The capability of the model to partition the incident solar radiation between the layers allows melt occurs on multiple depths. In CROCUS each snow layer in the snow column is treated as a reservoir with a maximum water holding capacity of 5% of the pore volume. When the liquid water content (LWC) exceeds the threshold, excess water moves toward the layer below and the process continues until the water reaches the bottom layer and generates runoff. In addition, CROCUS takes into account changes in LWC due to snow melt, refreezing, and evaporation during a model time step. The physics of CROCUS and its validation are detailed in Brun et al. (1989, 1992).

Assimilation of data into an RCM is another option for attempting to improve RCM fields (such as precipitation, for example), but beyond the scope of this work. The focus of this work is improving of surface mass fluxes using RCM outputs and assimilation of a surface remote sensing data stream. Furthermore, the use of a fully coupled MAR-CROCUS system to generate an a priori ensemble estimate would be computationally prohibitive. To reduce the computational burden, an offline version of CROCUS was implemented (i.e., MAR was run over the whole modelling period, and then MAR outputs were used to force CROCUS over the same period). One can think of the DA framework outlined below as providing an update to an initial (prior) estimate of the surface mass fluxes from MAR (or any other regional climate model) using IST data as an additional constraint.

Of particular relevance to this study is the connection between CROCUS states and the measured variables used in the DA (i.e. IST). Surface temperature (synthetic IST) is an output of the forward model (CROCUS), therefore, it can directly be used as a prediction of the measurement in the DA system. One key aspect is that the raw measurements are available at higher spatial resolution than the model state (i.e. 1.5 km vs. 25 km). This was handled via an assumed change in the measurement error due to aggregation as described in more detail below.

2.3.5 Model adaptation

The CROCUS snow/ice model was originally developed for operational avalanche forecasting. Therefore, the model must be modified for SMB ice sheet applications. Following Fettweis (2006), the bottom boundary condition was modified for simulating approximately the top 10 meters of the ice sheets. In this context, this represents the "surface" mass and energy balance via the vertically integrated states and fluxes within these top layers of the ice sheet. This method consists of the following rules: First, if during the model integration the sum of the snow and ice layer heights becomes less than 8 m, the bottom layer is extended for two meters. Second, in the case that the sum of the snow and ice layer heights becomes larger than 15 m, the bottom layer is divided by two. This is consistent with the methodology used in nominal MAR simulations.

2.3.6 Ensemble Batch Smoother (EnBS) Framework

The EnBS is a technique that conditions a prior estimate of model states on measurements taken over an assimilation window to generate a posterior reanalysis estimate rather than a

real-time (or sequential) estimate (Girotto et al., 2014a; Bateni et al., 2013, 2015). In the context of this paper, the assimilation window is a full annual cycle and measurements consist of IST data over this period. Using the generated forcing fields from MAR, the CROCUS model was run forward in time to provide an ensemble of a priori estimates of snow/ice state variables (e.g. surface temperature, snow/ice layer temperature, density, grain size, etc.) and different surface mass fluxes (e.g. evaporation, sublimation, runoff, etc.). The propagation of the CROCUS model forward in time can be shown in state-space form as:

$$\boldsymbol{y}_j(t) = f(\boldsymbol{y}_j(\tau), \boldsymbol{u}_j(t), \boldsymbol{\beta}_j) \qquad (2.4)$$

where $\boldsymbol{y}_j(t)$ is the vector of states for the *j*th realization at time *t*, $f(.)$ represents the CROCUS model operator, $\boldsymbol{y}_j(\tau)$ is the vector of states at previous times (τ), $\boldsymbol{u}_j(t)$ is the forcing fields for realization *j*, and $\boldsymbol{\beta}_j$ is the model parameter vector for replicate *j*. Conventionally, the generated snow/ice states and surface mass fluxes by the forward propagation of CROCUS are called the open-loop (prior) estimates. Note that $\boldsymbol{y}_j(\tau = 0)$ represents the initial snow profile (IC: initial condition).

The main source of uncertainty in a priori snow/ice states and surface mass fluxes is hypothesized to be most likely due to errors in the meteorological forcings ($\boldsymbol{u}_j(t)$, see Eq. 2.4) generated by a parent model (in this case MAR): incoming shortwave and longwave radiation, air temperature ($\boldsymbol{T}_a$, which is implicit in the latent and sensible heat fluxes), precipitation, wind speed, relative humidity, and cloudiness. Herein, our focus is on the sub-set of key forcings that are the postulated main drivers of SMB (i.e., $\boldsymbol{P}$, $\boldsymbol{R}_l$, $\boldsymbol{R}_s$, and $\boldsymbol{T}_a$). It is hypothesized that the a

priori uncertainty in forcings can be modeled via:

$$\boldsymbol{P}_j(x,t) = \gamma_{P,j}(x)\boldsymbol{P}_{MAR}(x,t) \quad (2.5a)$$

$$\boldsymbol{R}^{\downarrow}_{s,j}(x,t) = \gamma_{S,j}(x)\boldsymbol{R}^{\downarrow}_{s,MAR}(x,t) \quad (2.5b)$$

$$\boldsymbol{R}^{\downarrow}_{l,j}(x,t) = \gamma_{l,j}(x)\boldsymbol{R}^{\downarrow}_{l,MAR}(x,t) \quad (2.5c)$$

$$\boldsymbol{T}_{a,j}(x,t) = \gamma_{T,j}(x)\boldsymbol{T}_{a,MAR}(x,t) \quad (2.5d)$$

where $\boldsymbol{P}_{MAR}(x,t)$, $\boldsymbol{R}^{\downarrow}_{s,MAR}(x,t)$, $\boldsymbol{R}^{\downarrow}_{l,MAR}(x,t)$, and $\boldsymbol{T}_{a,MAR}(x,t)$ are the nominal near-surface meteorological outputs from MAR, $\gamma_{P,j}(x)$, $\gamma_{S,j}(x)$, $\gamma_{l,j}(x)$, and $\gamma_{T,j}(x)$ are lognormally-distributed multiplicative coefficients designed to capture uncertainty in the forcing inputs. The subscript *j* represents an individual ensemble member sampled from the postulated uncertainty distribution ($j = 1,\ldots, N_e$, where N_e represents the ensemble size) and *x* shows the spatial index (i.e., implicitly represents an individual computational pixel in the domain). It should be noted that, a multiplicative lognormal perturbation model (e.g. Margulis et al., 2002; Andreadis and Lettenmaier, 2006; Forman and Margulis, 2010, etc.) was used since all forcing (i.e., $\boldsymbol{P}$, $\boldsymbol{R}_l$, $\boldsymbol{R}_s$, and $\boldsymbol{T}_a$ [ºK]) are positive quantities and it provides a simple mechanism for capturing the expected uncertainty in the inputs. This type of perturbation model characterizes the ensemble using the first two moments (i.e., mean and coefficient of variation (CV)) (Forman and Margulis 2010). In this study, the mean, CV, and cross correlation between the forcing variables was obtained using the reported values in De Lannoy et al. (2010, 2012). All of the parameters for each forcing are shown in Table 2.1.

Table 2.1 Postulated parameters (Coefficient of variation (CV) and cross-correlation) for multiplicative perturbations to hourly meteorological forcing inputs (the units for each forcing are: *P* in mm/hour, R_s and R_l in W/m^2 and T_a in K).

Perturbation	CV	Cross correlation			
		P	R_s	R_l	T_a
Precipitation (*P*)	0.5	1.0	-0.1	0.5	-0.1
Shortwave (R_s)	0.2	-0.1	1.0	-0.3	0.3
Longwave (R_l)	0.1	0.5	-0.3	1.0	0.6
Air temperature (T_a)	0.005	-0.1	0.3	0.6	1.0

Traditional DA applications are posed as state estimation problems where the vector of state variables (i.e., snow temperature, density, grain size, depth, etc.) is estimated via conditioning on measurements. In the current application, this can become prohibitive since the state vector dimension is extremely large (i.e., each snow state profile involves 50 layers with several states per pixel and several thousand pixels over the domain). More importantly, updated states do not provide quantitative information about surface mass fluxes. Hence, here we took a different approach. Rather than estimating the states directly, we treated the multiplicative coefficients $\gamma_{i,j}$ in Eq. (2.5) as the 'states' to be estimated. In other words, the multiplicative coefficients have been used to transfer the nominal MAR forcing into probabilistic space (i.e. prior and posterior forcings). The DA algorithm uses IST measurements to condition the probability density function (pdf) of the prior multiplicative coefficients to compute the posterior pdf of the multiplicative coefficients. This strategy, which was also used specifically for precipitation in Durand et al. (2008) and Girotto et al. (2014a), is in direct recognition of the fact that the primary source of uncertainty in surface mass fluxes is due to error in the near-surface meteorological forcing

inputs. The added benefit of this approach is that the size of the state vector is significantly reduced even in the case of time variant multiplicative states. Such a strategy derives a posterior estimate of the forcing variables directly (via the updated $\gamma_{i,j}$), and consequently allows for improved estimates of the surface mass fluxes via a posterior integration of CROCUS (with the posterior forcing inputs). The DA system theoretically allows the multiplicative states to vary on any arbitrary time scale. However, for simplicity, we implemented time-invariant perturbations (i.e., assumed $\gamma_{i,j}$ were unchanged over the annual modelling period) herein. In this way the update to the states was designed to allow for biases and/or low-frequency errors in individual realizations in the prior multiplicative states.

It would be ideal to characterize the uncertainties for all inputs from the information content in the assimilated data stream(s). However, in many cases available measurements are not relevant to some sources of uncertainty in the models. For instance, in this study, IST is less likely to have information about precipitation because there is no expected meaningful correlation between precipitation and IST. With regard to the fact that precipitation cannot be updated using the IST data the focus of this work has involved constraining the GrIS surface mass loss (SML) components (i.e., sublimation/evaporation, condensation, and runoff), while still including the expected uncertainty in the accumulation term (precipitation). In other words, all forcing inputs were perturbed to take into account their respective postulated uncertainties, but only longwave, shortwave and surface air temperature coefficients were updated as part of the assimilation system.

In the update step, the EnBS merges IST measurements with prior multiplicative states in order to generate a posterior estimate of those multiplicative states. In this study, we used an EnBS, which was implemented in a batch mode over a pre-defined window (i.e., applied over one year) with a single update. This feature of the EnBS (i.e., the batch mode update) allows running MAR and CROCUS in an offline mode that could be applied to the historical record. The open-loop (prior) estimate of the variables of interest (i.e., γ_S, γ_l, and γ_T) were collected into the state matrix Γ^-. Similarly, the vector of synthetically generated IST measurements was assembled into a vector:

$$\boldsymbol{T}_{measurement} = \boldsymbol{T}_{true} + \boldsymbol{v} \tag{2.6}$$

where $\boldsymbol{v}$ is the assumed additive white Gaussian error and $\boldsymbol{T}_{true}$ is the synthetic truth (see Sect. 2.4.1). Finally, each ensemble member was updated individually via a Kalman-type update equation (Durand and Margulis, 2008; Bateni et al., 2013, 2015),

$$\Gamma_j^+ = \Gamma_j^- + \boldsymbol{K}[\boldsymbol{T}_{measurement} + \boldsymbol{V}_j - \boldsymbol{T}_{predicted,j}] \tag{2.7}$$

where Γ_j^- and Γ_j^+ represent the *j*th ensemble member before and after the update, respectively, $\boldsymbol{T}_{predicted}$ is the matrix of predicted measurements consisting of predicted IST. $\boldsymbol{V}$ is the measurement error that was synthetically produced and added to the measurements in order to avoid correlation among the replicates (Burgers et al. 1998), and K is the Kalman gain matrix which is given by

$$\boldsymbol{K} = \boldsymbol{C}_{\Gamma T}[\boldsymbol{C}_{TT} + \boldsymbol{C}_V]^{-1} \tag{2.8}$$

where $\boldsymbol{C}_V$ is the error covariance of the measurements, $\boldsymbol{C}_{\Gamma T}$ is the cross-covariance between the

prior states and predicted measurements, and $\boldsymbol{C}_{TT}$ is the covariance of the predicted measurements. In this framework, the state variables are related to the measurements in the batch through the covariance matrices that are obtained from the ensemble.

The update in Eq. (2.7) can be seen as a projection of measurement-prediction misfits onto the states. The updated (posterior) multiplicative states were used in Eq. (2.5) to retrieve updated (posterior) forcing. The posterior forcings and initial snow profile (I.C.) were used as inputs in CROCUS to estimate the posterior surface mass fluxes. The proposed methodology can simply be extended to multiple years by applying the DA sequentially and independently for each year (e.g. Girotto et al., 2014b) or via applying the DA to a moving window (e.g. Dunne et al., 2005). A schematic illustration of the methodology is presented in Figure 2.2. The proposed methodology can be thought of as a post-processing (reanalysis) of MAR estimates by constraining the model using independent IST observations.

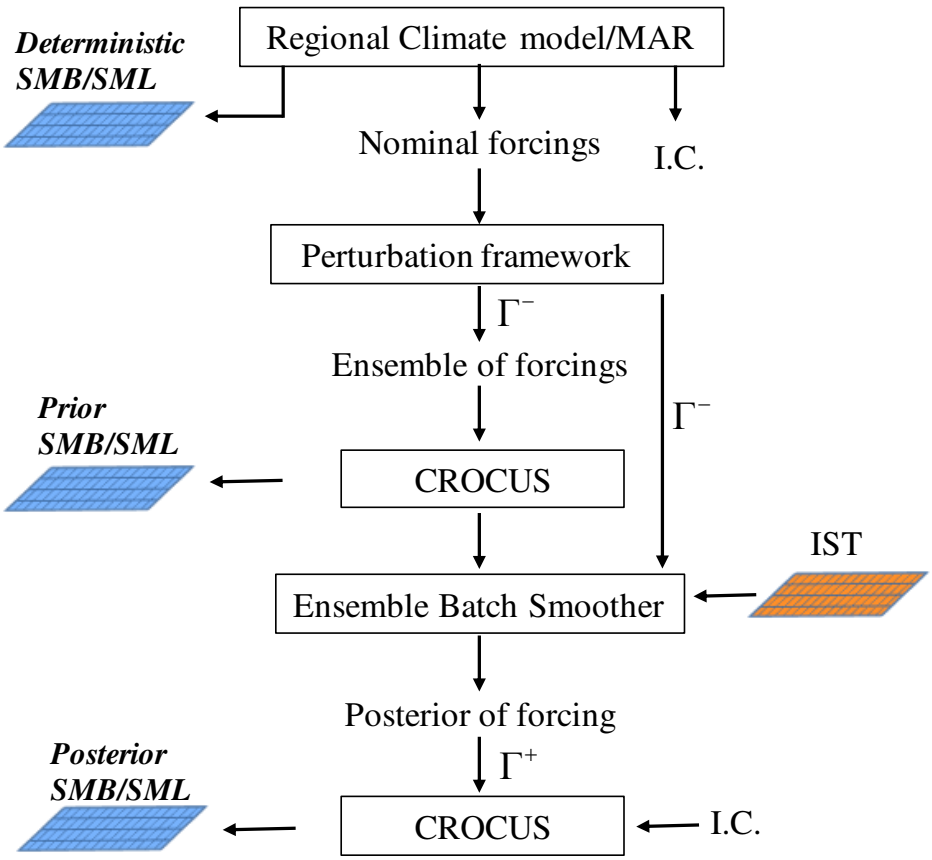

Figure 2.2 Schematic illustration of the proposed methodology. The posterior SMB/SML is effectively a post-processing (reanalysis) of regional climate model (in this case MAR) estimates conditioned on IST measurements.

2.4 Experimental Design

An OSSE or synthetic twin experiment offers a controlled setting in which the true forcing variables (i.e., γ_S, γ_l, and γ_T) are available. The goal of an OSSE is to evaluate the feasibility of the new methodology prior to assimilating real space-borne measurements. In an OSSE, a synthetic true state and corresponding noisy measurements of the system are generated and used to evaluate the feasibility of the DA framework (e.g. Durand and Margulis, 2006; Crow and Ryu, 2009; De Lannoy et al., 2010).

2.4.1 True selection

The synthetic truth uses realistic input and measurement error characteristics in conjunction with the forward models to generate a realistic realization of the true system. In this study, the synthetic truth was selected as an outlier (defined below) from the generated ensemble due to the fact that errors in forcings can yield differences between a forward model (open-loop) estimate and the true surface mass fluxes.

In the OSSE system, traditionally the synthetic true ensemble is chosen from state space trajectory of the forward model (e.g., Crow and Van Loon, 2006; Durand and Margulis, 2006; Bateni et al., 2013). While an alternative approach could involve choosing the synthetic truth from the trajectory space of another well developed RCM model, running multiple RCM models to generate a synthetic truth is prohibitive.

The ensemble of forcing data was generated via Eq. (2.5) for the year 2010 and then the offline CROCUS implementation was run using the ensemble of forcing data to generate estimates of the GrIS surface mass fluxes in 2010. The year 2010 was chosen, at least in part, since it was characterized by an extreme melt rate (Tedesco et al., 2011). Considering the fact that runoff is the main component of the GrIS surface mass loss, the true ensemble (synthetic truth) was selected in a way that the integrated true runoff over the GrIS was an outlier relative to the median of the ensemble simulations. The forcing variables, states, and fluxes corresponding to the synthetic truth were also considered as the true forcings, the true states and the true fluxes respectively. It should be highlighted that in a synthetic DA experiment, any generated

realization from the forward model (CROCUS) can be used as the synthetic truth, but one that is significantly different from the prior mean/median allows for a more robust assessment of the value of the assimilated measurements. In other words, in an OSSE the goal is to assess whether a DA framework can replicate the randomly selected true by merging the measurements with the prior (open-loop) estimates. It has been shown that (see Section 2.5.3) the proposed data assimilation algorithm is insensitive to the selected truth (i.e. runoff) and is capable of retrieving the true states and fluxes for different runoff scenarios.

2.4.2 Assimilated measurement characteristics

Surface temperature from the forward model can be considered as a close approximation of the remotely-sensed IST. Here, the synthetic DA experiments were designed to mimic reality as much as possible. Hence, the DA system was run with a realistic representation of the temporal frequency of real space-borne IST measurements; e.g. the GrIS IST measurements from MODIS have a daily temporal resolution. However, in many instances daily observations are not available due to cloud contamination, instrument outage, and quality related considerations. To take this issue into account, the number of available daily IST measurements (i.e., synthetic measurements) for assimilation in each month was derived from the spatial average seen in the actual Greenland IST product (e.g., Hall et al., 2012). The days with measurements were selected randomly so that the total number per month was consistent with the real number of available measurements.

Since the raw MODIS IST measurements are available at a much finer spatial resolution (i.e.

~1.5 km) than the model scale (25 km), the measurements themselves and their error characteristics would require a pre-processing spatial aggregation to match the resolution of computational pixels (~25 km). In the context of the OSSE in this study, the synthetic measurements and forward model both have the same spatial resolution therefore there is no need for spatial aggregation of the predicted measurement. However, specification of realistic measurement errors need to take into account the difference in spatial resolution between MODIS IST measurements and the model pixel scale. Measurement errors for MODIS IST at its raw resolution (i.e. 1.5 km) are expected to be ~1° -1.5°K (e.g. Hall et al., 2012). Hence the measurement errors at the model scale (25 km) are expected to be less than or equal to this value depending on the level of correlation of the measurement errors at the sub-pixel scale. In the case of perfectly uncorrelated sub-pixel measurement errors, the aggregated measurement would be expected to have a measurement error equal to the fine-scale value divided by the number of sub-grid MODIS pixels. Assuming uncorrelated sub-grid errors are likely overly optimistic, we postulated that the measurement error standard deviation of IST at the 25 km scale is 1K.

2.4.3 Implementation

The feasibility of the new DA system was evaluated via assimilation of IST as follows: A synthetically generated data stream was assimilated within an EnBS framework to assess the information content of the IST and explore whether it can overcome errors in forcing inputs. This was examined by comparing the open-loop and EnBS estimates of multiplicative states with the synthetic truth. Thereafter, the posterior meteorological forcings were fed into CROCUS to

estimate the surface mass fluxes. The performance of the EnBS algorithm was further evaluated through the comparison of the posterior estimates with the prior estimates and the true estimate for all surface mass fluxes. It is worth noting that in the OSSE in this study the ensemble size was set to 100 replicates which has been shown to be adequate in previous relevant studies (e.g. Margulis et al., 2002; Huang et al., 2008; Evensen 2009).

2.5 Results

2.5.1 Performance of the EnBS via Assimilation of IST

To provide an illustrative example of the methodology, Figure 2.3a-c shows the distribution of prior (open-loop) and posterior (obtained by assimilating IST) multiplicative state variables corresponding to the different forcings for a sample pixel (the red square in Figure 2.1) in the ablation zone (latitude 67ºN longitude 49.8ºW), which is the critical zone in terms of the GrIS surface mass loss. The prior distribution of multiplicative coefficients for each forcing variable is wide, representing the postulated uncertainty in the prior forcings. In contrast, Figure 2.3a shows that the histogram of the posterior estimates of γ_T is tightly distributed around the true estimate. A narrow distribution around the true estimate means that the DA system uses the information contained in the IST sequence and moves the ensemble members toward the true estimate while reducing the uncertainty of γ_T. The reduction in uncertainty is evident by comparing the base of the posterior histogram with that from the prior estimates. The positive update by the DA system can be explained based on the fact that IST and air temperature are coupled and each one affects

the other (Hall et al., 2008). Figure 2.3b illustrates that the median of the posterior estimate of γ_l agrees well with the corresponding synthetic truth. Incoming longwave radiation is correlated with the effective (near-surface) air temperature and as stated above, IST and surface air temperature are closely tied to each other. Prior to melt, solar radiation goes into heating the snow/ice surface and during the melt period, energy input drives sublimation or evaporation and melt (Box and Steffen 2001). Therefore, it can be stated that IST is positively correlated with the incoming shortwave radiation. The EnBS system takes advantage of this correlation and provides improved estimates of the multiplicative state related to shortwave radiation (Figure 2.3c).

Figure 2.3d presents the time series of the IST for the prior, posterior, synthetic true, and assimilated measurements during a portion of the assimilation window. For the purpose of illustration, IST data for 10 days during the dry period (January) and beginning of the melt period (April) were selected to show the ability of the algorithm to estimate the true IST (Figure 2.3d and Figure 2.3e). It is evident in Figure 2.3d-e that the EnBS captures the diurnal variability of IST and closely estimates the true IST both during the daytimes and nighttimes during the dry and melt periods. Moreover, Figure 2.3d shows that the EnBS successfully estimates the true IST even when the temporal resolution of the IST measurements significantly decreases. This is important since the IST record shows that there are fewer measurements available during the months of December and January (Hall et al., 2012) where in some years the available measurements during these two months drop to fewer than 10 measurements per month. Comparing Figure 2.3d with Figure 2.3e also shows that during the month of January when there

are fewer IST measurements the posterior estimates are in good agreement with the true IST, however, the uncertainty of the estimates is slightly larger. These results illustrate that information from IST measurements can be exploited to estimate the multiplicative states (i.e. γ_S, γ_l, and γ_T) and consequently the IST.

Results for the whole domain are presented in terms of relevant bulk metrics that capture the integrated impact of the forcings. Specifically, the pixel-wise cumulative incoming shortwave and incoming longwave radiation (in MJ/m^2/year) were used to represent the total energy input into the ice sheet and provide insight into the surface energy balance of the GrIS. For the air temperature, negative degree-day temperature (NDD) (i.e., cumulative mean daily air temperature for days in which the mean daily air temperature is below 0°C) and the positive degree-day temperature (PDD) (i.e., cumulative mean daily air temperature for days in which the mean daily air temperature is above 0°C) are two other metrics which are indicative of snow accumulation and melt periods, respectively. These bulk metrics were used to evaluate the performance of the DA algorithm over the entire ice sheet using RMSE and an improvement metric.

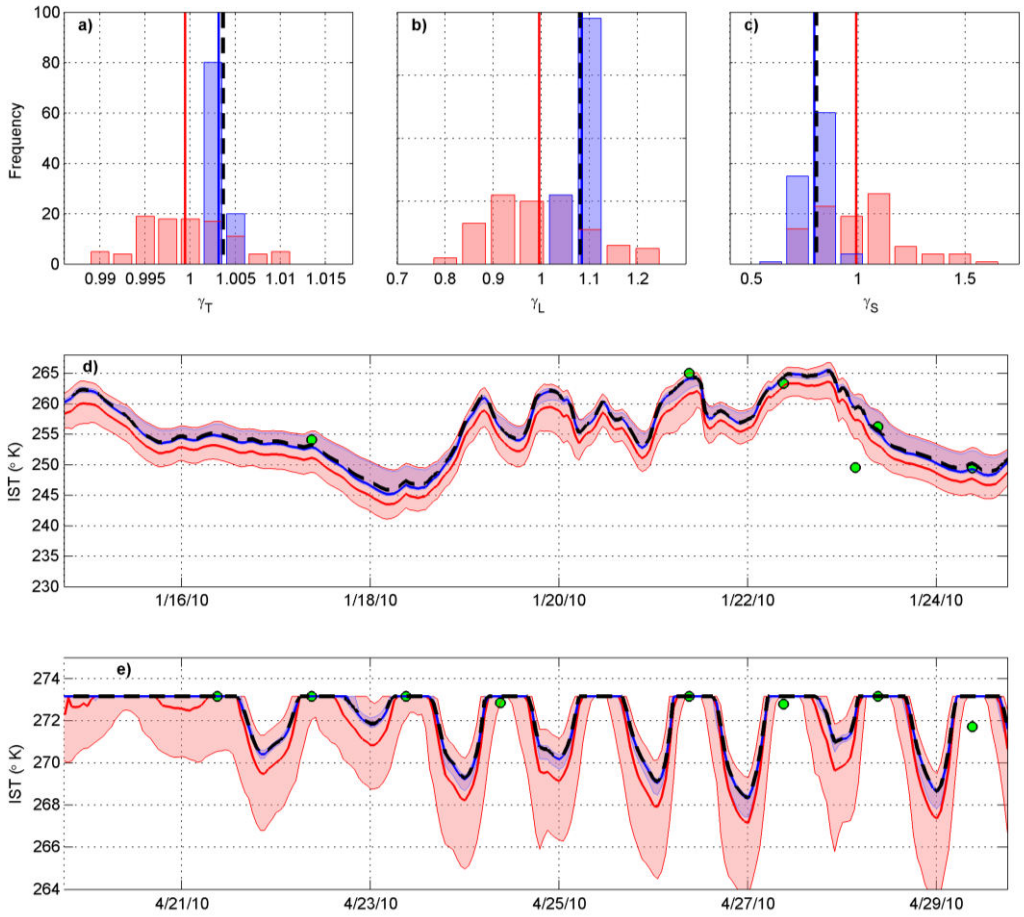

Figure 2.3 Ensemble histogram of the prior (red bars) and the posterior (after assimilation of IST) multiplicative states (blue bars) for (a) surface air temperature, (b) longwave radiation, (c) shortwave radiation for a sample pixel in the ablation zone. The prior (red line) and posterior (blue line) median values and truth (black line) are also shown for reference. The time series of: (d) the IST for the 10-day period during the dry season and (e) the IST for the 10-day period during the melt season. The red and blue shaded areas represent the prior and posterior uncertainty band (interquartile range) and the red, blue, and black lines represent the median of the prior, the median of the posterior and the truth, respectively. The green circles represent the synthetically generated (noisy) IST measurements that are assimilated to generate the posterior estimates.

The spatial mean bias and the spatial RMSE of the prior and posterior estimates of the integrated forcing variables over the GrIS were computed using the prior, posterior, and true cumulative longwave, shortwave, and air temperature (i.e., PDD and NDD). Table 2.2

summarizes the spatial mean bias and the spatial RMSE of the different forcing variables. As can be seen for the entire simulation period, the mean bias (RMSE) of cumulative shortwave, longwave, PDD, and NDD are, respectively, 84% (70%), 82% (85%), 94% (71%), and 65% (86%) less than the mean bias (RMSE) of the prior estimates.

Table 2.2 The spatial mean bias, the spatial RMSE, and improvement metric κ for the prior and posterior estimates of the forcing variables via assimilation of IST over the entire GrIS.

	R_s [MJ/m^2/yr]	R_l [MJ/m^2/yr]	PDD [ºC-day]	NDD [ºC-day]
Prior Bias	-82.0	-25.6	-16.7	-8.0
Posterior Bias	-12.8	+4.6	-1.0	-2.8
Prior RMSE	791.6	549.1	33.3	394.6
Posterior RMSE	241.3	97.9	9.7	55.4
κ	452.2	375.0	13.8	257.0

An alternative method to evaluate the DA system is to determine the contribution of RS data to the estimate explicitly. Following Durand et al. (2006) and Bateni et al. (2013) an improvement metric based on the prior and posterior error relative to the true was defined as follows:

$$\kappa_i = \left|\bar{Y}_i(-) - Y_i^{True}\right| - \left|\bar{Y}_i(+) - Y_i^{True}\right| \qquad (2.9)$$

where the $\bar{Y}_i(-)$ and $\bar{Y}_i(+)$ represent the cumulative ensemble median of the prior and posterior estimates of the forcing *i* respectively and Y_i^{True} is the cumulative synthetic true for the forcing *i*. The improvement metric κ_i can be used to interpret the contribution of the IST measurements to the posterior estimates of the forcing. This formulation suggests a value greater

than 0 when the posterior error is less than the prior error (i.e., measurement improves the posterior estimates), a value equal to 0 when the prior and posterior errors are equal, and a value less than 0 when the error in the posterior estimates is greater than that in the prior estimates (the measurement degrades the posterior estimates). Table 2.2 shows that IST measurements make a large contribution to correct the forcing variables. IST contributed an integrated sum of 452 (MJ/m^2/year), 375 (MJ/m^2/year), 14 (ºC-day), and 257 (ºC-day) to correct the shortwave, longwave, PPD, and NDD. The improvement metric of the PDD is much smaller than that of the NDD due the fact that there are many fewer days in which the mean daily near-surface air temperature is above the freezing point.

In order to further investigate the performance of the EnBS, the prior errors (i.e., prior - true) and the posterior errors (i.e., posterior - true) were computed for each forcing variable. Figure 2.4a-d shows the histograms of the prior and posterior errors for cumulative R_s , R_l , PDD, and NDD over the spatial domain. The EnBS reduces the uncertainty of the posterior estimates for all forcing variables and effectively removes any of the prior biases. Therefore, using the improved surface energy terms to force CROCUS improves vertically integrated melt energy and enhances the estimates of the states and fluxes over the vertical snow/ice column.

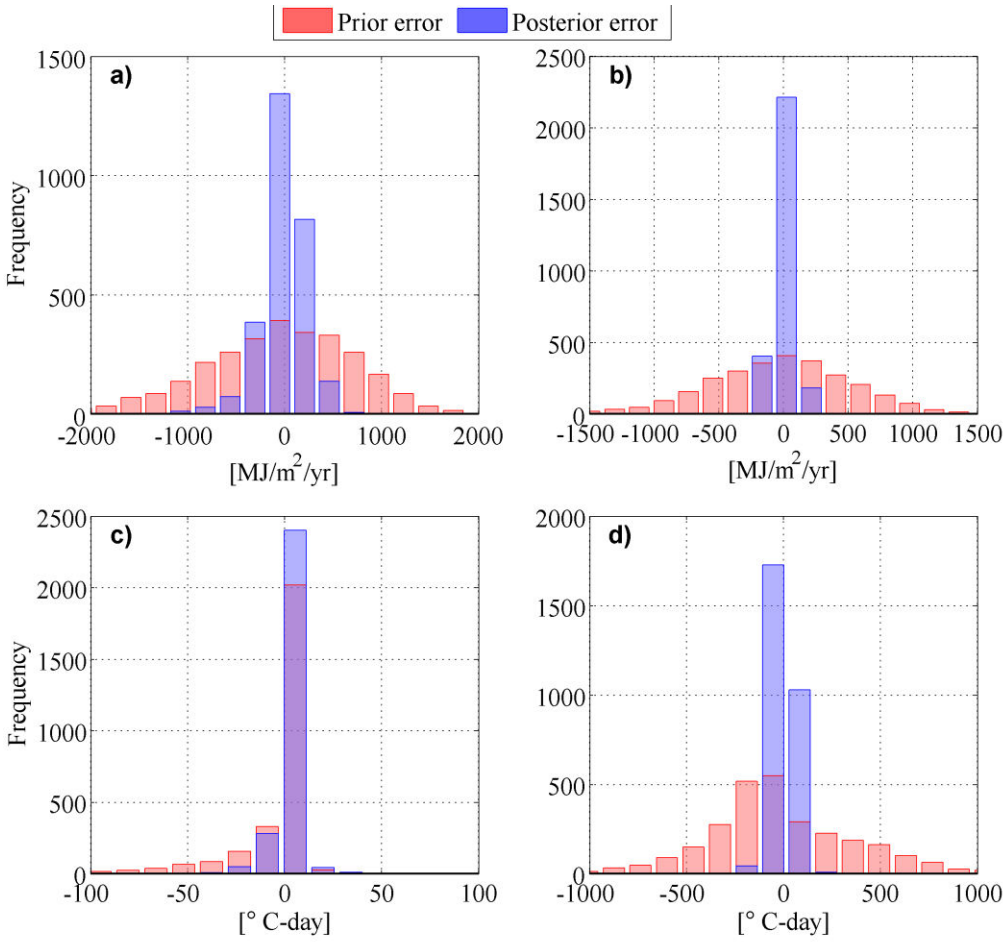

Figure 2.4 The histogram of the prior errors (red) and posterior (after assimilation of IST) errors (blue) for cumulative (a) shortwave radiation, (b) longwave radiation, (c) PDD, and (d) NDD over the full GrIS.

2.5.2 Updating the SML terms

While updating the forcing variables is the mechanism by which the EnBS transfers information from IST into the posterior estimates, the main objective of the DA framework in this study is to assess the feasibility of providing better estimates of the GrIS SML and related fluxes using the improved forcings. To generate a benchmark for our analysis, CROCUS was run in open-loop mode using the prior forcings (explained above). The SML terms obtained from the prior (open-loop) simulation constitute a basis for evaluation of the methodology implemented in

this study. Using the posterior forcing, CROCUS was executed for each grid cell to obtain posterior estimates of surface mass fluxes (i.e., runoff, sublimation /evaporation, and condensation) and consequently SML.

Runoff plays an important role in the GrIS net mass loss and is the main component of the GrIS SML. The GrIS meltwater runoff is heavily concentrated in the ablation zone along the ice sheet margin where the width of the ablation zone in the GrIS in some regions is very narrow and does not exceed tens of kilometres. The map of synthetic true runoff (Figure 2.5a) shows that the west and southwest margins experience the highest rates of runoff that exceeds 6 m water equivalent per year. It is worth remembering that the true runoff is an outlier in the context of ensemble modelling as explained previously. Figure 2.5b-c shows the runoff anomaly for the prior (i.e. prior-true) and the runoff anomaly for the posterior (i.e. posterior-true) respectively. The gray areas represent the percolation and dry snow zones, which do not generally contribute to surface runoff during the simulation period. It should be noted that in this area the snowmelt is not necessarily zero but refreezing can inhibit runoff. The prior anomaly map (Figure 2.5b) shows that the open-loop simulation consistently underestimates the true runoff across the domain with a strong negative anomaly in the southwest margin (more than 1600 mm water equivalent below the true). Comparing the GrIS margin pixels in the prior and posterior maps (Figure 2.5b-c) shows that the anomaly of the posterior estimates is significantly lower than that of the prior estimates. Reduced anomalies indicate that the EnBS successfully recovers the true estimates of the runoff in most pixels. However, the posterior results are not perfect and the

algorithm slightly underestimates and overestimates runoff in some pixels.

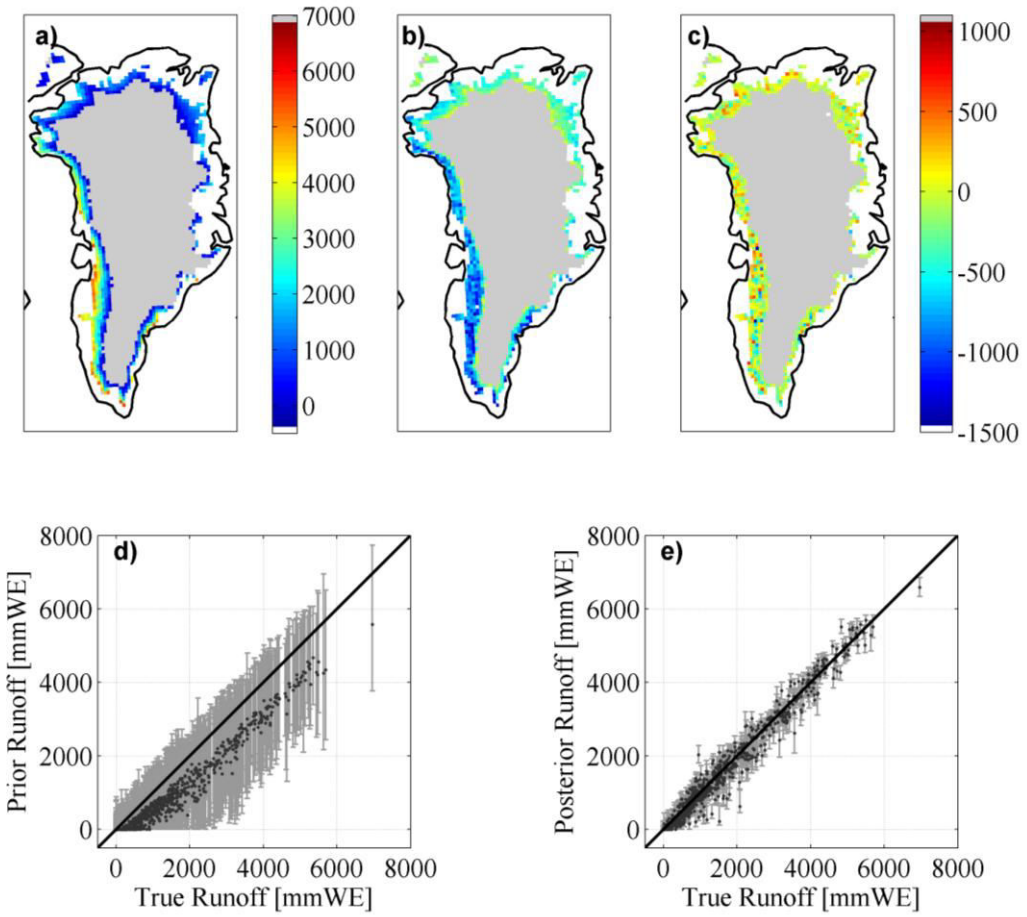

Figure 2.5 The (a) synthetic true runoff (mmWE/yr) for the year 2010, (b) runoff anomaly (mmWE/yr) for the prior (i.e., difference between the prior and true runoff), (c) runoff anomaly (mmWE/yr) for the posterior, (d) scatter plot of the prior runoff estimates, e) scatter plot of the posterior runoff estimates. Black dots are the ensemble median of the estimates and the error bars represent the corresponding ensemble interquartile range of the estimates.

Scatter plots of the runoff for the prior and posterior estimates versus the true estimates are illustrated in Figure 2.5d-e. Each data point in Figure 2.5d-e represents the ensemble median of the estimate (i.e., prior, posterior) versus the true estimate in a single pixel; and the error bar illustrates the corresponding ensemble interquartile range of the estimates in the same pixel. The

scatter plot of the prior runoff shows that almost all data points lie below the 1:1 line, indicating that the prior estimates were significantly biased (by construct in this OSSE). The posterior scatter plot (Figure 2.5e) displays that the data points are narrowly distributed around the 1:1 line and the error bars are much smaller than that in the prior estimates, implying that the proposed algorithm significantly removes the bias and decreases the uncertainty of the estimates.

Sublimation and evaporation play an important role in the GrIS surface mass loss. However, it should be noted that MAR and CROCUS estimate surface sublimation which is considerably smaller than drifting snow sublimation. Lenaerts et al. (2012) reported for the period 1960-2011 on average surface sublimation is responsible for 40% of total sublimation and drifting snow sublimation is responsible for another 60%. Here, the discussion focuses on sublimation rather than evaporation due to the fact that sublimation is one order of magnitude larger than evaporation. The map of synthetic true sublimation (Figure 2.6a) shows that the west and southwest of the GrIS in the ablation zone experience the largest sublimation rates. Box and Steffen (2001) explained that at the edge of the ice sheet, where slopes become steeper, the katabatic wind accelerates and tends to increase sublimation. Furthermore, the net radiation increases during the summertime, especially at lower latitudes, which in turn generates a vertical temperature gradient and increases the sublimation. Higher energy input also contributes to a positive albedo feedback (e.g. Tedesco et al. 2011) and further increases the sublimation rates. The prior anomaly map (Figure 2.6b) illustrates that the open-loop model underestimates the sublimation at the ice sheet margin and slightly overestimates it in the ice sheet interior. The

results demonstrate that posterior sublimation estimates from the assimilation of IST are much closer to the truth than are the prior estimates (Figure 2.6c). Comparing the scatter plots of the posterior versus the true estimates with that of the prior versus the true estimates, reveals that the methodology successfully overcomes the bias and significantly reduces the uncertainty of the sublimation estimates and increases the confidence of the results (see Figure 2.6d-e).

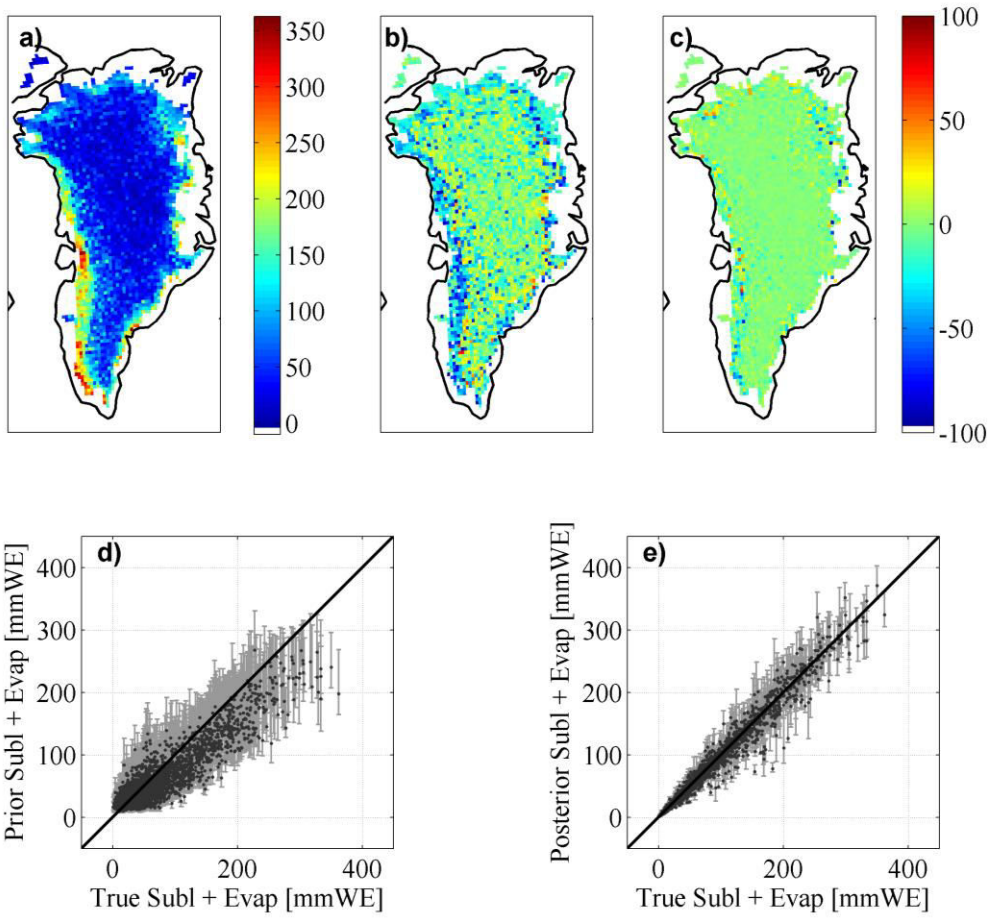

Figure 2.6 The same as Figure 2.5 but for sublimation and evaporation.

Surface solid condensation (deposition) also influences surface mass fluxes of the GrIS by adding mass to the ice sheet. Similar to sublimation, wind and the vertical specific humidity

gradient are two key factors that control the deposition. To be more precise, colder temperatures and lower winds enhance the deposition rates. In contrast with sublimation, deposition occurs at night and during winter, mainly due to radiative cooling (Box and Steffen 2001).

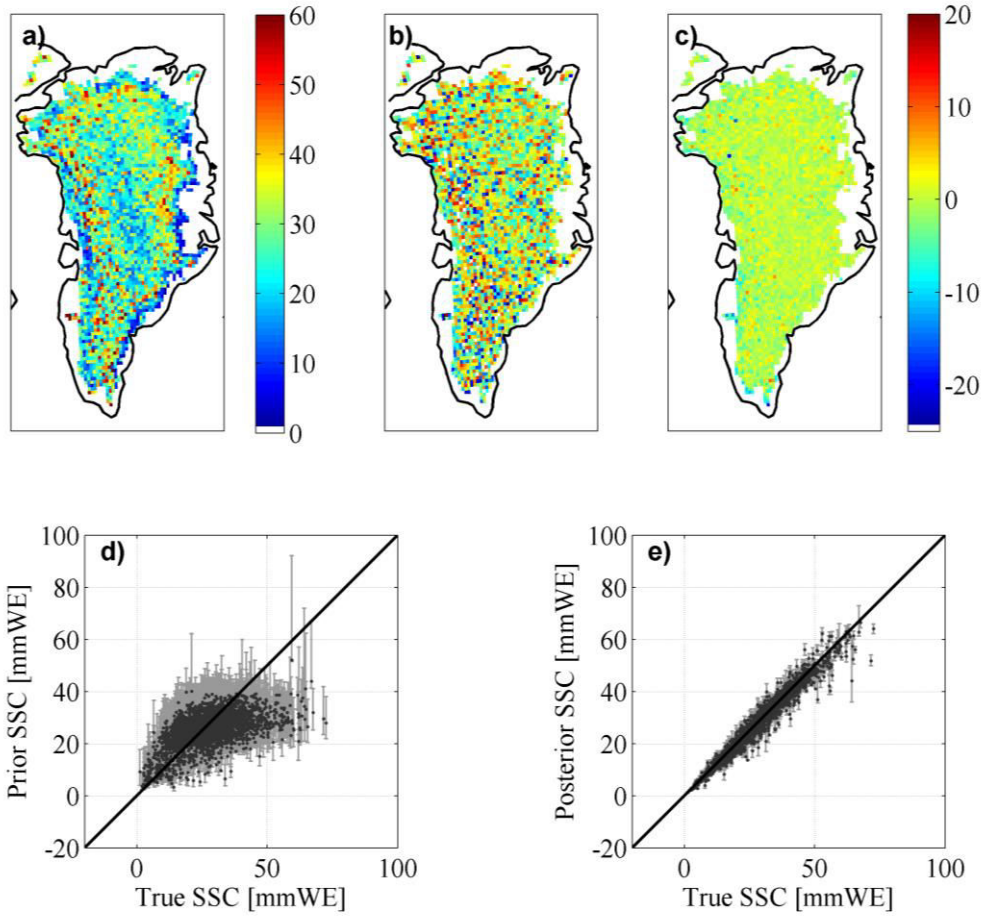

Figure 2.7 The same as Figure 2.5 but for surface solid condensation (SSC).

Figure 2.7a shows that the surface solid condensation (SSC) is greater in the ice sheet interior where winds are weak and there is sufficient moisture in the air column. The high elevation central regions, however, show less condensation due to distance from moisture sources. High speed winds in the ice sheet margins prevent condensation despite the availability

of moisture. Figure 2.7b shows that the prior estimates for SSC is not in good agreement with the truth and that the prior simulation both underestimates and overestimates surface solid condensation across the domain. A comparison between the prior and posterior anomaly maps (Figure 2.7b-c) suggests that the posterior estimates closely recover the true estimates. Figure 2.7e shows that the data points are clustered around the 1:1 line; indicating that the EnBS corrects the bias in the prior estimates (Figure 2.7d). In addition, posterior error bars are significantly smaller than that of the prior error bars, indicating that the EnBS effectively uses the information content of the IST measurements to eliminate the bias and reduce the uncertainties of the posterior estimates.

Herein, the SML is defined as the sum of the mass loss terms (i.e. runoff and sublimation/evaporation) and mass gain term (i.e. surface solid condensation) discussed above. Figure 2.8a shows that SML is greater in the west and southwest of the ice sheet where runoff is the dominant mass loss mechanism and is smaller in the ice sheet interior where mass loss mainly occurs through sublimation. Similar to runoff, the prior anomaly is largely concentrated in the ablation zone and since runoff is roughly two orders of magnitude larger than sublimation and condensation, the anomaly due to these two fluxes is almost undetectable in the anomaly map (see Figure 2.8b). Comparing the posterior anomaly map (Figure 2.8c) with that of the prior, clearly shows that the posterior SML is closely matched with the true estimates across the domain. Scatter plots (Figure 2.8d-e) also confirm that the EnBS effectively removes the bias and increases the confidence level of SML estimates.

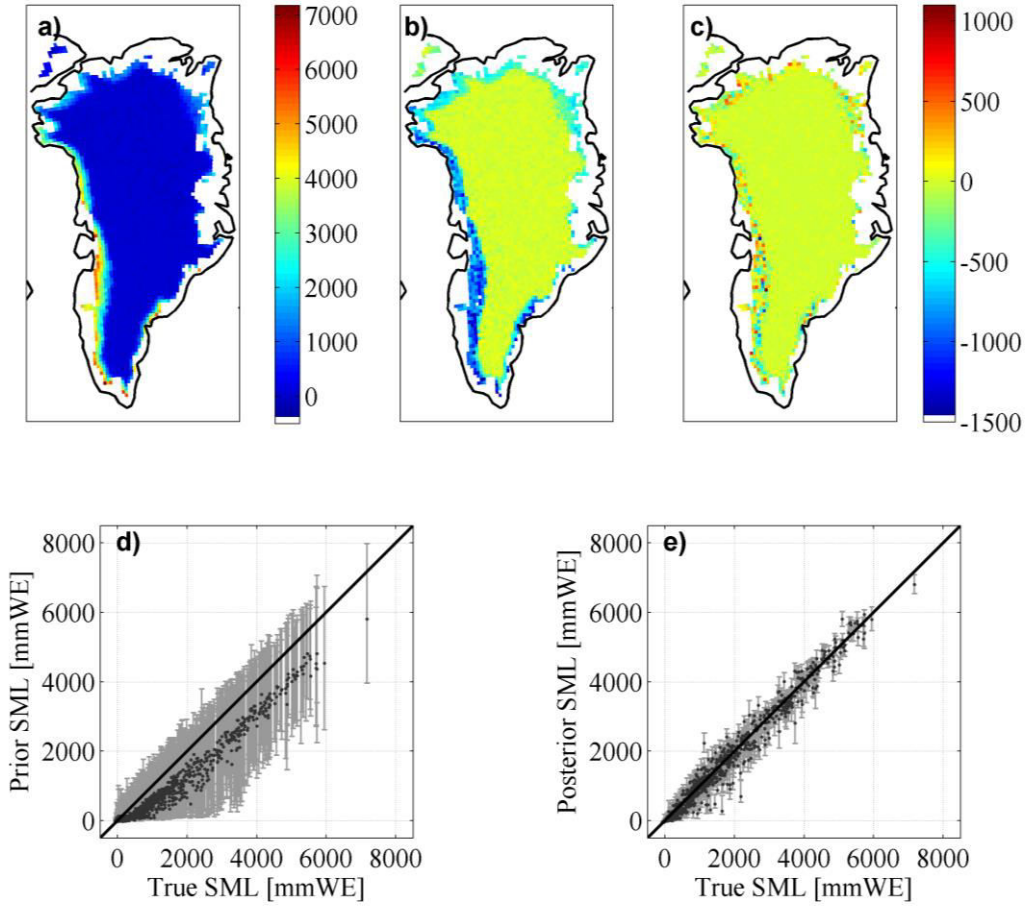

Figure 2.8 The same as Figure 2.5 but for the GrIS surface mass loss (SML).

To provide an integrated picture over the full domain, Figure 2.9a-d shows the time series of the cumulative runoff, sublimation, surface solid condensation, and SML over the GrIS respectively in 2010. As illustrated in Figure 2.9a, the true runoff starts in late April and increases rapidly during the melt season (to a cumulative value of 408 mm) until late August. The central tendency of the prior simulation (as indicated by the ensemble median) underestimates the runoff

by about 35% owing to errors in the forcing inputs. The posterior estimates show a cumulative runoff of 394 mm over the GrIS, which is in good agreement with the truth. Table 2.3 shows that the EnBS reduces the spatial mean bias (RMSE) of the prior estimates of runoff by 90% (61%) from -552 mm (646 mm) to -54 mm (250 mm). Note that runoff occurs in the ablation zone therefore the spatial mean bias and spatial RMSE for runoff were computed over the ablation zone. The spatial mean bias and spatial RMSE for sublimation, condensation, and SML were computed over the entire ice sheet. As evident in Figure 2.9b, sublimation accelerates during the summer season owing to increased energy input to the snow/ice surface. The true estimate suggests that in total net sublimation (i.e. sublimation and evaporation) accounts for about 66 mm (~15%) mass loss over the GrIS. The median of the prior simulation shows a total sublimation loss of ~56 mm which is 10 mm less than the truth. The EnBS significantly improves the results where the posterior median estimate shows a total sublimation of 65 mm. From Table 2.3 the spatial mean bias (RMSE) of the posterior estimate shows a 90% (64%) reduction relative to the prior. In general surface solid condensation accelerates during the winter and decelerates in the summer season (Figure 2.9c). The true simulation suggests a cumulative SCC of 27 mm, and the median of the prior and posterior estimates are 25 and 27 mm, respectively. The 76% reduction of the spatial RMSE of the posterior estimates and 80% reduction of the spatial mean bias (Table 2.3) also supports the accuracy of the posterior estimates. Finally, the true SML estimate is 450 mm, the prior and posterior median of SML are 295, 435 mm, respectively. Clearly the posterior SML estimate is in better agreement with the

truth. The IST measurements contribute an integrated sum of 140 mm to correct the posterior estimates of the GrIS SML and also reduce the spatial mean bias and the spatial RMSE of the estimates by 90% and 62% respectively (Table 2.3).

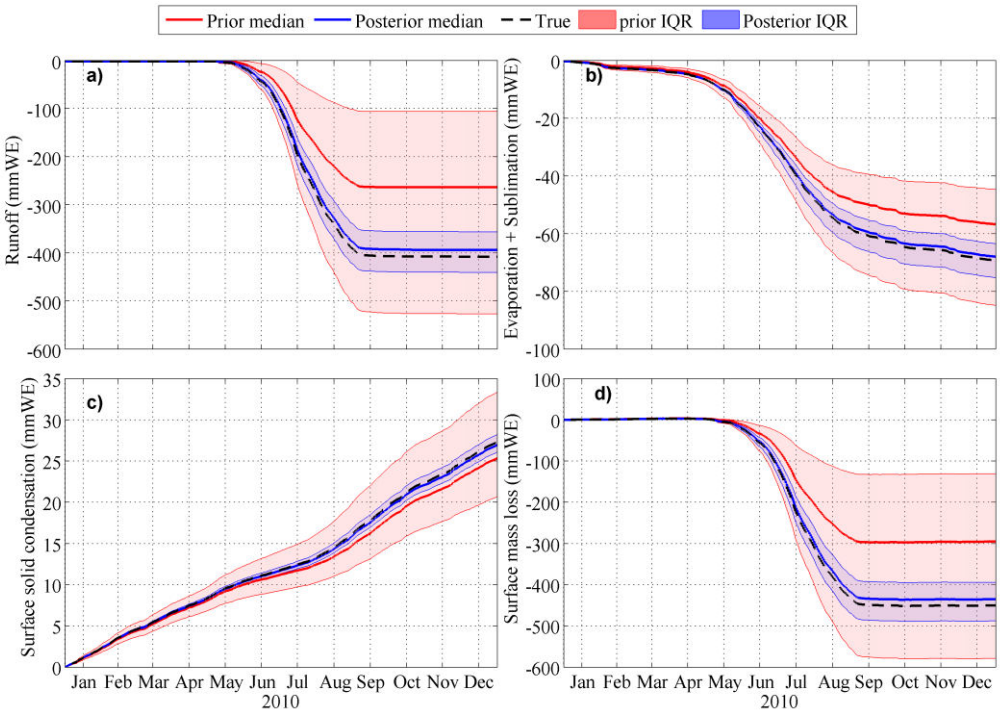

Figure 2.9 The time series of: (a) cumulative runoff, (b) cumulative sublimation and evaporation, (c) cumulative surface solid condensation, and (d) cumulative mass loss over the GrIS (in millimetres of water equivalent). The truth is the black dashed line, the prior ensemble median is the red line and the posterior ensemble median is the blue line. The red shaded area corresponds to the ensemble interquartile range (IQR) for the prior simulation and the blue shaded area corresponds to the ensemble IQR for the posterior estimates.

A probabilistic approach also provides information about the uncertainty of the estimates. Figure 2.9a-d show that the prior estimates of all surface mass fluxes have a large ensemble spread, reflecting the propagation of a priori forcing uncertainties to SML terms. During the update process the EnBS significantly reduces the uncertainties of the posterior estimates of

forcing variables and consequently the posterior estimates of the surface mass fluxes. Comparing the narrow blue shaded area with the wide red shaded area illustrates that the EnBS increases the confidence of the model predictions by decreasing the error and uncertainties of the posterior estimates relative to the prior estimates.

Table 2.3 The spatial mean bias and the spatial RMSE of runoff, sublimation/evaporation, surface solid condensation, and net mass loss estimates via assimilation of IST measurements. The spatial mean bias and the spatial RMSE for runoff were computed over the ablation zone and for the other surface mass fluxes were computed over the entire ice sheet.

	Runoff [mmWE]	Sublimation [mmWE]	SSC [mmWE]	Surface mass loss [mmWE]
Prior Bias	-551.6	-3.1	-0.5	-38.9
Posterior Bias	-54.0	-0.3	-0.1	-3.8
Prior RMSE	646.1	14.7	4.6	174.1
Posterior RMSE	249.8	5.3	1.1	66.9

2.5.3 Sensitivity to the synthetic truth values

As in any OSSE, the synthetic measurements are, by construct, a function of the chosen true and therefore the posterior results could be impacted by the particular selection of the true realization. To address this concern, and show the robustness of the proposed algorithm, the simulation was repeated for two different true values; one smaller than the baseline simulation and the other larger. In the first case the synthetic true runoff was set to 330 mm, which is the average of the runoff estimates from the open-loop simulation (i.e. ~260 mm) and the true runoff from the baseline simulation (i.e., ~400 mm). In the second case the true runoff was set to 470

mm, which is 70 mm larger than the baseline simulation. Table 2.4 shows the RMSE of the surface mass fluxes for all simulation cases. The posterior RMSE of each mass flux for all simulation cases are very similar even when the prior RMSE of the estimates are significantly different. For example, the prior RMSE of the runoff (SML) for the second simulation case (true runoff equal to 470 mm) is 2.5 (2.6) times larger than the prior RMSE of the first simulation case (true runoff equal to 330 mm), but the posterior RMSE differs by only 4% (10%). Therefore, it can be stated that the DA algorithm robustly retrieve the true estimates of the surface mass fluxes and the performance of the algorithm is relatively insensitive to the selected truth.

Table 2.4 The spatial RMSE of runoff, sublimation/evaporation, surface solid condensation, and net mass loss estimates via assimilation of IST measurements for three different true values.

True Runoff [mm]		Runoff [mm]	Sublimation [mm]	SSC [mm]	Surface mass loss [mm]
330	Prior	348.9	13.4	4.7	92.8
	Posterior	249.2	4.8	1.1	63.6
400 (baseline)	Prior	646.1	14.7	4.6	174.1
	Posterior	249.8	5.3	1.1	66.9
470	Prior	894.4	16.0	4.6	245.1
	Posterior	259.4	5.2	1.1	70.7

2.6 Discussion and conclusions

A new data assimilation methodology for improving estimates of the GrIS surface mass loss fluxes has been tested and presented using an observing system simulation experiment framework. The prior estimates were derived from an offline surface module (CROCUS) forced

by an ensemble of meteorological forcing fields that were based on a nominal regional climate model simulation (in this case MAR). A posterior estimate was generated by conditioning the forcings on the synthetically generated IST measurements using an ensemble batch smoother (EnBS) approach. Specifically, it was shown that using the EnBS with IST measurements was able to improve nominal estimates derived from MAR that result from erroneous forcing fields that drive surface mass and energy balance processes. The results illustrated that IST measurements have potential information on shortwave, longwave, and surface air temperature that allows for correction of errors in these terms. However, due to the lack of meaningful correlation between precipitation and IST measurements, the precipitation flux was not updated in this context (i.e. the prior and posterior precipitation is the same). Hence the assimilation of IST is primarily beneficial for estimating the surface mass loss terms and not the accumulation term. However, it should be noted that, using MAR-CROCUS to generate the synthetic truth might lead to optimistic results since the truth is taken from the same model. Mitigation of this was attempted by using an outlier for the truth. An expensive alternative, but worth pursuing in future work, would be to use other RCM models to generate the synthetic truth. That said, it can be argued that using another model such as RACMO2 (Ettema et al., 2009) to generate the true realization will not significantly affect the results because the synthetic truth from RACMO2 is likely to fall within the ensemble spread of MAR-CROCUS trajectory. The main reasons for that are (1) the SMB fluxes from MAR and RACMO2 are highly correlated (Fettweis et al., 2013), (2) the trends of SMB fluxes from two models are very similar Vernon et al., (2013). Furthermore,

sensitivity analysis shows that the proposed algorithm is able to retrieve the synthetic truth for the extreme cases where the real true stats fall beyond the chosen values.

The new methodology has several advantages over the traditional state-space data assimilation approaches. First, in this new application the multiplicative perturbation variables are considered as states to be updated. Reduction of the size of the state vector and consequently computational costs is the direct outcome of this approach. Second, mass loss terms cannot directly be sensed by the means of satellite sensors; using this methodology, the mass loss fluxes were estimated indirectly by reducing the error in forcing variables. Finally, the modularity of the proposed methodology would allow for incorporation of any regional climate model and additional remotely-sensed observations in future applications. All of these advantages should make such data assimilation approaches an attractive and complementary approach to better resolve and diagnose the ice sheet surface mass fluxes. The improved mass loss estimates could also be used as input to net mass balance estimates and ultimately a sea level rise projection when applied to real data over the remote sensing record.

As a final note, it should be emphasized that the application presented in this study does not attempt to optimize or include uncertainty in any model parameters. Rather, the focus is on the uncertainty of time-varying model forcing inputs, which is expected to be the primary source of uncertainty in estimates of surface melt. We acknowledge that the model parameters are treated as certain and therefore, any uncertainty/error in model parameters (e.g., water holding capacity that impacts the transformation of meltwater into runoff) would increase the expected error in

posterior SML in an application with real data. A more general case where estimation of parameters is included in the data assimilation framework could be the basis of future work.

The next logical step is to apply the methodology with real IST measurements to further validate the robustness of the proposed approach. This future work will include the use of the MODIS IST product for estimating GrIS SML. The data assimilation framework is general and could also include the potential application of assimilation of passive microwave, albedo, and even Gravity Recovery and Climate Experiment (GRACE) data to further constrain GrIS SMB estimates.

3 Characterization of the Greenland Ice Sheet Surface Mass Balance Via Assimilation of Ice Surface Temperature into the CROCUS Snow Ice Model

3.1 Introduction and Background

Climate change due to human activities is one of the greatest challenges of recent decades as it directly impacts the polar ice sheets and eventually sea level rise. As reported by Jansen et al. (2007), Arctic regions are currently facing increasingly warmer climate (warmer than at any time in the last 125000 years), which has raised concern about the possibility of significant polar ice melt. Major changes in the Greenland ice sheet (GrIS) as a part of the polar regions have already been studied and reported over the last decade including 1) significant thinning of the marginal ice (Krabill et al., 2004; Pritchard et al., 2009; Straneo et al., 2013; Khan et al., 2014), 2) glaciers acceleration and increase in ice discharge from many of Greenland outlet glaciers (Rignot 2010; Wouters et al., 2013; Enderlin et al., 2014); 3) significant surface melt (Tedecso et al., 2013; Fettweis et al., 2013; Nghiem et al., 2012; Hall et al., 2013; Vernon et al., 2013); and a thickening of the ice sheet in the Greenland interior (Thomas et al., 2006).

The GrIS is losing mass through ice discharge from outlet glaciers and surface processes (e.g. meltwater runoff, sublimation, and evaporation). Enderlin et al., (2014) shows that contribution of ice discharge to the total GrIS mass loss has been reduced from 58% during 2000-2005 to 36% during 2005-2009 and 32% between 2009 and 2012.

Despite the importance of mass loss through surface processes, fundamental questions remain unanswered including: How much does GrIS lose mass through the surface process? What is the temporal variability of the surface fluxes and how they change over the course of the year? What is the spatial variability of surface mass fluxes and how do the different regions of the GrIS respond to changes in atmospheric forcing? What are corresponding uncertainties of the GrIS surface mass fluxes? Lack of measurements in combination with insufficient parameterization of the GrIS surface processes are the primary reasons for large uncertainty in surface mass loss estimates (e.g., Smith et al., 2015; Alexander et al., 2014).

Limited and sparse in situ measurements such as the Greenland climate network (GC-Net: Steffen and Box, 2001), K-transect measurements (van de Wal et al., 2012), and data from ice core projects have been used to verify and validate models, remotely sensed data/products, and retrieval algorithms (e.g. Fettweis et al., 2005; Burgess et al., 2010). However, it is obvious that spatially continuous estimates of fluxes cannot be obtained by applying interpolation techniques to these sparse data sets. Taking into account the shortcoming of in situ measurements, surface remote sensing suggests a further possibility to study SMB.

Surface remote sensing (RS) data contain indirect and implicit information about GrIS surface processes with relatively high spatial and temporal resolutions. These data have been mostly used to estimate the melt extent and melt duration over the GrIS (e.g. Abdalati and Steffen, 1995; Tedesco et al., 2013; Hall et al., 2013). Theoretically, satellite-based visible and near infrared (Vis/NIR) data contain information on surface temperature, the solar energy

absorbed by the snowpack, and snow phase (wet/dry) but this information has not been fully exploited due to indirect and implicit links between these data/products and the SMB terms.

Given the limitations of the above mentioned observation-based methods, spatially and temporally continuous estimates of surface mass loss fluxes generally require physically based numerical modeling. These tools offer a significant advantage as they can provide spatially and temporally distributed estimates; however, error and uncertainty in the forcings and initial conditions directly propagate into the estimate of mass loss fluxes. While there is significant ongoing research focusing on these methods individually, there are some efforts (e.g. Larour et al. 2014; Navari et al., 2015) to take advantages of both models and remotely sensed measurements through the merging of these two data streams to construct reanalysis estimates of surface mass loss fluxes. In this approach, measurement can optimally merge with a model using data assimilation techniques, which have been proven to be a more robust alternative to deterministic modeling approach (e.g., Girotto et al., 2014).

The complexities of the ice sheet surface dynamics and nonlinearities of underlying surface mass loss mechanisms have introduced considerable uncertainties into the surface mass fluxes from different methodologies. Our previous work (Navari et al., 2015) has shown that a data assimilation methodology can overcome uncertainties associated with surface mass fluxes from a regional climate model via assimilation of ice surface temperature (IST). This work is a continuation of the previous study on which the feasibility of the methodology was examined using an observing system simulation experiment (OSSE). Here, satellite-derived IST is used to

condition a priori snow/ice model estimates to generate reanalysis estimates of the GrIS surface mass fluxes and associated spatiotemporal variability. We are trying to answer: How much does the GrIS lose mass through the surface process? How are these results comparable with open-loop simulation? What is the temporal and spatial variability of the surface fluxes? In Section 3.2 we briefly introduce models and the methodology used in this study. Section 3.3 describes the study areas and data sets. In Section 3.4 the experimental design is described and assimilation results are presented in Section 3.5. Assessment and verification of the results are presented in Section 3.6 and conclusions and future work are discussed in Section 3.7.

3.2 Method, and models

3.2.1 Regional climate model

In the data assimilation framework in this study the regional climate model Modèle Atmosphérique Régional (MAR; Gallée and Schayes (1994) and Gallée and Duynkerke (1997)) was used to generate hourly near-surface meteorological outputs (i.e., temperature, pressure, wind speed and direction, longwave and shortwave radiation, precipitation, pressure, humidity, etc.) for the years 2009 and 2010 at a horizontal spatial resolution of 25 km to force an offline snow/ice model (i.e. forward model). MAR has been recently selected as the official SMB model for the ICE2SEA European project aiming at quantifying the potential contribution of the ice sheets to sea level rise. We emphasize that MAR is fully coupled with the snow physical model CROCUS (Brun et al., 1992) described below. The reader is referred to Lefebre et al. (2003, 2005) and Fettweis et al. (2005) for detailed information on the MAR setup used here.

3.2.2 Surface mass/energy balance and snow physical model

The forward model used in this study is the surface mass/energy balance snow physical model CROCUS (Brun et al. 1989, 1992). CROCUS is a one dimensional, multi-layered energy balance model consisting of a thermodynamic module, a water balance module taking into account the refreezing of meltwater, a turbulence module, a snow metamorphism module, a snow/ice discretization module and an integrated surface albedo module. CROCUS was run in ensemble mode using an ensemble of meteorological forcing data including precipitation, shortwave, longwave, air temperature, wind speed, relative humidity, and cloudiness to generate an ensemble of prior estimates of the surface states and fluxes. The implementation of CROCUS in the data assimilation framework is explained in Navari et al. (2015).

3.2.3 Model adaptation

3.2.3.1 Boundary condition

The CROCUS snow/ice model was originally developed for operational avalanche forecasting. Therefore, the model has been modified for SMB ice sheet applications. Following Fettweis (2006), the bottom boundary condition was modified for simulating the top ~10 m of the ice sheets. This method consists of the following rules. First, if during the model integration the sum of the snow and ice layer thicknesses becomes less than 8 m, the modeled bottom layer is extended by two meters. Second, in the case that the sum of the snow and ice layer thicknesses becomes larger than 15 m, the bottom layer is divided by two. This is consistent with the methodology used in nominal MAR simulations.

3.2.3.2 Albedo parameterization

The CROCUS albedo parameterization has been described in Brun et al (1992). The CROCUS snow albedo depends on snow density and optical grain diameter; though density does not directly affect the albedo but has a direct impact on grain size. More importantly, CROCUS uses density to differentiate between snow and ice layers. The optical grain diameter is a function of sphericity, dendricity, and grain size (Brun et al 1992). CROCUS computes snow albedo for three spectral ranges including the visible range (0.3-0.8μm), and two near infrared ranges (i.e. 0.8-1.5μm and 1.5-2.8 μm) as follows:

$$\alpha_1 = \min\left[0.94, 0.96 - 1.58\sqrt{d}\right] - 0.2\frac{age}{60} \quad (0.3-0.8\mu\text{m}) \qquad (3.1)$$

$$\alpha_2 = 0.95 - 15.4 * \sqrt{d} \quad (0.8-1.5\mu\text{m}) \qquad (3.2)$$

$$\alpha_3 = 346.3\,d' - 32.31\sqrt{d'} + 0.88 \quad (1.5-2.8\mu\text{m})$$
$$d' = \min\left(d, 0.0023\right) \qquad (3.3)$$

where *age* is the snow age in days, and *d* is the optical grain diameter in m. MAR uses a modified and upgraded version of the CROCUS snow and ice albedo as described in Lefebre et al. (2003). Here the CROCUS albedo parameterization was updated using MAR albedo parameterization. CROCUS takes into account the snow impurities by correcting the visible band snow albedo via adding an aging factor (i.e. visible albedo decreases as the snow surface ages). Although, the GrIS snow/ice impurity is an open area of research, the impurity term in CROCUS was calibrated to take into account the dry deposition (vegetation dust) from the forest close to the CROCUS test site in Col de Porte, France, which is not relevant to our application over the GrIS. Following

Dumont et al., (2014), the impurity term (i.e., the term $0.2\frac{age}{60}$) was removed from the visible band albedo. Removing the effect of impurities makes the CROCUS albedo more consistent with the MAR albedo scheme, and the visible band snow albedo becomes solely a function of the optical grain diameter (d). However, the visible band snow albedo is still slightly different from the MAR equation. MAR uses the maximum function instead of the minimum function in Eq. (3.1) which mean the visible snow albedo is always larger than 0.94. This is more likely a bug in the equation which needs to be fixed. Here, the CROCUS equation was preferred to the MAR equation since it better represents the visible snow albedo. For the first near infrared range, no modification was applied since the both MAR and CROCUS have an identical equation (i.e. Eq. (3.2)). For the second near infrared range MAR and CROCUS use slightly different equations; here the CROCUS equation was preferred to the MAR equation since the MAR equation results in unrealistic albedo for the optical grain diameter (d) greater than 0.0028 m which can frequently be seen in the MAR output during the melt period (especially in the ablation zone). In addition, similar to the MAR albedo scheme, the lower limit of the snow albedo was set to 0.65 for all spectral ranges.

Over the bare ice, CROCUS uses constant values of 0.45, 0.3, and 0.1 for the above-mentioned three spectral ranges, respectively. The spectral albedo for the bare ice surface is replaced with that from MAR. MAR uses a fixed value of 0.45 for bare ice albedo in all spectral ranges. In CROCUS a layer is considered as a snow layer if the layer density is less than 850 kg/m^3; following MAR the ice threshold was reduced from 850 kg/m^3 to 800 kg/m^3. Using

the snow/ice threshold causes a discontinuity in the time series of albedo. To ensure a smooth transition around the threshold value, the MAR transition equation was used as follows:

$$\alpha_{ice} = \alpha_{bare\,ice} + (0.65 - \alpha_{bare\,ice})\left(\frac{\rho_{snow} - 917 kgm^{-3}}{800 - 917 kgm^{-3}}\right) \quad (3.4)$$

where α_{ice} is the ice albedo for the cases where the density of layer is between 800-917 kg/m^3, $\alpha_{bare\,ice}$ is the bare ice albedo, and ρ_{snow} is the layer density.

MAR also uses a transition albedo if the thickness of the snow layers above the ice or compact snow (layer with a density larger than the snow threshold of 800 kg/m^3) becomes less than 10 cm. This transition is simply an interpolation between the snow albedo and ice albedo (Eq. (3.4)) which is applied to all spectral albedo terms as follows:

$$\begin{cases} \alpha_i = \alpha_{ice} + (\alpha_i - \alpha_{ice})\left(\frac{H_{snow}}{0.1}\right) & for\ H_{snow} < 0.1m \\ \alpha_i = \alpha_i & for\ H_{snow} \geq 0.1m \end{cases} \quad (3.5)$$

where α_i is the spectral snow albedo, H_{snow} is the snowpack thickness above the ice layer. It should be noted that MAR v2.0 has been used in this study and the albedo parameterization has been slightly modified in MAR v3.2. In MAR v3.2, the bare ice albedo is a function of meltwater production and ranges between 0.45 to 0.55. The snow and ice threshold has also been increased from 800 kg/m^3 to 830 kg/m^3. A complete description of MAR v3.2 albedo scheme can be found in Alexander et al., (2014). It also should be highlighted that both the MAR and CROCUS albedo modules have been designed to simulate pure snow and ice albedo while studies over the GrIS show that impurities play an important role in surface melt through the albedo feedback. This can be an important source of error in SMB estimates using MAR and CROCUS.

3.2.4 Melt extent and melt duration from passive microwave

In this study, melt extent and melt duration diagnosed from passive microwave measurements have been used to attempt to verify the assimilation results. Hence, this section briefly summarizes the method has been implemented to retrieve melt extent and melt duration from passive microwave brightness temperature. Melt extent and melt duration have been extensively investigated using remote sensing data from different satellite imagery such as passive microwave data (e.g. Abdalati and Steffen 1995, 1997; Fettweis et al 2006, 2011; Tedesco 2007) and ice surface temperature data (e.g. Hall et al., 2013). The Cross Polarization Gradient Ratio (XPGR) and the Diurnal Amplitude Variation (DAV) are the two well-known algorithms which can be used to estimate the melt extent and melt duration. The XPGR uses the normalized difference between the 19 GHz H-pol and the 37 GHz V-pol (Abdalati and Steffen 1995), and the DAV (Ramage and Isacks, 2002) uses the difference between brightness temperature at ascending and descending passes of the 19 GHz H-pol or the 37 GHz V-pol.

The DAV algorithm was preferred to the XPGR because finding the melt thresholds for passive microwave from the Advanced Microwave Scanning Radiometer - Earth Observing System AMSR-E does not require field experiments. In addition, the DAV is very sensitive to the daily melt cycle (Tedesco, 2007) and it can also detect the liquid water under the frozen surface layer during the nighttime. Following Tedesco (2007) two criteria were used to detect the melt onset and wet snow including a) brightness temperature at 37GHz V-pol becomes larger than a fixed threshold (A), and b) the difference between the ascending and descending passes at 37

GHz V-pol becomes larger than another fixed threshold B (i.e. $DAV = abs(T_b^{ascending} - T_b^{descending}) > B$). During the melt season melt might persist during the night (sustained melt), which means the DVA will be very small; to account for this condition it was assumed that snow is melting when both the ascending and descending values are larger than the threshold A.

Apgar et al., (2007) reported a brightness temperature threshold (A) of 252 K and a DAV threshold (B) of ±18 K to detect the presence of wet snow in the sub-arctic region using AMSR-E data. Tedesco (2007) applied a brightness temperature threshold of 258 and a DAV threshold of ±18 K to the 37 GHz V-pol Special Sensor Microwave Imager (SSM/I) data to study the melt over the GrIS. Monahan et al., (2010) used AMSR-E data with a brightness temperature threshold of 252 K and a DAV threshold of ±18 K to study melt pattern of the southern Patagonia ice field.

Ramage and Isacks, (2003) suggested a method to compute the brightness temperature threshold (A) using the histogram of the measured brightness temperature. The histogram of brightness temperature shows a bimodal distribution if the snow melts during the melt season. The population in the left side of the histogram represents the frozen snow and the population in the right side represents the melting snow. They suggested the lowest population between the two peaks to be considered as a threshold between the dry and wet snow.

3.2.5 Reanalysis Method (Ensemble Batch Smoother algorithm)

Data assimilation is a general term for an algorithm that systematically merges the

measurements and models assuming both contain useful information about the states of the system while both models and measurements contain errors. Data assimilation techniques have a well-established history in hydrology (e.g. Reichle et al., 2002; De Lannoy et al., 2012; Girotto et al., 2014a; Bateni et al., 2013, 2015; Margulis et al., 2015). For comprehensive details, the reader is referred to these references.

In this work, an EnBS framework is implemented to merge satellite-derived IST with prior states (i.e. prior multiplicative states) to generate posterior states. The key aspects of the method are described below. Unlike commonly used filtering method in which states are sequentially updated when a measurement becomes available, EnBS updates the states in a single step using all measurements in the assimilation window (i.e. one year). In this way, the EnBS removes the overall bias and better fit the true states while there still might be some degree of disagreement between the true states and the EnBS results.

Many studies (e.g. Rignot et al., 2011; Vernon et al., 2013; Smith et al., 2015) have shown that error and uncertainty in model input variables are an important source of uncertainty in surface mass fluxes from different deterministic approaches. The data assimilation techniques can overcome uncertainty in forcing variables and consequently provide better estimates of states and fluxes (e.g. Durand et al. 2008; Girotto et al., 2014a,b; and Navari et al., 2015).

In this study, a multiplicative lognormal perturbation model (e.g., Forman and Margulis 2010) was used to incorporate expected uncertainty to the key forcing variables (i.e., precipitation (P), longwave (R_l), shortwave (R_s), and air temperature (T_a) [K]) using the mean

and coefficient of variation. The prior uncertainty in forcing variables can be modeled via:

$$F_j(x,t) = \gamma_{F,j}(x).F_{MAR}(x,t) \quad (3.6)$$

where $F_j(x,t)$ is perturbed forcing variable (i.e. $P_j(x,t)$, $R^{\downarrow}_{s,j}(x,t)$, $R^{\downarrow}_{l,j}(x,t)$, and $T_{a,j}(x,t)$) with postulated uncertainty, and $F_{MAR}(x,t)$ is the nominal near-surface meteorological output from regional climate model (i.e. $P_{MAR}(x,t)$, $R^{\downarrow}_{s,MAR}(x,t)$, $R^{\downarrow}_{l,MAR}(x,t)$, and $T_{a,MAR}(x,t)$), $\gamma_{F,j}(x)$ is lognormally-distributed multiplicative coefficients designed to capture uncertainty in the forcing inputs. The subscript *F* represents different forcing (i.e., *P*, R_l, R_s, and T_a), and *j* represents an individual ensemble member sampled from the postulated uncertainty distribution ($j = 1,\ldots, N_e$, where N_e represents the ensemble size) and *x* shows the spatial index (i.e., implicitly represents an individual computational pixel in the domain).

Finding the uncertainty structure of near-surface meteorological data over the GrIS is very difficult since there are very limited measurements. Here, for simplicity, we chose to use literature reported coefficient of variation (CV) and cross correlations between the variables to perturb the meteorological forcings. Following De Lannoy et al., (2010, 2012) precipitation was perturbed using multiplicative coefficients with mean=1 and CV=0.5, downward shortwave was perturbed using multiplicative coefficients with mean=1 and CV=0.2, downward longwave and surface air temperature were subject to multiplicative perturbation with mean=1 and CV=0.1 (R_l) and CV=0.005 (T_a) respectively. To impose the cross correlation between the forcing variables following values were used (LW–SW:-0.3, SW–P:-0.1, SW–Ta: 0.3, LW–P: 0.5, LW–Ta: 0.6,

P–Ta: -0.1). Note that the key point is to achieve a reasonable level of uncertainty that represent the realistic uncertainty of the forcing variables.

Updating the state variables does not provide quantitative information about surface mass fluxes. Hence, the forcing variables were treated as states to be updated. This means that the prior pdf of forcing variables was conditioned on the measurements to obtain the posterior pdf of the forcing variables. This strategy, was also reported specifically for precipitation in Durand et al. (2008); Girotto et al. (2014a,b); and for longwave, shortwave, and air temperature in Navari et al., (2015). The updated forcing variables (via the updated $\gamma_{i,j}$), can then be used to obtain an improved posterior estimate of the surface mass fluxes. It has been shown in Navari et al., (2015) that precipitation, the main component of SMB, can't be robustly updated using IST due to the fact that there is no meaningful correlation between IST and precipitation. Consequently, the study was adopted to estimate the GrIS surface mass loss (SML), which to a large degree is independent of precipitation. In order to take into account the indirect effects of precipitation on SML through the albedo and precipitation energy flux, we chose to perturb the precipitation instead of using the nominal precipitation from MAR. However, we emphasize that only the GrIS SML components (i.e., sublimation/evaporation, condensation, and runoff) were constrained while still including the expected uncertainty in the accumulation term (precipitation). While the data assimilation framework updates the SML components, precipitation kept unchanged.

In the update step, the EnBS provides estimates of uncertain $\gamma_{i,j}$ parameters as a means for

improving prior estimates of surface mass fluxes through conditioning on IST measurements. The open-loop (prior) estimate of the variables of interest (i.e., γ_S, γ_l, and γ_T) were collected into the state matrix Γ^-. Similarly, the vector of satellite-derived ice surface temperature (IST) measurements was assembled into a vector:

$$T_{measurement} = f(T_{IST}) \tag{3.7}$$

where T_{IST} is the IST measurement, and f is an aggregation operator which transfers the IST data into the model space. The EnBS individually updates each ensemble member via a Kalman-type update equation (e.g., Durand and Margulis, 2008; Navari et al., 2015),

$$\Gamma_j^+ = \Gamma_j^- + K[T_{measurement} + V_j - T_{predicted,j}] \tag{3.8}$$

where Γ_j^- and Γ_j^+ represent the *j*th ensemble member before and after the update, respectively, $T_{measurement}$ is satellite-derived IST, $T_{predicted}$ is the matrix of predicted measurements consisting of the predicted GrIS surface temperature generated by the integration of forward model using the prior forcing variables. V is the additive Gaussian measurement error that was synthetically produced and added to the measurements in order to avoid correlation among the replicates (Burgers et al. 1998), and K is the Kalman gain matrix, which is computed from the sample covariances. In this framework, the state variables relate to the measurements in the batch through the covariance matrices that are obtained from the ensemble. A posterior simulation was performed using the posterior estimates of $\gamma_{i,j}$ in the forward model to generate reanalysis time series of the surface mass fluxes.

3.3 Study Site and Data

3.3.1 Study site

In this study, the focus is on fully covered snow/ice pixels of the GrIS. Based on MAR mask the study domain consists of 2817 pixels of 25 km by 25 km with an area of $1.76 \times 10^6\ km^2$. Figure 3.1 shows the different GrIS mass balance zones based on a forward simulation for the year 2010 and topographic contour lines. Three distinct mass balance zones over the GrIS includes: 1) The ablation zone: the region of the GrIS where the annual surface mass balance is negative. 2) The dry snow zone: the region where the mean annual temperature is less than -25ºC (Cuffey and Paterson 2010) and melt generally does not occur. 3) The percolation zone: the area between the ablation zone and the dry snow zone where surface meltwater percolates downward into the snow layers and is separated from the ablation zone by the equilibrium line.

3.3.2 Data

3.3.2.1 Ice surface temperature data

The EnBS framework conditions the prior meteorological forcing on satellite-derived IST measurements. The satellite-derived data used in reanalysis estimate proposed in this work is a mixed data set which was generated by combing the two IST products.

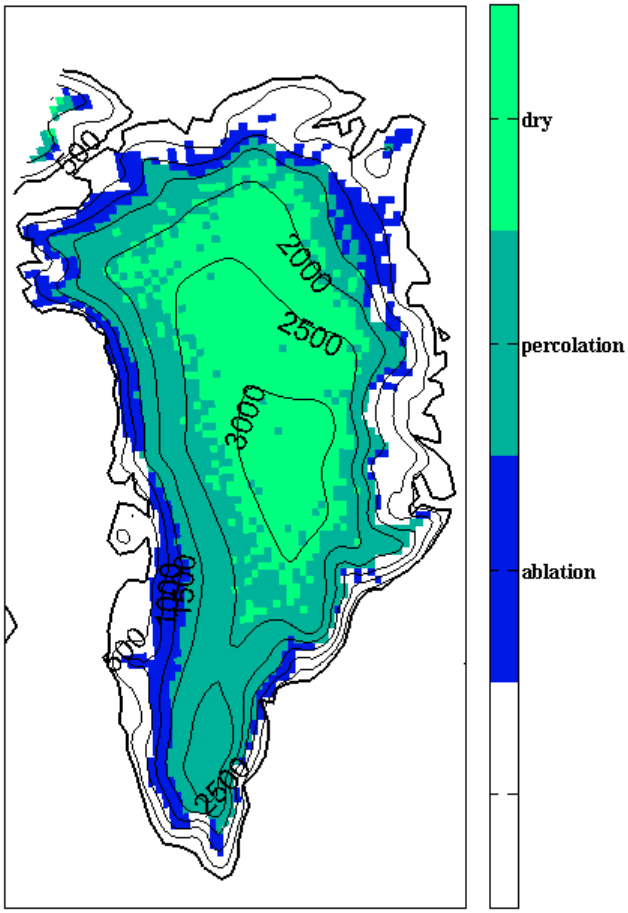

Figure 3.1: The Greenland ice sheet mask (filled area), including the ablation zone (blue), the percolation zone (dark green), and the dry snow zone (bright green) based on an offline CROCUS simulation for the year 2010. The contour lines show the topography of the ice sheet with an interval of 500 m.

The first data set (Figure 3.2a) is the MOD29 IST product of Greenland available online at (http://modis-snow-ice.gsfc.nasa.gov/?c=greenland). This product was developed based on Terra-MODIS clear-sky swath data obtained at 17:00 ± 3:00 UTC (14:00 ± 3:00) local time using the algorithm developed by Key and Haefliger (1992) and Key et al. (1997) for the MODIS sea ice product (i.e. MOD29 and MYD29). The MOD29 IST product uses data from Aqua-MODIS to fill the gaps due to instrument outages. An intensive automated and manual cloud correction

process has been employed to the data set to obtain high-quality clear sky IST. The daily MOD29 IST data set has been stored in a polar stereographic grid at 1.5 by 1.5 km and is available in binary and GeoTIFF format from Jan. 2000 to Dec. 2014. The reader is referred to Hall et al. (2012, 2013) for detailed information on the product. This product is a unique high-quality daily ice surface temperature data set which makes it suitable for data assimilation processes over the GrIS. However, the major drawback of using this data set is that there is no accurate acquisition time and data have been acquired from different satellite overpass within ± 3 hours of 17:00 UTC. Furthermore, Hall et al., (2012) reported a cold bias of ~3 K using short period in situ measurements at the Summit station.

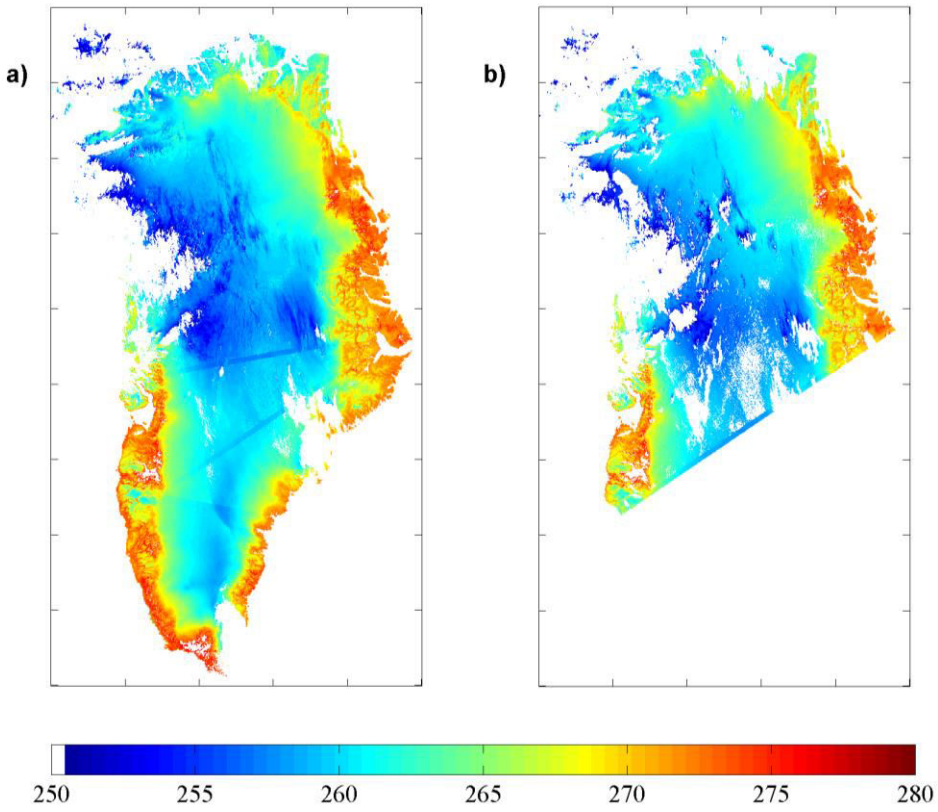

Figure 3.2 Ice surface temperature over the GrIS on May 15, 2009 (a) the first data set obtained at 17:00 ± 3:00 UTC, (b) the second data set obtained at 17:00 ± 1:00 UTC

The second data set (Figure 3.2b) is similar to the first data set, but it was developed based on Terra-MODIS clear-sky swaths data obtained at 17:00 ± 1:00 UTC which has been generated specifically for this study at NASA Goddard Space Flight Center (Hall, personal communication). This data set contains a more accurate acquisition time because it just uses swaths within ±1 hour of 17:00 UTC. One drawback, however, is that there are less high quality clear-sky daily observations within ±1 hour than ±3 hour. In addition, Terra orbit tracks over the GrIS at 17:00 ± 1:00 UTC distributed over the northern part of the GrIS (between ~80ºN-85ºN) which means the Terra-MODIS sensor at this time windows does not cover the southern part of the GrIS in many overpasses (Figure 3.2b). Therefore, significant information in the southern part of the GrIS where most of the melt happens is missing in the second data set. The two data sets were carefully combined to obtain the maximum number of measurements with relatively accurate measurement time. For each day the IST 17:00 ± 1:00 UTC data was used as the main data set and then the missing data (the areas of the southern part of the GrIS that has been cut off in the IST 17:00±1:00 data) was replaced with that of data from IST 17:00±3:00 data.

To estimate an approximate acquisition time for the measurements obtained from the first data set (i.e. data within ± 3 hours of 17:00 UTC) the Terra orbit tracks data (available at https:;//www.ssec.wisc.edu/datacenter/terra) was investigated. It was found out that the Terra data which covers the southern part of the GrIS has an overpass time of 15:00±1:00 UTC which is within the 17:00±3:00 time span. The approximate acquisition time for data obtained from the IST 17:00±1:00 was set to 17:00 UTC and for the data obtained from IST 17:00±3:00 acquisition

time was set to 15:00 UTC. This data set hereinafter is referred as MOD-IST-GrIS. It is clear that these approximate acquisition times will introduce uncertainties into the data assimilation framework which cannot be quantified.

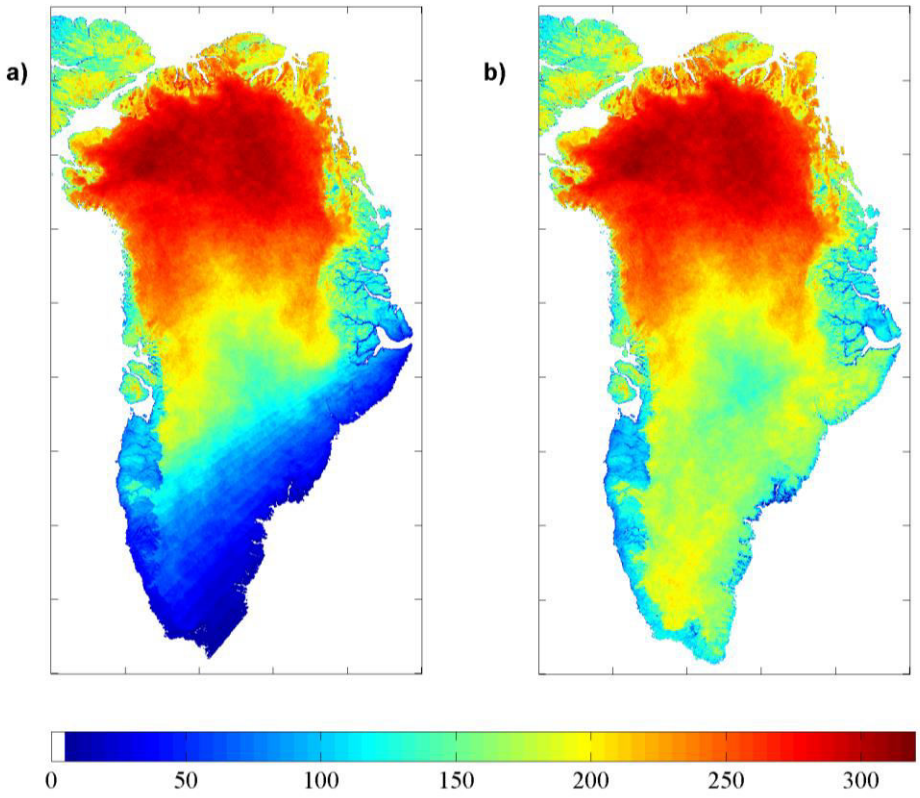

Figure 3.3: (a) number of IST measurement obtained at 17:00 ± 1:00 UTC, (b) number of IST observations for the combined data sets. The colorbar shows the number of IST measurements over the one year.

3.3.2.2 Passive microwave brightness temperature data

Passive microwave observations from the Advanced Microwave Scanning Radiometer - Earth Observing System (AMSR-E) were used for validation of results in this study. Passive microwave data are available in 12 channels, six frequencies (i.e. 6.9, 10.6, 18.7, 23.8, 36.5, and 89GHz) approximately twice per day (on ascending/descending passes) with a resolution that

varies as a function of frequency. The data is available in Equal-Area Scalable Earth Grid (EASE-Grid) at a nominal resolution of 25 km. It is worth noting that resampling the passive microwave data from their native footprint resolution into the EASE-Grid would smooth out the information content of the passive microwave signals especially for the 36.5 and 89 GHz channels. Because the footprint area of 36.5 GHz channel is 87.9 km^2 which is seven times smaller than the EASE-Grid area of 625 km^2. Li et al., (2012; 2015a; 2015b) used passive microwave brightness temperature to characterize the deep mountain snowpack and reported that using the 37 GHz V-pol data from AMSR-E in its native footprint resolution significantly outperforms the EASE-Grid data. The initial reanalysis (described in more detail below) was conducted on the nominal atmospheric model grid, which is of the same order as the cells in the EASE-Grid (25 km). Furthermore, it should be reminded that resampling the data from EASE-Grid into the MAR grid also introduces some error into the data set.

3.3.2.3 Near-surface meteorological data

The snow/ice model (CROCUS) applied in this study, uses the meteorological data obtained from the hourly MAR simulation for the year 2009 and 2010. In a data assimilation approach, the forward model needs an ensemble of forcing variables. Here, the nominal forcings from MAR integration were perturbed to generate the ensemble of the prior methodological forcing variables (i.e. P^-, R_s^-, R_l^-, T_a^-). The prior forcings were used as input to CROCUS to generate prior estimates of mass loss fluxes which are the main components of reanalysis estimates of mass loss.

3.4 Experimental design

The model setup and data assimilation steps are very similar to that explained in Navari et al., (2015). Hence, for brevity, only the key points are repeated here. In order to adjust the initial states of the snow/ice model to quasi-stationary condition, one-year model spin-up was performed. CROCUS was integrated forward in time using an ensemble of forcing data and nominal initial snow/ice profile from MAR. Then the ensemble of evolved snow profiles at the end of the spin-up simulation were used as initial profiles for prior (open-loop) and posterior simulations. Note that, for the both 2010 prior and posterior simulations, the snow/ice profile from the end of the 2009 posterior simulation was used.

A data assimilation analysis is performed for the two-year period from January 2009 through December 2010. The year 2009 and 2010 were chosen since the hydrological year 2009-2010 was characterized by an extreme negative SMB of 2.6 standard deviations below the 1958-2009 average (Tedesco et al., 2011). Moreover, the IST record also shows that the GrIS has experienced a large positive IST anomaly in all seasons during 2010 (Hall et al., 2013). It should be noted that these are two years for which hourly MAR outputs were readily available.

The feasibility of conditioning the GrIS surface mass fluxes using synthetically generated IST measurements based on a real temporal frequency of satellite-derived IST in an EnBS framework has been shown in our previous study. In this study, satellite-derived IST measurements have been used to generate reanalysis estimates of the GrIS surface mass fluxes via conditioning the forcing variables.

The measurement error standard deviation dictates how much the IST measurements are trusted relative to the prior estimate of IST in the assimilation step. The measurement error standard deviation at the simulation grid resolution (i.e. 25 km) depends (among other factors) on sensor spatial resolution and accuracy. In this study, IST measurement errors are assumed white Gaussian, with a standard deviation of 3 K. Although, there is not enough in situ IST measurements to validate the accuracy of the assumed measurement error standard deviation across the GrIS, different measurement error standard deviations can be investigated.

3.5 Data assimilation results

3.5.1 Illustrative results for updating surface temperature

3.5.1.1 Single Pixel data assimilation experiments

A straightforward method to evaluate the assimilation scheme is to explore the agreement between the posterior estimates of surface temperature with the satellite-derived IST. In theory, an effective data assimilation framework should transfer information from measurements into posterior estimates during the update step. As a result, the central tendency of posterior estimates should be in better agreement with the measurements than that of the prior estimates. Furthermore, the posterior ensemble spread (an indicator of uncertainty in the estimates) should be smaller than the prior ensemble spread. If this is not the case, then it should be either due to a very small Kalman gain or should be due to a near-zero innovation term which is defined as a difference between the predicted measurement and measurement (Forman et al., 2012).

For illustrative purposes, satellite-derived ISTs and predicted prior and posterior surface

temperatures for sample pixels (i.e. pixels that co-located with JAR2, JAR1, Swiss camp GC-Net stations) in the ablation zone is presented in Figure 3.4a-f. These pixels hereinafter referred to as JAR1 pixel, JAR2 pixel, and Swiss cap pixel, respectively. This figure graphically illustrates how the EnBS uses the information in measured IST to update the prior estimates of surface temperature from the snow/ice model. As can be seen, EnBS moves the prior estimates toward the measurements and the posterior estimates are in better agreement with the IST measurements. The ensemble spread is a measure of confidence in the estimates. Here, interquartile range (the difference between the third and the first quartiles) has been used to demonstrate the distribution of the prior and posterior estimates of the ensemble members. The prior estimates of surface temperature have a larger spread, reflecting the uncertainty of the prior estimates; on the other hand, the posterior estimates have a narrower spread which shows how EnBS improves the confidence of the posterior estimates.

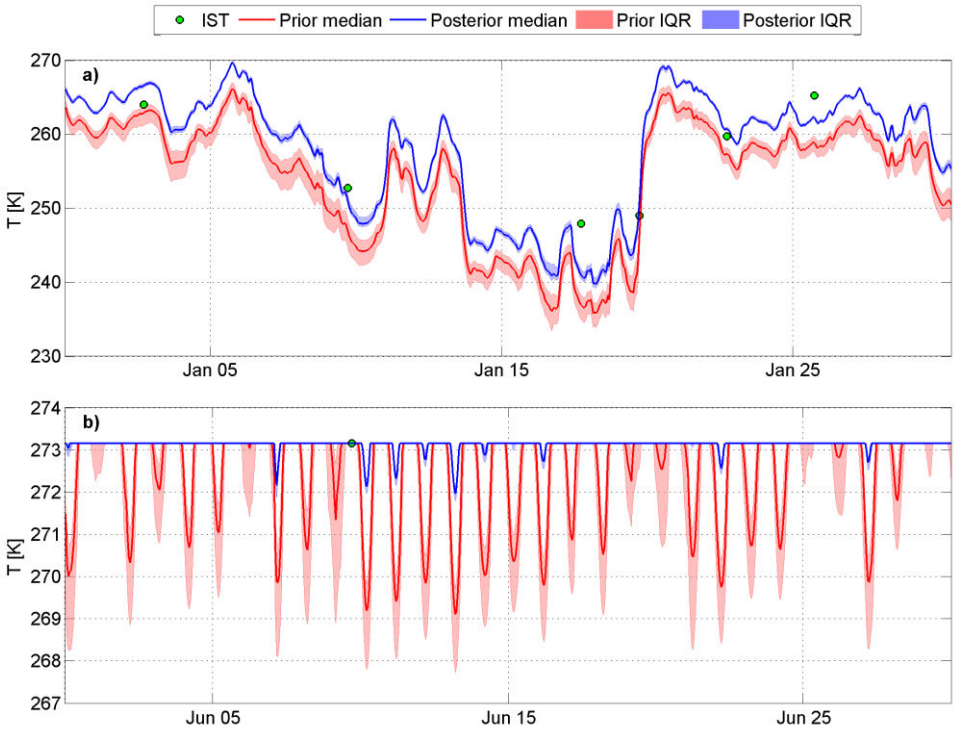
IST
Prior median
Posterior median
Prior IQR
Posterior IQR
a)
T [K]
270
260
250
240
230
Jan 05
Jan 15
Jan 25
b)
T [K]
274
273
272
271
270
269
268
267
Jun 05
Jun 15
Jun 25

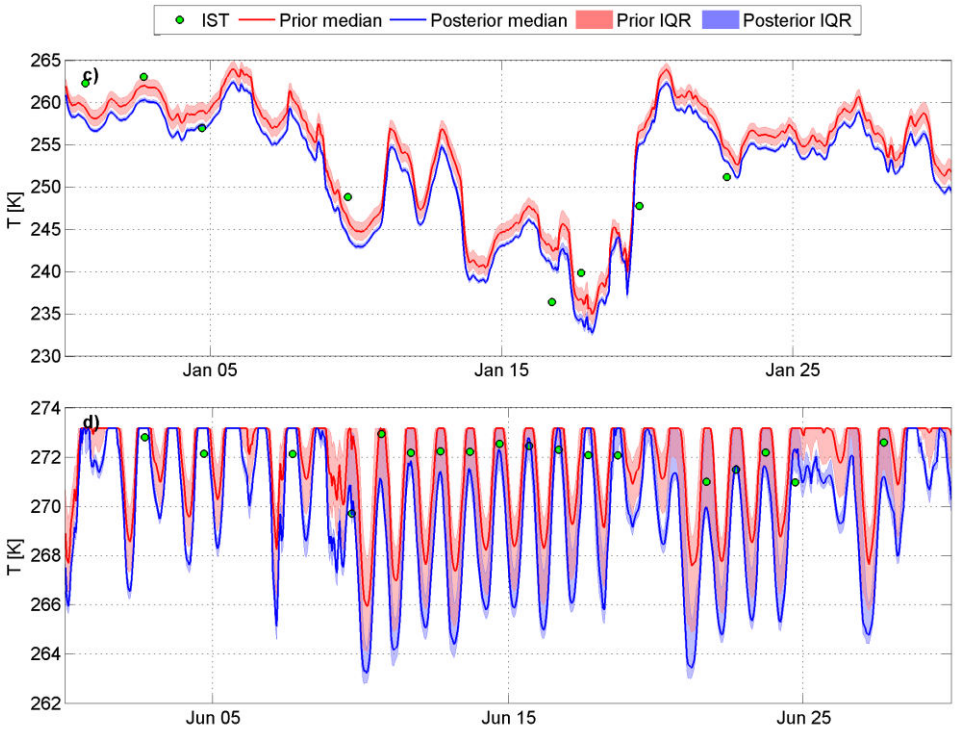
IST
Prior median
Posterior median
Prior IQR
Posterior IQR
c)
T [K]
265
260
255
250
245
240
235
230
Jan 05
Jan 15
Jan 25
d)
T [K]
274
272
270
268
266
264
262
Jun 05
Jun 15
Jun 25

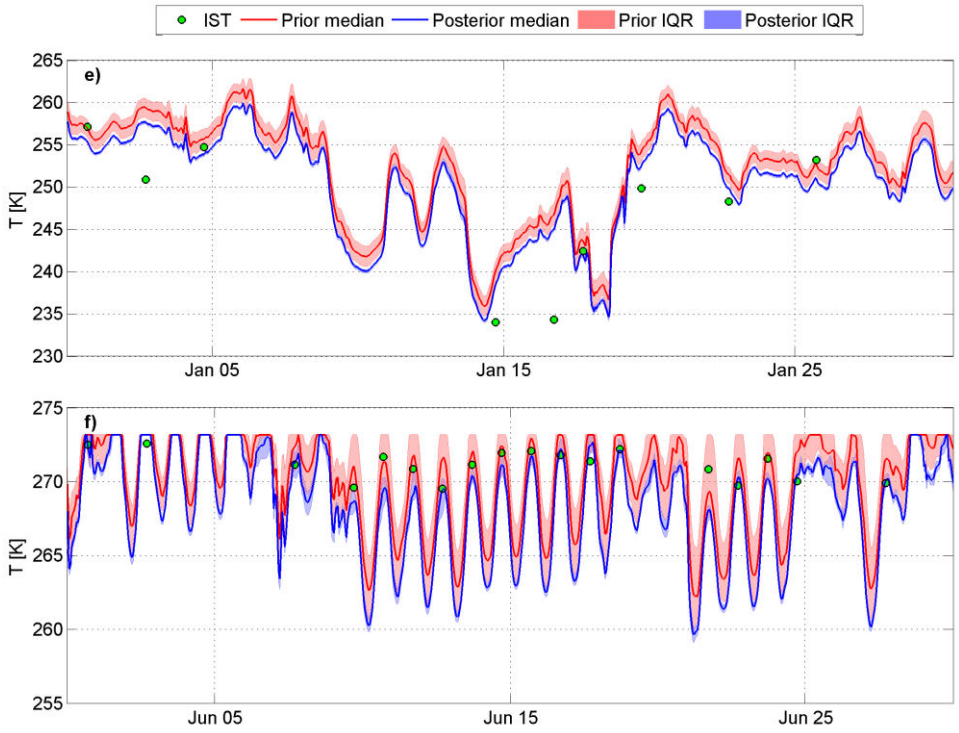

Figure 3.4 (a) the IST during the dry season (January) and (b) during the melt season (June) for the JAR2 pixel. The red and blue shaded areas represent the prior and the posterior uncertainty band (interquartile range) and the red and blue lines represent the median of the prior and the median of the posterior respectively. The green circles represent the IST measurements that are assimilated to generate the posterior estimates. The (c and e) similar to (a) but for the JAR1 pixel, and Swiss camp pixel. The (d and f) similar to (b) but for the JAR1 pixel and Swiss camp pixels.

The scatter plots of IST measurements versus predicted surface temperatures (i.e. prior and posterior) can be used to further evaluate the assimilation scheme. Figure 3.5a-c shows the scatter plots of IST data versus ensemble median of the prior and posterior estimates of surface temperature for the three pixels that co-located with the GC-Net stations (JAR2 pixel, JAR1 pixel, Swiss camp pixel). At the JAR2 pixel, almost all data points from the prior estimates are above the 1:1 line indicating that CROCUS underestimates the surface temperature. In contrast, the posterior estimates of surface temperature are fairly distributed around the 1:1 line reflecting

the fact that the data assimilation system shifts the data points toward the 1:1 line and reduces the bias. The trend lines also show that the posterior result is in better agreement with the IST. At the JAR1 pixel and Swiss camp pixel, the prior tends to overestimate the surface temperature and the data assimilation system shifts the prior toward the lower temperature to better match the 1:1 line. These results indicate that how the data assimilation system effectively reduces both the positive and negative bias in the adjacent pixels.

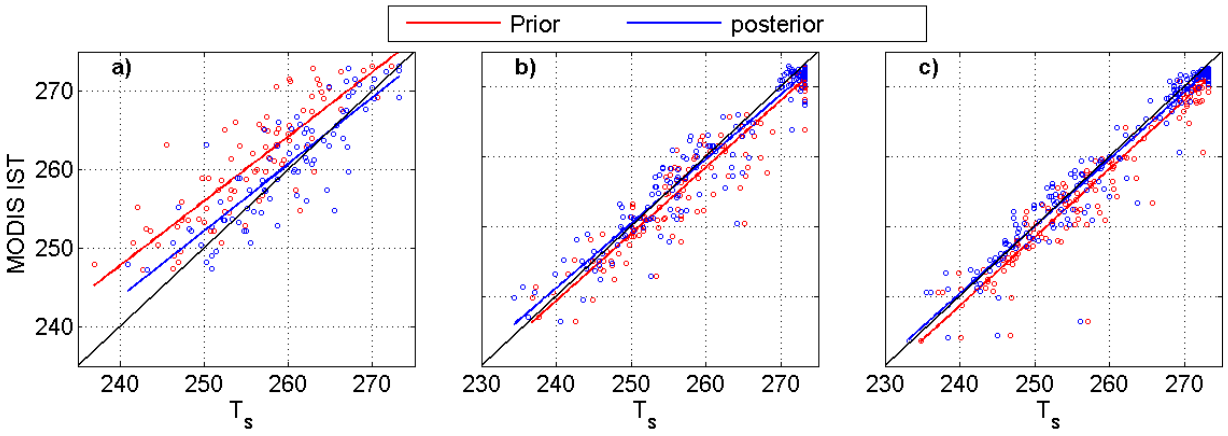

Figure 3.5 Scatter plots of satellite-derived IST measurements versus the prior and posterior surface temperatures from CROCUS, (a) for the JAR2 pixel, (b) for the JAR1 pixel, and (c) for the Swiss camp pixel. The red and blue circles represent the prior and posterior estimates respectively and the red line and the blue line represent the regression lines for the prior and posterior data points. The black line represents the 1:1 line.

Two distinct features can be detected in the scatter plots, including a) presence of outliers (i.e. the data with significant negative bias) in the satellite-derived IST data set which most likely could be due to the cloud contamination; b) the prior and posterior regression lines are not parallel to 1:1 line, means that CROCUS underestimates the surface temperature in lower temperatures and overestimates the surface temperature close to the melting point.

3.5.1.2 Distributed data assimilation experiments

The ability of the EnBS framework to update the surface temperature over the entire domain was evaluated using the RMSE, MAE, and an improvement metric κ. The EnBS reduces the spatial mean RMSE (MAE) of the posterior estimates of surface temperature about 69% (62%) from 1.1 K (0.7 K) to 0.3 K (0.3 K). The improvement metric is given by:

$$\kappa(\tau) = \left|T_s^{prior}(\tau) - IST(\tau)\right| - \left|T_s^{posterior}(\tau) - IST(\tau)\right| \qquad (3.9)$$

where $\kappa(\tau)$ represents the improvement metric at measurement time τ, T_s^{prior} and $T_s^{posterior}$ are the ensemble median of the prior and posterior estimates of surface temperature, respectively, and IST represents the satellite-derived IST measurements. The metric κ represents the contribution of the assimilated satellite-derived IST to the posterior estimates of the modeled surface temperature obtained from integration of CROCUS using updated forcings. This metric is positive if EnBS improves the IST; it is zero if EnBS does not update the surface temperature, and it is negative if EnBS degrades the surface temperature. The improvement metric was computed at the IST measurement time across the domain and then averaged over time. Figure 3.6a-c shows the mean of the improvement metric over the GrIS. EnBS improves (i.e. κ >0) the surface temperature in 57%, 68%, and 69% of the computational pixels using a measurement error of 1 K, 3 K, and 5 K respectively. The ensemble median of the posterior surface temperatures is in better agreement with the measured IST in the GrIS margin where most of the melt occurs. EnBS improves the surface temperature in about 77%, 87%, and 89% of the grid cells in the ablation zone using a measurement error of 1 K, 3 K, and 5 K respectively. In some pixels the algorithm

does not update the surface temperature or slightly degrade (i.e κ<0) the surface temperature. The main question is whether the negative κ value means model degradation or not.

The posterior error of surface temperature in some pixel is slightly larger than the prior error relative to IST measurement, which leads to a negative κ value (shown in blue color in Figure 3.6a-c). However, it would be instructive to statistically evaluate these negative values. A hypothesis test was performed to evaluate the significance of differences between the prior and posterior estimates of surface temperatures, which lead to the negative κ values. A two sample *t*-test was carried out to test the null hypothesis that the mean of the ensemble of the prior and posterior are the same. In particular, the *t*-test was conducted to determine: if there is sufficient evidence at the 0.05 level to conclude that the ensemble mean of the prior estimates of surface temperature differs from the ensemble mean of the posterior estimates of surface temperature. The *t*-test was applied to all pixels with a negative κ value. The results were statistically insignificant and the null hypothesis was accepted. The results show that at the 95% confidence interval, less than 0.3% of the pixels reject the null hypothesis. Therefore, it can be concluded that, statistically, the mean of the posterior estimates of surface temperature at the pixels where the κ metric is negative is the same as the mean of the prior estimates.

It is worth noting that, the DA was run for three different measurement errors standard deviation of 1 K, 3 K, and 5 K, and prior and posterior were compared against IST. Results revealed that by increasing the measurement error standard deviation, the number of pixels with no improvement or negative κ value considerably decreases. However, by increasing the

measurement error standard deviation from 3 K to 5 K the number of pixels with positive κ to the total number of pixels improves by 1% on the other hand, the spatial mean of the κ value decrease by 5%. Therefore, we chose to use a measurement error standard deviation of 3 K in this study. A similar measurement error standard deviation has been reported by Bateni and Entekhabi (2012) using land surface temperature data from MODIS (i.e., data from the same sensor).

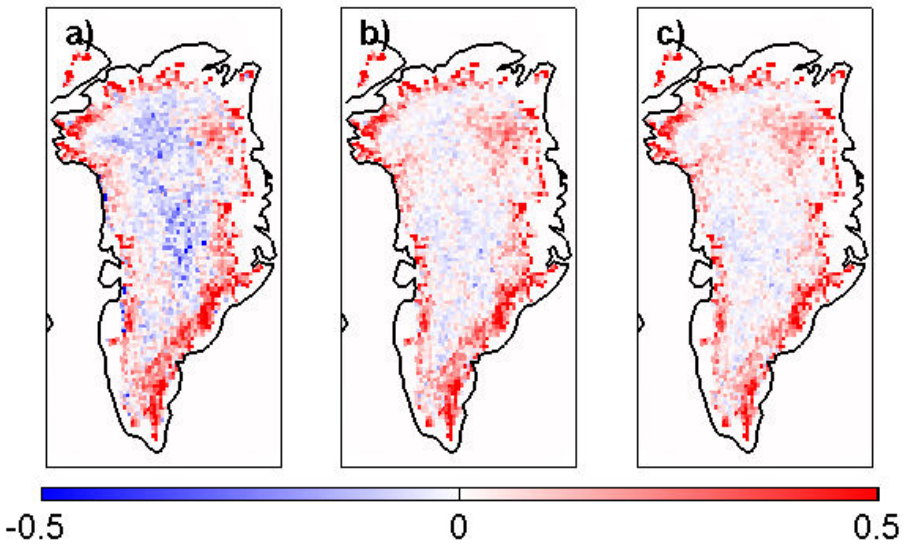

Figure 3.6 Maps of mean surface temperature improvements in [K] over the GrIS for (a) a measurement error of 1 K, (b) a measurement error of 3 K, and (c) a measurement error of 5 K. The red color represents a positive improvement. The white color represents no improvement, and the blue color represents the negative κ value which statistically means no improvement

Figure 3.7a and 3.8a show the mean IST over the GrIS for the year 2009 and 2010. It can clearly be seen that the ice sheet margin experiencing relatively warmer temperature, especially in the west and south-east. Figure 3.7b-c and 3.8b-c show the mean surface temperature error for the prior (i.e. prior - IST) and the mean surface temperature error for the posterior (i.e. posterior -

IST). The prior error map shows that the open-loop model considerably underestimates/overestimates surface temperatures, especially in the ice sheet margin where the melt occurs. The model underestimates the surface temperature in the ice sheet interior and overestimates the surface temperature in the ice sheet margin. Figure 3.7c and Figure 3.8c show that the posterior error is significantly smaller than of the prior error indicating that the data assimilation system effectively reduces the positive and negative biases in the prior estimates. It is important to emphasize that in this study, unlike many data assimilation applications the surface temperature (model state) has not been directly updated by conditioning the model surface temperature on satellite-derived IST, instead, the forcing data has been updated and the posterior estimates of surface temperature were obtained by integrating the CROCUS in time using the posterior forcings. Since surface temperature is the most important factor that regulates partitioning of the net radiation into the subsurface snow/ice, sensible and latent heat fluxes and plays a key role in the generation of runoff (Hall et al., 2013), therefore, it can be expected that a better estimate of surface temperature from a data assimilation system contributes to a better estimate of surface mass fluxes. Figure 3.7c and Figure 3.8c demonstrate that a) IST data contains valuable information to update the forcing variables; b) EnBS can effectively extract and use this information to estimate the surface temperature.

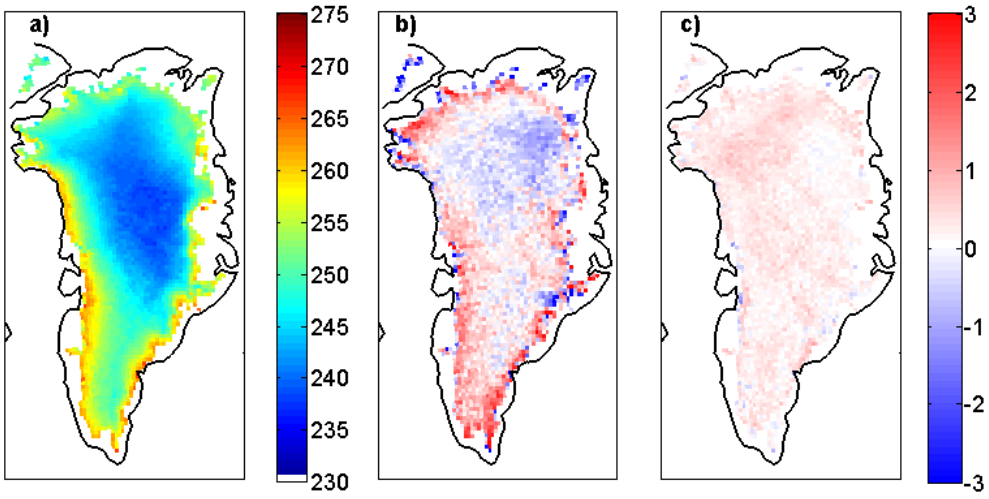

Figure 3.7 (a) mean IST [K] for 2009, (b) mean surface temperature error [K] for the prior (i.e., difference between the prior surface temperature and satellite-derived IST), (c) mean surface temperature error [K] for the posterior.

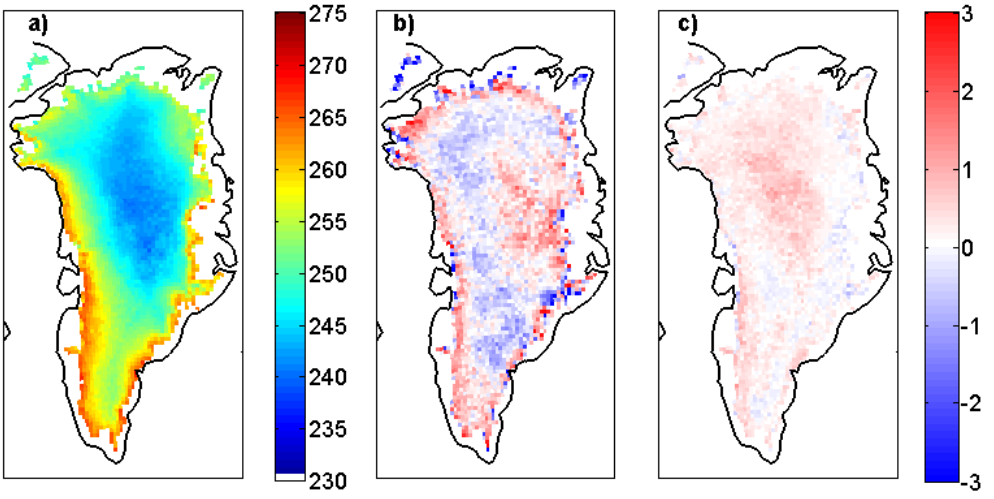

Figure 3.8 the same as Figure 3.7 but for 2010

3.5.2 Illustrative results for SML fluxes

EnBS transfers the information content of satellite-derived IST into the posterior estimates

of surface mass fluxes via updating the forcing variables. Here, the posterior estimates were compared against the prior estimates since there is no knowledge of the true fluxes. Figure 3.9-a and 3.10-a shows time series of the prior and posterior estimates of runoff for the year 2009(2010). As can be seen, the prior runoff is 97(144) mmWE which is significantly smaller than the posterior runoff estimates of 150(205) mmWE. By conditioning the model on real IST measurements, EnBS corrects a perceived bias in the forcing variables and propagates the correction to the posterior estimates. Bias-corrected forcings from the data assimilation suggest about 54% (42%) more runoff than the prior estimates for the year 2009 (2010). The prior and posterior simulations also provide an uncertainty estimate of the runoff. The lower and upper bounds of the light blue and light red bounds in Figure 3.9a and Figure 3.10a correspond to the 25^{th} and 75^{th} percentile (i.e., interquartile range) of the ensemble estimates of the prior and posterior simulations respectively. The uncertain forcings in the prior simulation lead to a large ensemble spread as shown in light red. Assimilation of IST measurements reduces the uncertainty of the runoff from the posterior simulation (illustrated in light blue).

Evaporation, sublimation, and surface condensation are known as turbulent fluxes that play an important role in the GrIS mass loss. Sublimation occurs through two main processes over the GrIS, including a) surface sublimation, and b) drifting snow sublimation which is very important in dry and windy conditions. Lenaerts et al., (2012) reported an average surface sublimation of 16 $Gtyr^{-1}$ and an average drifting snow sublimation of 24 $Gtyr^{-1}$ during the 1960 to 2011 period. The CROCUS turbulent flux module does not have the capability to take into account snow drift

sublimation; therefore, this flux was ignored in estimates of surface mass fluxes. The sum of sublimation, evaporation, and surface condensation was used as an integrated mass loss term, which hereinafter is called turbulent fluxes. Figure 3.9b and 3.10b shows the cumulative mass loss of the GrIS through the turbulent fluxes. The posterior estimates suggest a turbulent mass loss of 18 (22) mm for the year 2009 (2010) which are very close to the prior estimates of 22 mm (25 mm), however, smaller spread represents increased confidence in the mass loss estimates via turbulent fluxes. The assimilation of IST measurements reduces the uncertainty in the posterior estimates of the turbulent fluxes as presented by the narrow blue band in Figure 3.9b and 3.10b.

Now, the GrIS SML can be computed by adding the runoff and turbulent mass loss. Figure 3.9c and 3.10c show the cumulative time series of the GrIS SML for the year 2009 and 2010. The data assimilation algorithm estimates a total SML of 169 mmWE, 228 mmWE for the year 2009 and 2010 respectively, which are 42% and 35% larger than the prior estimates. In addition, EnBS reduces the uncertainty of the posterior estimates about 70% and 75% for the year 2009 and 2010 respectively. In general, assimilation of IST measurements has two main impacts on the prior estimates: a) reduction of the bias by shifting of the ensemble median of the prior and b) reduction of the prior uncertainty.

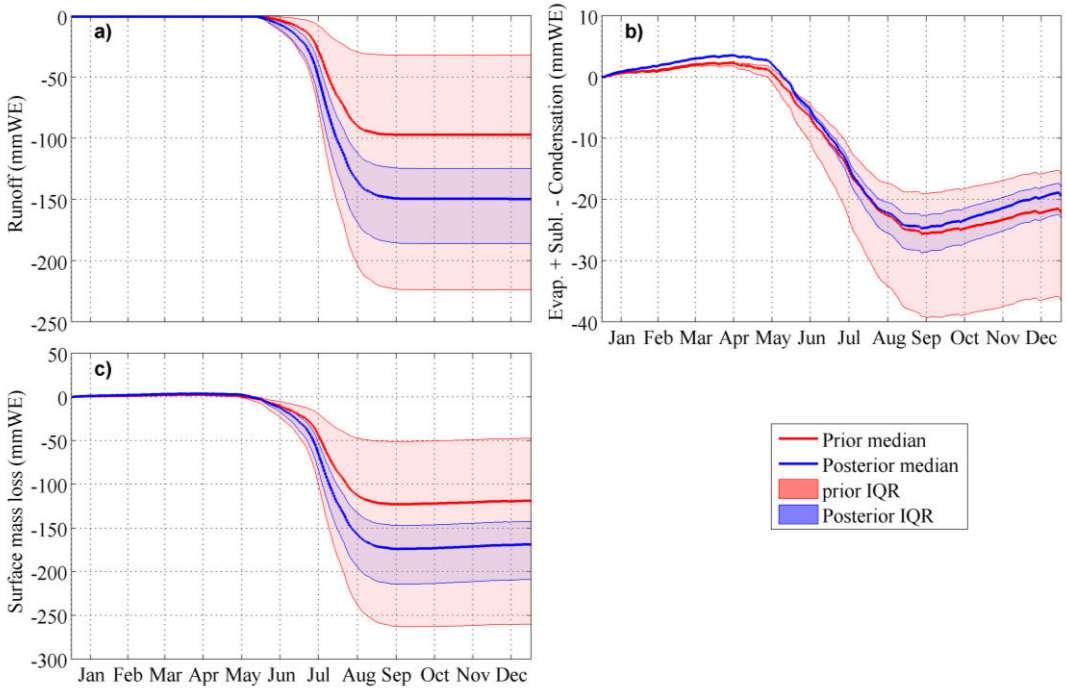

Figure 3.9 Time series of (a) cumulative runoff, (b) cumulative mass loss through evaporation, sublimation, and surface condensation, and (c) cumulative mass loss over the GrIS (in millimeters of water equivalent) for 2009. The prior ensemble median is the red line and the posterior ensemble median is the blue line. The red shaded area corresponds to the ensemble interquartile range (IQR) for the prior simulation and the blue shaded area corresponds to the ensemble IQR for the posterior estimates.

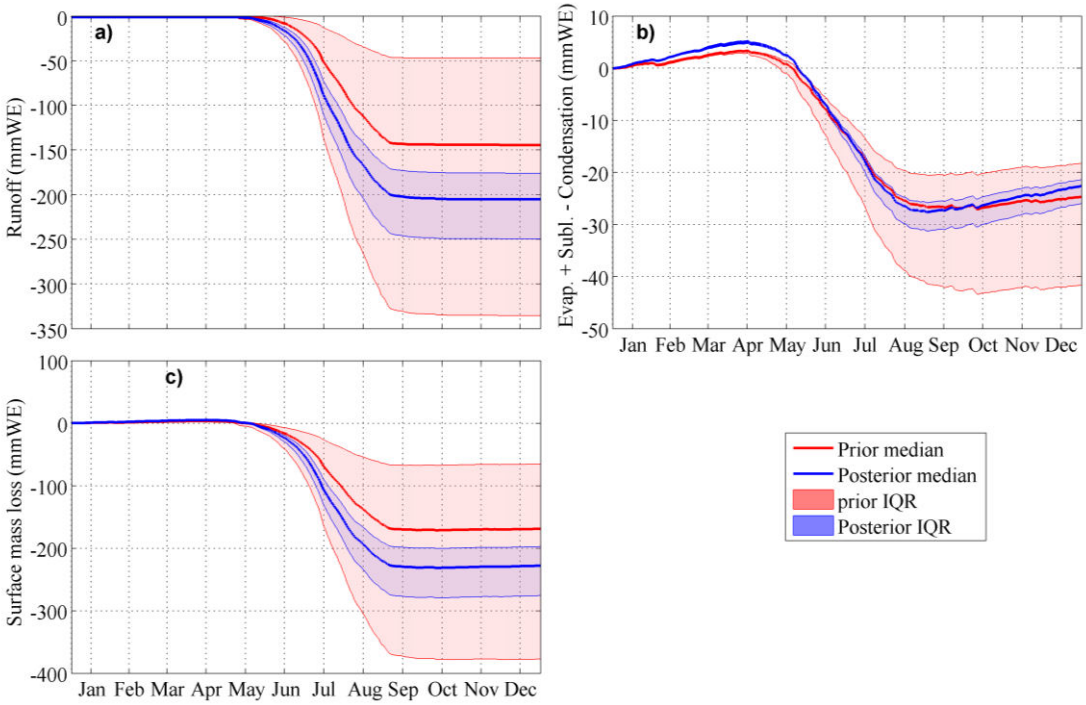

Figure 3.10 the same as Figure 3.9 but for 2010

3.5.3 The effect of cold bias on surface mass fluxes

Hall et al., (2012) reported a cold bias of ~3 K using short period in situ measurements at the Summit station. The cold bias was detected under clear skies when the surface temperature was between -50ºC to -30ºC, therefore, this bias might be site dependent and temperature dependent. While there are not enough in situ measurements to verify the reported cold bias over the entire GrIS, investigating the effect of this cold bias on surface mass fluxes would be informative. The cold bias was removed from the IST measurements by increasing all measurements by 3ºC and the bias corrected IST was assimilated into the MAR forcing variables. CROCUS was run for several pixels over the different mass balance zones using updated forcings from the data assimilation. Results (not shown) indicate that removing 3ºC bias from the IST measurements while keeping all measurements at or below the freezing point significantly increases the surface mass loss in all pixels across the different mass balance zones with an extensive mass loss in the ablation zone. It is clear that increasing the temperature in the ice sheet margin where the summer temperature is close to the melting point would significantly impact the meltwater production and mass loss. In the interior area where the mean summer temperature is very low (i.e., less than -25ºC) increasing the IST is more likely to impact the mass loss through the turbulent fluxes. Results highlight that removing the cold bias from IST measurements can potentially increase the GrIS SML. Since the IST product is under development more effort is needed to characterize the bias and uncertainty of this product.

3.6 Assessment and verification

Assessment and verification of the results are a critical part of this study but are heavily limited by the lack of suitable verification data sets. In this section, the feasibility of using several potential data sets for verification of data assimilation results was investigated.

3.6.1 Melt extent and melt duration

3.6.1.1 Satellite-derived melt extent and melt duration over the GrIS

Melt extent and melt duration can be used as potential criteria to evaluate the data assimilation results over the GrIS, albeit in a limited way. In this study melt extent and melt duration from AMSR-E using the DAV algorithm was compared with that from CROCUS. We chose to use DAV because DAV is a straightforward retrieval algorithm that does not require field measurements to obtain the melt threshold parameters. The histogram of the brightness temperature over the GrIS can be used to determine the brightness temperature threshold. The histogram of the measured brightness temperature in areas that experience melt shows a bimodal distribution. The lowest population between the two peaks represents the threshold between dry snow and wet snow (Ramage and Isacks, 2003). The histograms of the brightness temperatures for the year 2009 and 2010 were constructed using all observations over the ablation and percolation zones. A brightness temperature corresponding to the lowest population between the two peaks for the year 2009 and 2010 was 251 K and 249 K respectively. In this study, a DAV threshold of ±18K was adopted from Tedesco (2007) and Apgar et al., (2007). The melt extent and melt duration for 2009 and 2010 were obtained by applying the DAV method to the

AMSR-E data.

3.6.1.2 Melt extent and melt duration from CROCUS-MEMLS

To apply the DAV method to the CROCUS output, snow layer properties required to be translated into the brightness temperature. The microwave emission model of layered snowpack (MEMLS: Matzler and Wiesmann, 1999; Wiesmann and Matzler, 1999) can be utilized to estimate the brightness temperature using snow layer properties. Estimates of the prior and posterior melt extent and melt duration need a coupled CROCUS-MEMLS system. However, generating prior and posterior ensemble estimates of brightness temperature by means of the coupled CROCUS-MEMLS are computationally expensive. Therefore, as a pilot study, the DAV method was applied to a deterministic CROCUS-MEMLS system. In this way, we tried to assess the feasibility of using the CROCUS-MEMLS system to predict the melt extent and melt duration. The same procedure that was used to estimate the satellite-based brightness temperature threshold was applied to the CROCUS-MEMLS output and a brightness temperature threshold of 265 K was obtained for the year 2009. For the DAV threshold (i.e. the threshold B) a sensitivity experiment was performed to obtain an optimum DAV threshold. It was found out that the results are not sensitive to the DAV threshold. This is more likely due to the fact that the changes in brightness temperatures due to the presence of liquid water in the snowpack are abrupt and larger than the range of the reported DAV threshold value of ±18K, hence, the same DAV threshold of ±18K was implemented to the CROCUS-MEMLS outputs.

Our preliminary findings indicate that the predicted melt extent (Figure 3.11c) and melt

duration (Figure 3.11a) is larger than the satellite-derived melt extent (Figure 3.11c) and melt duration (Figure 3.11b). An inability of the CROCUS-MEMLS system to accurately predict the brightness temperature is the main reason for this overestimation which has been discussed in more detail in chapter 4.

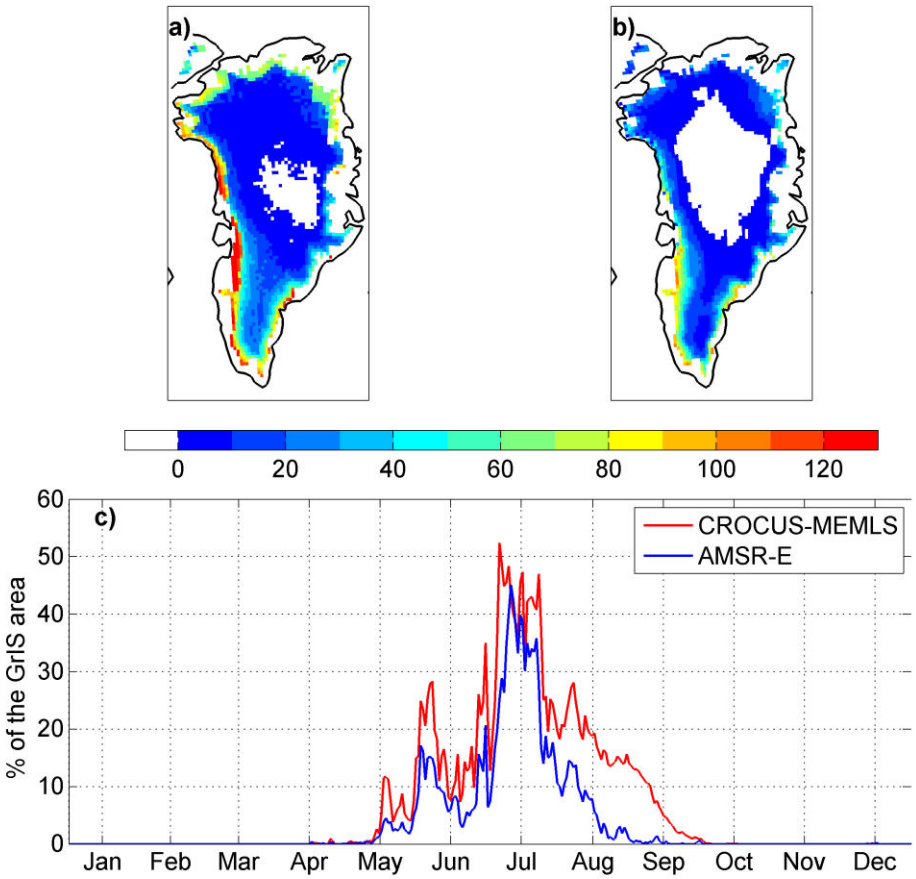

Figure 3.11 Melt extent and melt duration using DAV method, (a) map of melt extent and melt duration using CROCUS-MEMLS system, (b) map of melt extent and melt duration using AMSR-E data, (c) time series of melt extent from AMSR-E (blue) and from CROCUS-MEMLS (red).

3.6.1.3 Melt extent and melt duration using liquid water content in the snowpack

Another potential method to verify the results is using liquid water content of the snowpack as a criterion to detect the melt extent and melt duration. Modeled liquid water content (LWC) of

the snowpack has been used in several studies as a metric to diagnose melt. Abdalati and Steffen (1995) reported that a snowpack LWC of 0.5% by volume in the top one meter of snowpack is corresponding to sharp increases in XPGR using SMM/I data. Abdalati and Steffen (1997) increased the LWC threshold from 0.5% to 1% using the Scanning Multichannel Microwave Radiometer (SMMR) data. Fettweis et al., (2006) applied a LWC of 1% and Fettweis et al., (2011) applied a LWC of 1.1% to the top one meter of snow profile from MAR to estimate the melt extent and melt duration. It should be highlighted that, Abdalati and Steffen (1995, 1997) reported that a) the value of 1% in the top one meter is not a theoretically defined metric, b) this value is based on in situ data from ETH/CU camp (also called Swiss camp) and it might be site dependent, c) the threshold of 1% was used to be consistent with the other studies conducted by Mote and Anderson (1995), and d) emission depth of the wet snow with a LWC of about 2% is limited to about 2 cm and 8 cm for the 37 GHz V-pol and the 19 GHz H-pol respectively. Therefore, the wetness below the emission depth barely influences the microwave signals. The last point has also been reported by Matzler (2006).

To obtain a threshold for LWC and depth of wet snow, a set of experiments were performed using the MEMLS. Several snow profiles from the different mass balance zones were selected and LWC and depth of wet layers gradually increased while the other snow layer properties (i.e. layer density, layer temperature, layer height) kept constant. Results (not shown) revealed that there is an abrupt change in modeled brightness temperature when LWC increases from 0 to 0.2-0.5% and after that a further increase in LWC does not significantly change the modeled

brightness temperature. Therefore, a LWC of ~0.5% by volume can be set as a melt threshold. This threshold is in agreement with Abdalati and Steffen (1995) and Tedesco et al., (2006, 2007) which reported that the minimum detectable LWC ranges between 0.2 and 0.5%.

Sensitivity experiments on the thickness of wet layers showed that for a LWC of 0.2% and larger, the modeled brightness temperature shows an abrupt change when the thickness of the wet layer reaches ~1 cm and after that further increasing the wet layer thickness does not significantly change the brightness temperature. However, since the 37 GHz V-pol can see the liquid water under the frozen surface layers, it would be more realistic to look at the LWC in the wet layers not just the top 1 cm which might be frozen during the night (i.e. LWC=0).

Using a LWC threshold of 0.5% (by volume) and applying the threshold to the mean daily LWC of the snowpack, melt extent and melt duration were computed for the year 2009 and 2010 over the GrIS. As shown in Figure 3.12 and Figure 3.13 both the prior (Figure 3.12a and Figure 3.13a) and the posterior simulations (Figure 3.12b and Figure 3.13b) overestimate the melt duration in comparison with the satellite-derived values (Figure 3.12c and Figure 3.13c). However, time series of daily melt extent from both the prior and posterior are in good agreement with the daily melt extent from AMSR-E (Figure 3.12d and Figure 3.13d).

It seems that the usage of melt extent and melt duration is an overly bulk metric to evaluate the data assimilation results. The prior and posterior melt extent is almost identical even though the prior and posterior runoff is very different. It can be argued that the prior and posterior melt extent can be similar for different runoff values since changes in runoff values can be due to an

increase in melt energy during the melt period or due to an increase in the number of melting day in the same pixel which will not affect the melt extent. The other possible reason is the fact that a satellite-derived melt extent is based on instantaneous observation at which there might be no melt while the daily ensemble mean might show small melt. In general, melt extent and melt duration are significantly influenced by the LWC threshold and it seems that there is no physically based method to provide a robust LWC threshold.

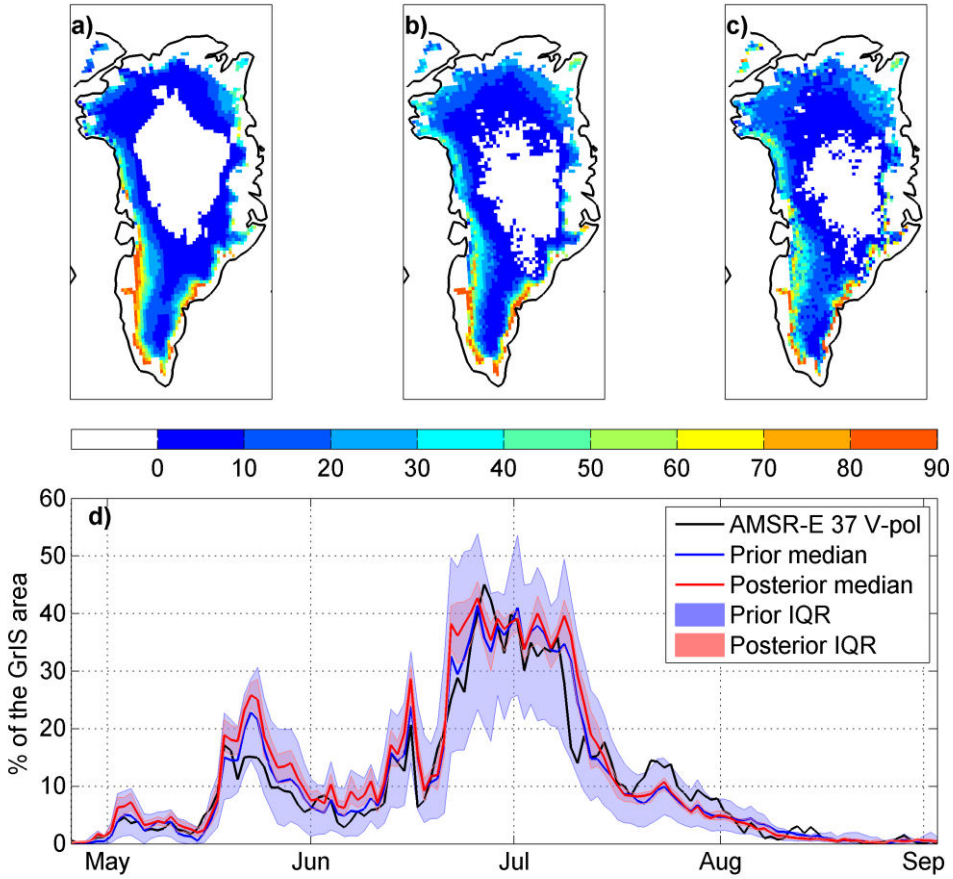

Figure 3.12 Maps of melt duration from (a) AMSR-E data using the DAV, (b) prior simulation using a LWC threshold of 0.5% by volume, (c) the same as (b) but for the posterior simulation. (d) time series of melt extent from AMSR-E data (black), the prior simulation (blue), the posterior simulation (red). The blue shaded area represents the interquartile range (IQR) of the prior estimates and the red shaded area represents the interquartile range of the posterior estimates

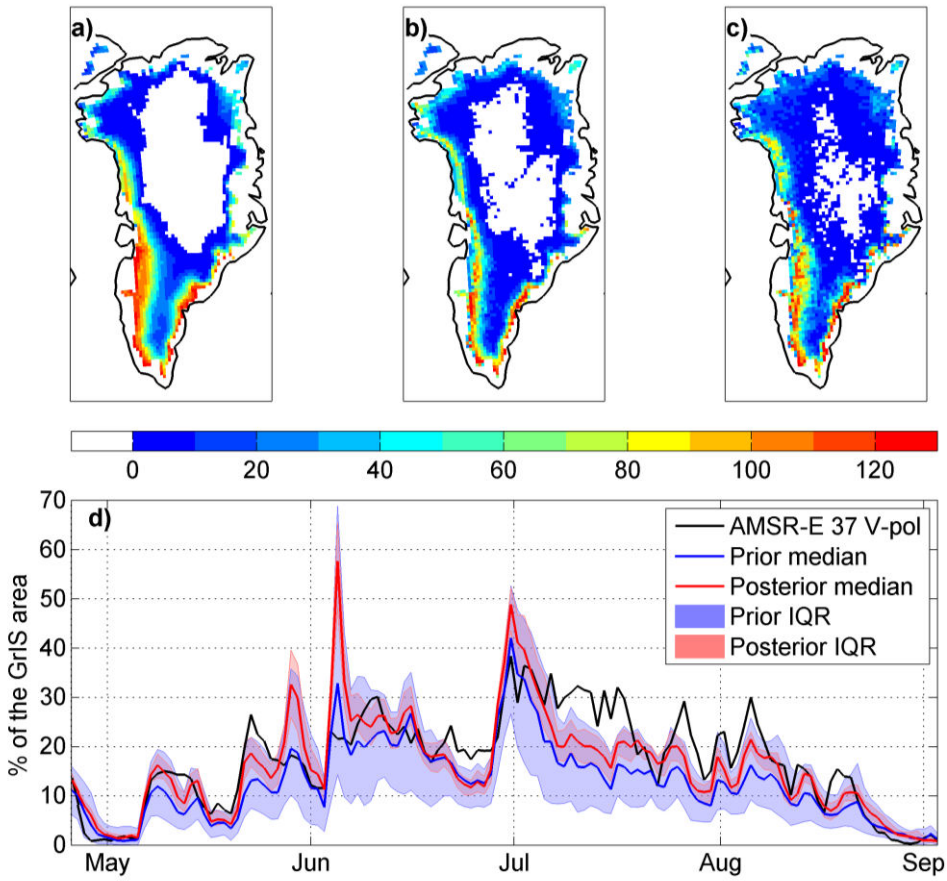

Figure 3.13 the same as figure 3.12 but for 2010.

3.6.2 K-transect SMB measurements

Since 1990 SMB measurements have been carried out at eight locations in southern Greenland (Figure 3.14), near the town of Kangerlussuaq at different elevations (van de Wal et al., 2012). This data set is the longest record of ground-based SMB measurements in Greenland. The measurements and adjustment of the stakes were conducted in late August every year. Among the stations, six stations are located in the ablation zone, one in the percolation zone and the last station in the accumulation zone. Here we compare the results of the prior and posterior SMB with SMB from K-transect measurements. As can be seen (Figure 3.15) the data

assimilation system provides better estimates of SMB in the ice sheet margin, but it fails to correctly estimate the SMB further inland. The prior model performs better in the inland pixels, but they are both significantly different from in situ measurements. A close inspection of surface temperature during the melt period shows that the posterior surface temperature is in better agreement with IST. However, there are significant differences between the observed and modeled SMB. There are a number of possible explanations for the observed discrepancy. The lead candidate for explaining this discrepancy is the fact that the S6, S7, and S8 stations are located in the GrIS dark zone (a narrow region stretched from 65ºN to 70ºN where the snow surface is darker than surrounding areas due to the higher concentration of impurities) (Wientjes et al., 2011). Therefore, an albedo feedback mechanism (Box et al., 2012) due to snow impurities and the fact that CROCUS does not take into account the snow impurities could be the main reason for significant differences between the modeled and measured SMB, particularly at the above-mentioned stations. The presence of liquid water in a different form (pond, lake, and stream) significantly decreases the albedo and further enhances melting. This phenomenon can be the main reason for differences between the predicted and measured SMB in the S9 station. Another reason might be inaccurate IST acquisition time as explained in Section 3.3.2.1. It was assumed that all measurements within 17:00 ± 1:00 have an acquisition time of 17:00 and all measurements within 15:00 ± 1:00 have an acquisition time of 15:00. Another possibility might be the uncertainty of IST data since this data set is still under development. Shuman et al., (2014) highlighted that the further development of the IST product should benefit from a better cloud

mask and an improved algorithm to take into account the cold bias. The CROCUS physics representation is imperfect; therefore model error can be another possible reason for the observed discrepancy. A comparison between the model elevation and real elevation in the K-transect stations shows that the model elevation is higher than the real elevation (i.e., 10 m to 75 m) which leads to less snow/ice melt.

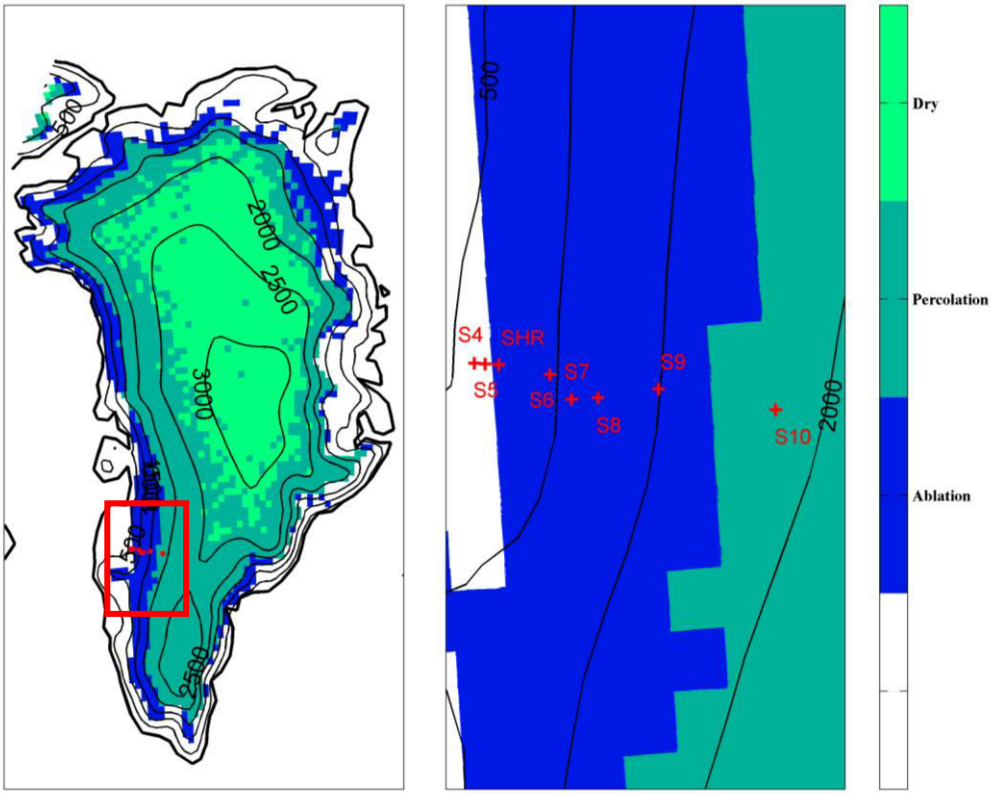

3.14 The location of the K-transect stations over the GrIS

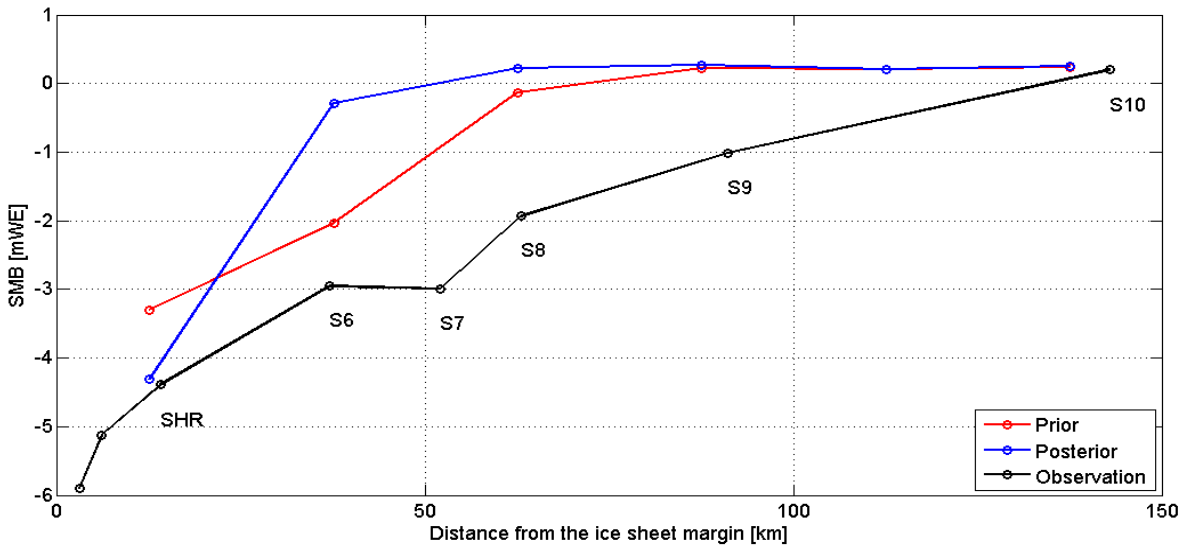

Figure 3.15 SMB at the K-transect stations, the black circles and the line show the in situ observation, the red and blue circles and lines are the prior and posterior SMB

3.7 Conclusion

In this work an EnBS data assimilation methodology was implemented to integrate the satellite-derived IST with the a priori estimate of forcing data from the MAR regional climate model aiming to generate reanalysis estimates of the GrIS surface mass fluxes. We showed that the EnBS is able to retrieve the surface temperature given the biased forcing data from MAR. Pixel scale comparison between the EnBS estimates and open-loop simulation demonstrates the advantages of assimilating IST measurements. Surface temperatures from the data assimilation results are closer to satellite-derived IST measurements than the open-loop estimates. Comparing the results over the GrIS showed that the EnBS reduces the both positive and negative biases in the prior estimates of surface temperature to better match the IST measurements. The results also

showed that the spatial mean RMSE and MAE of the posterior estimates are 69% and 62% smaller than that of the prior estimates relative to the IST measurements.

While a further verification of the results is critical, it is limited by the sparse amount of verification data set. Here, the feasibility of verification of results using several data sets was investigated. We compared melt extent and melt duration from our assimilation framework with that of passive microwave remote sensing data set. The well-known DAV method was applied to the both passive microwave data from AMSR-E and predicted brightness temperature from a deterministic CROCUS-MEMLS system. The CROCUS-MEMLS system overestimates the melt extent and melt duration in comparison with the results from satellite-derived passive microwave data, likely due imperfect CROCUS-MEMLS system.

We also used the snowpack LWC as a criterion to detect the melt extent and melt duration. Our results using mean daily LWC of 0.5% over the wet layers overestimates the melt duration while the time series of melt extent is in good agreement with the satellite-derived melt extent. It can be argued that the snowpack LWC is not a robust criterion to detect the melt extent and melt duration since both the LWC threshold and the depth of snowpack which the LWC has been measured can be tuned to better match the melt extent and duration from the passive microwave (see Section 3.6.1.3).

In general melt extent and melt duration are bulk metrics to be used for evaluation purpose. Moreover, runoff is not directly related to the melt extent and melt duration, for instance, an increase in albedo due to the presence of liquid water or exposed ice could increase the melt

while would not affect the melt extent and or melt duration.

We also used the K-transect point scale SMB measurements to assess our results. It was shown that EnBS significantly improved the results in the marginal pixel where the SHR K-transect station is located. However, it fails to improve the SMB of the pixel that encompass the S6, S7, and S8 stations. Since these three stations are located in the GrIS dark zone one possible reason could be melt anomaly due to higher albedo in this region. While the CROCUS albedo module cannot simulate impurities, satellite measurements provide valuable information about the spatial variability of albedo over the GrIS. This highlights the information content of albedo products and shows the value of assimilating albedo in future work.

While we acknowledge that EnBS might provide a suboptimal solution due to the nonlinearity of the system and the lack of enough measurements for assimilation, the other reason for suboptimal results could be a lack of accuracy of the IST measurements since this product is still under development. Future work should benefit from developing physically based criteria to be able to compare the results with passive microwave data or other remote sensing data in a more consistent way.

4 Feasibility of Radiance Assimilation

4.1 Passive microwave applications in cryosphere

Passive microwave brightness temperature measurements from different platforms have been widely used in cryosphere applications (e.g., Abdalati and Steffen 1997; Tedesco et al., 2007; Fettweis et al., 2011). While visible imagery is available for cloud-free regions and only during the daylight time, passive microwave provides continuous imagery of the Earth's surface during day and night. In addition, unlike visible imagery, the passive microwave signal is not significantly affected by different atmospheric components, especially in cold regions (e.g., Qiu et al., 2007). Therefore, continuous passive microwave data theoretically contains information that may be useful to better characterize the surface processes during the day and night for both cloudy and clear sky conditions.

4.1.1 Passive microwave melt signature

A dry snowpack can be considered as a column of air and ice crystals with a dominant volume scattering mechanism. In a wet snowpack, liquid water with higher dielectric constant fills the gaps between the ice crystals and increases the dielectric constant of the snowpack. Surface scattering is directly related to the dielectric constant at the interface between the layers. Therefore, as liquid water increases in the snowpack the surface scattering also increases and begins to dominate over the volume scattering. In addition, as liquid water increases, the emissivity of the snowpack increases and approaches that of a blackbody (Abdalati and Steffen

1995). This property of liquid water in the snowpack has been used to develop different algorithms to classify wet and dry snow (e.g., Abdalati and Steffen 1995, 1997; Ramage and Isacks, 2002).

Over the last two decades, several algorithms have been developed and widely used to map the areal extent of melting snow from passive microwave data. The Cross-Polarized Gradient Ratio (XPGR) introduced by Steffen et al., (1993) and improved by Abdalati and Steffen, (1995, 1997) and diurnal amplitude variation (DAV: Ramage and Isacks, 2002; Tedesco et al., 2007) are two well-known satellite-derived melt classification algorithms. The XPGR is a normalized difference between the 19 GHz horizontal channel and the 37 GHz vertical channel as follows:

$$XPGR = \frac{T_{b,19H} - T_{b,37V}}{T_{b,19H} + T_{b,37V}} \tag{4.1}$$

where the T_b represents the brightness temperature at 19 and 37 GHz, and the indices *V* and *H* represents the vertical and horizontal polarization respectively. The XPGR has been validated using in situ liquid water measurements at the Swiss camp (also called ETH/CU camp) during the 1990 and 1991 field seasons. Abdalati and Steffen, (1995) reported that a sharp increase in the XPGR value (using Special Sensor Microwave/Imager (SSM/I) data) corresponds to the days that mean liquid water content in the top one meter of the snowpack is approximately 0.5% by volume. Using Scanning Multichannel Microwave Radiometer (SMMR) data, Abdalati and Steffen (1997) reported that a sharp increase in the XPGR corresponds to a mean liquid water content of 1% in the top one meter of the snowpack. However, they highlighted that the value of 1% in the top one meter of snowpack is not a robust metric due to the fact that: (1) The XPGR

has been validated at one location and the results might be site specific. (2) The emission depth in a snowpack is highly dependent on liquid water content and for a liquid water content of 2% the emission depth of the 37 GHz and 19 GHz channels are limited to approximately 2 cm and 8 cm respectively (Abdalati and Steffen, 1997). Therefore, averaging liquid water content over the top one meter might underestimate melt extent and melt duration. (3) The threshold of 1% was used to be consistent with the other study conducted by Mote and Anderson (1995). Fettweis et al., (2006, 2011) used a mean daily liquid water content of 1% and 1.1% in the top one meter of snow to compare the satellite-derived melt extent and melt duration with the predicted melt extent and melt duration from the MAR regional climate model. Note that the terms "predicted brightness temperature" and "modeled brightness temperature" have been interchangeably used in this document.

The second algorithm is based on the DAV, which is the difference between ascending and descending passes of the brightness temperatures at 19.35 or 37 GHz. The method is defined based on two thresholds, including 1) a brightness temperature threshold (*A*), 2) a DAV threshold (*B*), which is the difference between the brightness temperatures from ascending and descending passes (e.g., Tedesco 2007). The threshold (*A*) can be obtained from the distribution of measured brightness temperatures over the study area. The histogram of the measured brightness temperatures in a region experiencing melt shows a bimodal distribution. The brightness temperature with the lowest population between the two peaks is considered as the threshold (*A*) (Ramage and Isacks, 2002). Apgar et al., (2007) and Monahan et al., (2010) reported a DAV

threshold value (B) of ±10 K for the data from SSM/I and a value of ±18 K using data from AMSR-E.

4.1.2 Snow depth and snow water equivalent retrieval from passive microwave

In many applications, passive microwave has been directly used in a retrieval algorithm to estimate the snow depth (e.g., Kelly et al 2003; Biancamaria et al., 2008) and snow water equivalent (e.g., Chang et al., 1987) for seasonal snowpacks. While passive microwave retrieval algorithms provide an approximate estimate of snow water equivalent (SWE) and snow depth for shallow snowpack, the well-known saturation effect has limited the application of this algorithm in deep snow. For each passive microwave frequency, there is a certain threshold after which a further increase in snow depth does not affect the observed microwave brightness temperature (Durand et al., 2006). Kelly et al., (2003) reported a saturation depth of 50-100 cm (~100 times of the wavelength) for the 37GHz brightness temperature. Moreover, Durand et al., (2008) reported that a good estimate of SWE needs an accurate estimate of snow grain size, which is very difficult to obtain. Foster et al., (2005) reported that grain size and vegetation cover are two key factors that introduce significant error in SWE retrieval algorithms from passive microwave measurements. Much work has been done to incorporate knowledge of grain size and vegetation canopy into passive microwave retrieval algorithms. Unsatisfactory results from these efforts led some researchers to use data assimilation techniques to improve the SWE estimates.

4.1.3 Passive microwave assimilation

Satellite-based passive microwave measurement is a long continuous data record with approximately 40 years of data. This data set contains valuable information about the snow and ice processes. However, the application of passive microwave data in data assimilation frameworks has been mostly reported in the context of synthetic experiments for seasonal snowpack (e.g., Durand and Margulis 2006; Durand and Margulis 2007, Bateni et al., 2013). In a few studies, the data assimilation technique has been used in small test sites using ground-based radiance observations. For instance, Durand et al., (2008) used snowpit data and ground-based radiometer measurements from the NASA Cold Land Processes Field Experiment (CLPX) to quantify uncertainty of radiance assimilation. Ally et al., (2011) used ground-based passive microwave data in a data assimilation framework to improve the SWE estimate in the NASA CLPX site. Bateni et al., 2015 used a data assimilation framework to characterize SWE and the underlying soil freeze-thaw state in the CLPX site. Recently, Li et al., (2015a, 2015b) used AMSR-E data to improve the SWE estimate in the upper part of the Kern River Basin, Sierra Nevada. The main reasons for the limited application of passive microwave in data assimilation frameworks are due to 1) the fact that the spatial resolution of the passive microwave measurements is very coarse which makes it very difficult to relate point scale results to satellite footprint scale; 2) difficulties related to estimation of snow states especially snow grain size and their representativeness; 3) the well-known saturation effect of passive microwave signal, and 4) the lack of accuracy of predicted passive microwave brightness temperature relative to measured

brightness temperature. Some studies have tried to address these issues; however, more effort is needed to be able to properly implement data assimilation techniques over a large-scale domain using satellite-derived passive microwave measurements. In particular, characterizing error and uncertainty between the measured and modeled brightness temperatures requires an extensive effort.

4.2 Motivation

Passive microwaves emitted from snow covered surfaces contain information about snow grain size, snow phase, snowpack stratigraphy, and snow layer temperature. But the information content of passive microwave data remains under-utilized due to an indirect and implicit relation between passive microwave and snow states and fluxes. Assimilation is a key step to exploit the information content of passive microwave data. In passive microwave radiance assimilation, a radiative transfer model (e.g., MEMLS: see Section 4.3.2.1) must be used to predict satellite-derived brightness temperatures. The predicted values contain errors; therefore, the first necessary step is to characterize the error and uncertainties associated with predicted values prior to using them in a data assimilation framework. Understanding and characterizing the errors are the main motivations for this chapter.

Many studies tried to characterize the error and uncertainty of the microwave brightness temperature of seasonal snowpack. Tedesco and Kim (2006) conducted an inter-comparison between four different electromagnetic models and highlighted that there is no superior model and all models have some advantages and disadvantages. Tedesco and Kim (2006) reported that

MEMLS can reproduce the brightness temperature at 37 GHz vertical polarization with an average error of 15% to 20%. Tedesco et al., (2006) used the dense media radiative transfer theory (DMRT) and snowpit data and ground-based radiometer data from the NASA CLPX to compare the predicted and measured brightness temperatures. They were able to reproduce brightness temperatures at 37 GHz channels with an error of ~20 K. Durand et al., (2008) used snowpit data and ground-based radiometer measurements from the NASA CLPX and reported a difference of 3.4 K and 9.3 K between the predicted and measured brightness temperatures at 37 GHz horizontal and vertical polarization respectively. For a comprehensive study, the reader is referred to the following references (e.g., Tedesco et al., 2006; Tedesco and Kim 2006; Durand and Margulis 2007, Durand et al., 2008, Brucker et al., 2011; Picard et al., 2013; Roy et al., 2015). However, to the best of my knowledge, there is no study to characterize the error and uncertainty associated with predicted and measured passive microwave brightness temperatures over the GrIS. Here, it has been hypothesized that the sources of error and uncertainty in passive microwave brightness temperatures for both seasonal snowpack and ice sheet are similar while the underlying media is different.

Durand et al., (2008) reported three sources of uncertainty in predicted brightness temperature using the MEMLS radiative transfer model as follows: 1) uncertainty associated with MEMLS physics, 2) uncertainty associated with lack of vertical discretization of the snowpack, 3) uncertainty in input variables from the land surface model. With regard to the first source of uncertainty, it is worth noting that, while the MEMLS physics is not perfect, it is one of

the most widely applied models to predict microwave emission and validation of MEMLS has been reported in the literature (e.g., Wiesmann and Mätzler 1998; Wiesmann and Mätzler 1999). Furthermore, the discussion about MEMLS physics is beyond the scope of this dissertation. However, the effect of grain size parameterization on predicted brightness temperature has been investigated. With regard to the second source of uncertainty, it is expected that the use of CROCUS can help resolve this issue because CROCUS has the ability to finely discretize the snowpack in the vertical direction. A detailed discussion has been given in Section 4.3.2.3 (CROCUS modification). With regard to the third source of uncertainty, Durand et al., (2008) used snowpit data and ground-based measurements and reported that the predicted brightness temperature is very sensitive to the presence of ice layers, error in exponential correlation length, and error in density. Considering the above discussion, the focus of this chapter would be on the third source of uncertainty explained above. The goal is to understand the effects of grain size parameterization, uncertain input variables, and sub-grid heterogeneity on predicted passive microwave brightness temperature in the context of simulating microwave emission from the GrIS.

4.3 Data and model

4.3.1 Data

4.3.1.1 Snowpack characteristic

Availability of real snow profiles over the GrIS is limited to the location of ice core projects

or field campaigns which are very sparse in time and space. On the other hand, snow/ice models and regional climate models (RCMs) provide spatially and temporarily distributed estimates of snow profile which can be used to predict brightness temperature over the GrIS using a radiative transfer model.

The snow profile from a large scale RCM (i.e., MAR) contains error and uncertainties. It was found out that the snow profile in some pixels has an unusual structure which can be due to an artifact in the model. For instance, in MAR version 2 the thickness and density of the surface layer in some pixels are about 40 cm and 300 kg/m^3 respectively while the thickness and density of the next layer under this thick layer are about 1 cm and 150 kg/m^3 respectively. In addition, MAR uses large grain size parameters to characterize the solid ice which might negatively affect the predicted brightness temperature. These issues have been discussed in the following sections.

Model spin-up, i.e. running the snow/ice model until it reaches a state of statistical equilibrium under the applied forcing, could mitigate some errors and uncertainties in the initial snow profile. In this study, a one-year spin-up was performed to bring the snow profile to the equilibrium state and correct the snow layer properties. An inspection of snow profile after the spin-up period shows that CROCUS can effectively correct the snow profile from MAR. However, very large grain size parameters associated with solid ice at the bottom of the profile in the ablation and percolation zones remain unchanged. The sensitivity of predicted brightness temperature to this large grain size has been explained in (Section 4.4.4 Issues related to MAR snow profiles). Given the initial snow profile from the spin-up simulation, CROCUS was run

forward in time to simulate the time evolution of snow profile for each grid cell over the GrIS (Fig 4.1). CROCUS provides estimates of the snow states, including layer thickness, grain size, temperature, density, and liquid water content at each time step.

The GrIS consists of three mass balance zones with different snow/ice profiles. In the ablation zone, a typical snow profile is similar to a seasonal snowpack, but over solid ice. Note that during summer it might just be bare ice. In the percolation zone, accumulation exceeds ablation; therefore, a typical snowpack consists of snow layers from several snow seasons. Snow profiles in the percolation zone are highly heterogeneous (e.g., Brandt et al., 2009; Harper et al., 2012) and consist of ice lenses, ice pipes, and ice layers. The shape, depth, and density of the ice features depend on the structure of the snowpack, melt intensity and melt duration (e.g., Pena et al., 2015). In the percolation zone, the snowpack heterogeneity introduces considerable uncertainty into the estimates of brightness temperature. Moving toward the dry snow zone, the heterogeneity of snow profiles reduces. However, extreme snowmelt events (e.g. Nghiem et al., 2012; Hall et al., 2013) which can extend over the dry snow zone have introduced layers of ice (i.e. heterogeneity) to the snow profiles in the dry snow zone (Pena et al., 2015).

4.3.1.2 Measured passive microwave

In this study, passive microwave brightness temperatures were obtained from the AMSR-E instrument on the NASA-EOS Aqua satellite. The AMSR-E sensor provides horizontally and vertically polarized passive microwave data in 12 channels, six frequencies with a spatial resolution of 5.4km (89GHz) to 56km (6.9 GHz). The data has already been projected into the

North Pole Lambert Azimuthal Equal Area grid which is available online at ftp://sidads.colorado.edu/pub/DATASETS/nsidc0301_amsre_ease_grid_tbs/north/. For application over the GrIS, the data was resampled to the MAR/CROCUS grid (see Fig 4.1).

4.3.2 Passive microwave radiative transfer model

Predictions of brightness temperature using snow properties are required in order to be able to compare with satellite-measured brightness temperature. Electromagnetic wave theory and the radiative transfer theory are two commonly used methods to predict the brightness temperature. For a comprehensive review on this topic, the reader is referred to Bucker et al., (2011); and Löwe and Picard (2015).

4.3.2.1 Microwave Emission Model of Layered Snowpack (MEMLS)

In this study, we chose to use radiative transfer theory by implementing MEMLS (Wiesmann and Mätzler 1999). MEMLS treats a snowpack as a stack of horizontal parallel layers. The layers are introduced to the model with properties like thickness, exponential correlation length (related to grain size), density, liquid water content, and temperature. MEMLS employs the sandwich model to take into account both the internal scattering and reflections at the interfaces. MEMLS uses an empirical relationship or the improved Born approximation to determine the scattering coefficient. The scattering coefficient depends on the correlation length, density, and frequency. The absorption coefficient depends on density, temperature, and frequency (Wiesmann and Matzler, 1998). While the real part of the dry snow effective

permittivity depends on density (Matzler 1996) a fixed value of 3.15 has been used for the real part of ice permittivity (Tedesco and Kim 2006). MEMLS uses the method by Matzler (1998) for the imaginary part of ice permittivity. Note that by adding the improved Born approximation to MEMLS, it became a complete physically based model (Matzler and Wiesmann, 1999).

A detailed evaluation of MEMLS performance for the different type of snowpack has been reported in the literature (e.g. Wiesmann and Matzler, 1999; Matzler and Wiesmann, 1999, Bucker et al., 2011).

4.3.2.2 Snow input parameters

MEMLS needs physical properties of the snowpack to predict brightness temperature. CROCUS provides all these input variables except the exponential correlation length, which is a function of grain size parameters. Different land surface models provide different grain size parameters. While some models (e.g., Jordan grain size model 1991; Flanner and Zender grain size model, 2006) attempt to estimate the grain size diameter (D_g) other models (CROCUS, SNOWPACK (Lehning et al., 2002)) define the grain size by three parameters such as dendricity, sphericity, and grain size. Brun et al., (1989) proposed an empirical equation to compute an optical equivalent diameter (D_o) using the dendricity, sphericity, and grain size. A complete discussion about the relation between the grain size and the exponential correlation length has been reported in Mätzler (2002). This relationship is given by:

$$P_{ex} = \alpha D_i$$
$$\alpha = \frac{2}{3}\beta(1-\nu) \qquad (4.2)$$

where D_i is the grain size or optical grain diameter and β is an empirical coefficient suggested to be 0.75 and ν is the volumetric fraction of ice. Mätzler (2002) suggested an α value of 0.4 and 0.3 for dendritic and non-dendritic snow respectively; when the coupled CROCUS-MEMLS is used. For the coupled Sntherm-MEMLS model, Mätzler (2002) suggested a constant α value of 0.16. Huang et al., (2012) studied the impact of different grain size models on estimates of brightness temperature. Huang et al., (2012) suggested a constant value of 0.11 for α using the grain size of the SNOWPACK model. For the grain size model of Flanner and Zender (2006), Huang et al., (2012) suggested an α value of 0.2 and for the Jordan grain size model (Jordan 1991) they suggested an α value of 0.11. Brucker et al., (2011) compared the observed and modeled brightness temperature to adjust α and found that the best fit with a β value of 0.63, which results in an α range from 0.25 to 0.4. Following Mätzler (2002) and Brucker et al., (2011), three different α values of 0.2, 0.3, and 0.4 were used to relate the optical grain diameter with the exponential correlation length.

In this study, brightness temperatures were predicted using MEMLS version 3 available at (http://www.iapmw.unibe.ch/research/projects/snowtools/memls.html). MEMLS needs snow layer temperature (K), volumetric liquid water content, density (kg/m^3), thickness (cm), salinity (part per thousand), and exponential correlation length (mm) to predict brightness temperature. Besides the snow parameters, MEMLS needs other input parameters to complete the simulation. The input parameters include 1) the desired frequency, in this study our focus is on V-pol brightness temperature at 36.5 GHz, which proved to be sensitive to liquid water and has been

widely used in different retrieval algorithms. 2) The incident angle, AMSR-E has an incident angle of 55º degree, therefore, the same incident angle was used as an input to MEMLS. 3) Snow-ground reflectivity, MEMLS computes brightness temperature using both the snowpack parameters and the snow-ground reflectivity. In seasonal snow, the empirical model introduced by Wegmuller and Matzler (1999) can be used to provide underlying ground parameters. In this application, approximately top 10 meters of the ice sheet have been simulated. The snow/ice layer under the simulated layers was used as a bottom boundary condition; hence, there is no need to use the snow-ground interface parameters. 4) The sky downwelling brightness temperature (T_{sky}) is also needed by MEMLS. The lowest possible value is 2.7 K which also means a situation without any atmospheric influence. In general the atmospheric influence on T_{sky} is higher on high frequencies than low frequencies. In many applications in cold regions, due to the lack of water vapor and absence of clouds, the effect of the atmosphere is negligible. A sensitivity analysis on sky brightness temperature (i.e., increasing T_{sky} from 2.7 K to 10 K) shows that by increasing T_{sky}, predicted brightness temperatures slightly increase, however, the differences between brightness temperatures from different sensitivity experiments are negligible. This result is in agreement with the results reported by Durand et al., (2008). In this study, following Durand et al., (2008), the lowest possible value of 2.7 K was used for simplicity. 5) The ground temperature needs to be provided, here, the bottom layer temperature was used as the ground temperature. 6) Finally, the type of scattering coefficients must be determined. As explained above, two scattering options are available, one is based on an empirical equation and

the other is the physically based improved Born approximation. Both scattering coefficients have validity and both suffer from uncertainties. In the improved Born approximation, the correlation length describes the snow structure. For a snowpack with this property, the improved Born approximation is probably superior to the empirical equation. For instance, refrozen snow after having been wet is a good example. On the other hand, in some cases, the correlation function may not be exponential, especially for relatively fresh snow (personal communication with Christian Matzler). However, we chose to use the improved Born approximation to predict the brightness temperature since it is a physically based model and better represents the GrIS especially in the ablation and percolation zones with frequent melt and refreeze cycles.

4.3.2.3 CROCUS modification

As stated in Chapter 2, the CROCUS bottom boundary condition was modified to add(remove) snow/ice layer to(from) the bottom of the snowpack, to keep the thickness of the snowpack about 10 meters at all times.

4.4 Results and discussion

In this section, pixel scale and distributed predicted brightness temperatures from MEMLS were compared with satellite-measured brightness temperatures. The differences between the predicted and measured brightness temperature come from different sources including 1) error and uncertainty from satellite sensor, data processing, re-sampling of satellite footprint to nominal passive microwave resolution of 25 km, 2) error related to radiative transfer models, 3) lack of vertical discretization of snowpack, 4) error in CROCUS physics, 5) error in snow states

from CROCUS, and 6) sub-grid heterogeneity. In this section, the effects of snow grain parameterization, snow density, sub-grid heterogeneity and uncertainty in snow profile from MAR have been investigated. It was hypothesized that the sub-grid heterogeneity plays an important role in the differences between the predicted and measured brightness temperature. While there is no high-resolution passive microwave brightness temperature data to characterize the error, using other high-resolution datasets may help to highlight the effect of sub-grid heterogeneity.

4.4.1 Sensitivity analysis on exponential correlation length

4.4.1.1 Pixel scale results

4.4.1.1.1 Simulation results for a sample pixel in the ablation zone

The snowpack in the ablation zone can be characterized as seasonal snow over solid ice. In the ablation zone, especially in the ice sheet margin, a seasonal snow cover melts quickly during the melt season and leaves the bare ice exposed. Figure 4.2a shows the passive microwave brightness temperature at 36.5 GHz vertical polarization from AMSR-E and the predicted brightness temperature using CROCUS-MEMLS for α values of 0.2, 0.3, and 0.4. As can be seen, from Figure 4.2a, the measured brightness temperature at 37 GHz V-pol is significantly different from the predicted brightness temperature. During the melt period (i.e., May-September) the measured brightness temperature shows a significant diurnal cycle, presumably due to the presence of liquid water in the snowpack. The predicted brightness temperature for the same

period can be divided into two sub-periods, (1) the period in which snow exists over the solid ice; during this period, brightness temperature shows diurnal cycle due to melt and refreeze processes, (2) the period where bare ice is exposed and melting occurs from the bare ice. The exposed bare ice decreases the scattering and as a result, brightness temperature increases. While the AMSR-E signal shows diurnal cycles during the second period, the predicted brightness temperature is almost constant about 273 K. Differences between predicted brightness temperatures and satellite-derived brightness temperatures may be due to sub-grid heterogeneity. The measured brightness temperature is an integrated value over the 25 km grid cell with different snow and ice features (i.e., snow gullies, ice hummocks, meltwater ponds, impurities) while the modeled brightness temperature is from a single ice profile.

From mid-September 2009, snow starts accumulating over the bare ice and the predicted brightness temperature gradually decreases and moves toward the measured value due to an increase in snow depth over the solid ice. As can be seen, in Figure 4.2a measured brightness temperatures remain relatively constant during the accumulation season. Possible reasons could be low precipitation rate, and blowing snow due to katabatic winds. As shown in Figure 4.2a an α value of 0.4 better represents the grain size parameterization during the accumulation season.

Figure 4.2b and Figure 4.2c show the evolution of snow layer density and snow layer exponential correlation length at the JAR1 pixel (i.e., pixel that is co-located with the JAR1 station) for year 2009 and 2010. As can be seen in Figure 4.2b the simulated snowpack melts within several weeks during the melt season and bare ice is exposed. The bare ice is less

reflective than snow, therefore, the ice surface absorbs more energy and generates more meltwater which further reduces the albedo and creates a positive albedo feedback. This mechanism is responsible for significant melt in the ice sheet margin as shown in Figure 4.2b.

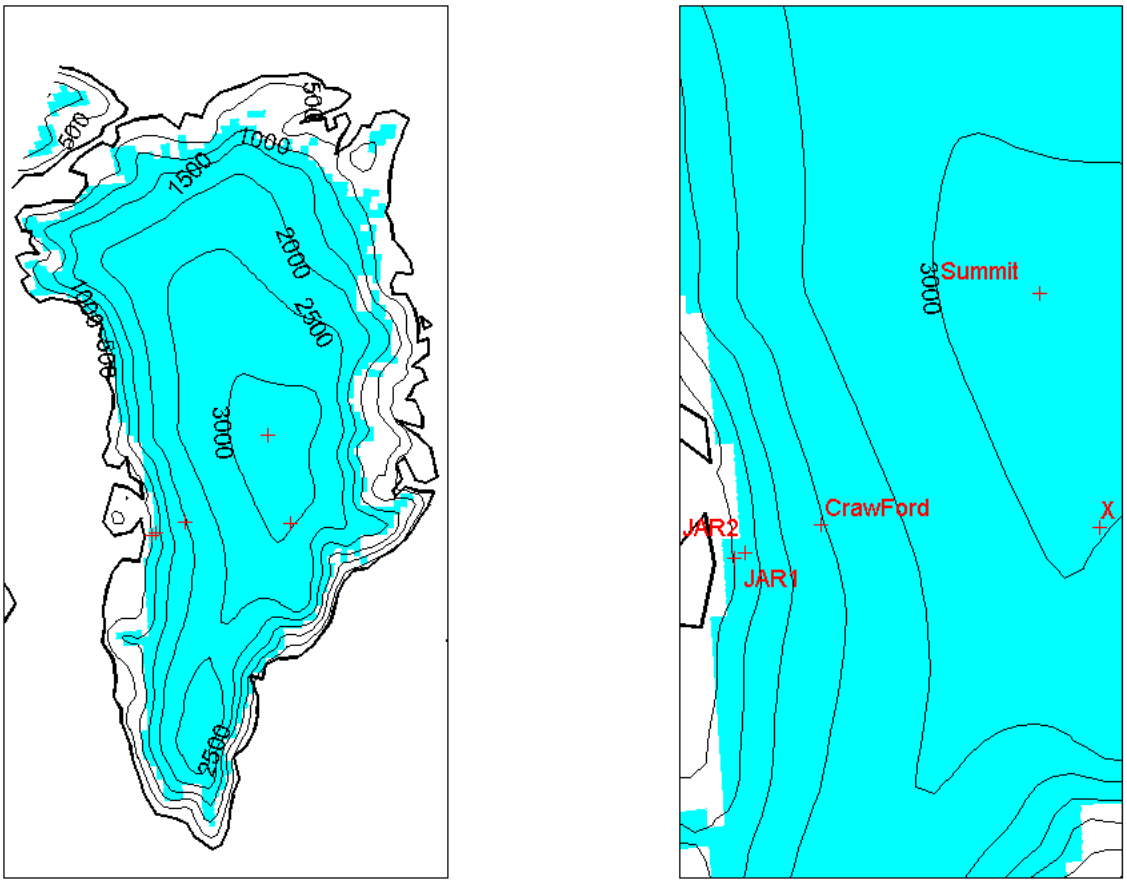

Figure 4.1 a) The GrIS mask, b) location of JAR2, JAR1, Crawford, X, and Summit stations

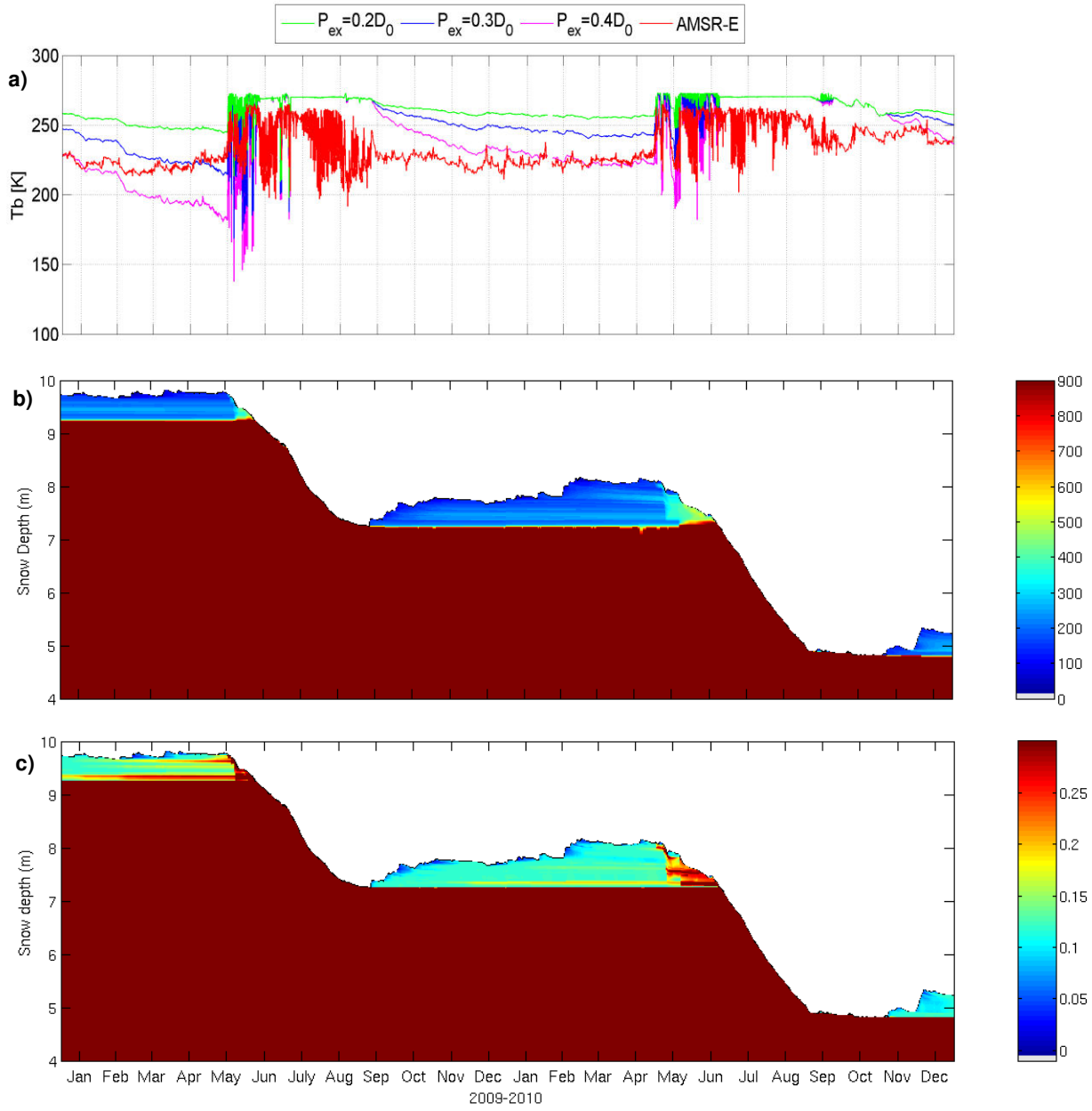

Figure 4.2 (a) time series of the brightness temperature at 36.5 GHz vertical polarization from AMSR-E and CROCUS-MEMLS for 2009 and 2010 at the JAR1 pixel, the red line shows the measured brightness temperature from AMSR-E sensor, the green, blue, and magenta lines show the predicted brightness temperature from CROCUS-MEMLS using an α value of 0.2, 0.3, and 0.4 respectively, (b) evolution of the snow/ice density in kg/m^3, solid ice shown with dark red color, (c) evolution of the exponential correlation length in mm.

4.4.1.1.2 Simulation results for a sample pixel in the percolation zone

In the percolation zone, accumulation exceeds ablation and snow layers accumulate on top of the older snowpack from previous seasons. During the melting season, periodic melt-refreeze cycles create ice layers, ice lenses, and ice pipes with different shapes and sizes which make the snowpack highly heterogeneous. The snowpack heterogeneity is different from location to location. For instance, in the low elevations, the snowpack is more heterogeneous than the high elevation since melting occurs more frequently and with higher intensity. The snow layers that survived from previous melting season create a denser layer called firn. Accumulation of these firn layers creates a stratified snowpack with vertical and horizontal heterogeneity. The satellite sensor detects both the horizontal and vertical heterogeneity and provides an integrated brightness temperature over the footprint of the passive microwave sensor. Note that passive microwave penetration depth may vary from a few centimeters to hundreds of meters depending on snow wetness, density and microwave frequency [Mätzler 2006]. This complex and heterogeneous structure might introduce significant uncertainty in modeled brightness temperatures as heterogeneity over the 25 km by 25 km grid cell must be represented by means of a single snow profile.

Figure 4.3a shows the time series of the predicted and measured brightness temperature for the pixel encompassing the Crawford station (see Figure 4.1). As can be seen in Figure 4.3a, the measured and predicted brightness temperatures are in general agreement from January 2009 to

June 2009 and from October 2009 to June 2010 using an α value of 0.2. In the melt season, the snowpack experiences melt metamorphism. Liquid water from the melting percolates into the snowpack and freezes at certain depths where the temperature is subfreezing. During the freezing process, liquid water binds the existing grains together and creates larger grains. The freezing process also releases latent heat that can accelerate the constructive metamorphism as an effective grain growth mechanism. These mechanisms form a denser snow layer with a higher exponential correlation length as shown in Figure 4.3b and Figure 4.3c. Figure 4.3a shows that the measured brightness temperature sharply drops in July 2009 and in late August 2010. This is more likely due to refreezing liquid water content within the snowpack and exposure of dense snow layers (i.e., ice lenses). This is unexpected since the 36.5 GHz vertical polarization is less sensitive to ice lenses.

From September 2009 to May 2010, which corresponds to the accumulation season, the measured brightness temperature gradually increases. This anomalous behavior is in contrast with the snow scattering property of microwave radiation. The classical pattern assumed that the brightness temperature has an inverse relationship with snow depth and frequencies. It is worth noting that this classical property of the snowpack has been widely used in SWE retrieval algorithms (e.g., Chang et al. 1987). Similar anomalous observations have been reported by Rosenfeld and Grody (2000). They reported (1) a positive correlation between the brightness temperature and snow depth in the deep Alpine snow, and (2) an increase in the brightness temperature in late winter in some locations in Siberia and northern Europe. They suggested that

possible reasons for this anomaly could be due to the snow aging and reduction in snow depth due to the densification. The modeled brightness temperature from September 2009 to May 2010 shows a different pattern; it gradually decreases due to the accumulation of new snow on top of the old and dense snow layers and then gradually increases after it reaches a minimum in December. Fresh snow with small grain size and low density significantly scatters the microwave signals and reduces the brightness temperature. An increase in the predicted brightness temperature after reaching the minimum value is more likely due to the snowpack densification which is similar to the effect of decreasing snow depth (Rosenfeld and Grody 2000) and aging of the snowpack while snowfall events temporarily interrupt this increasing trend.

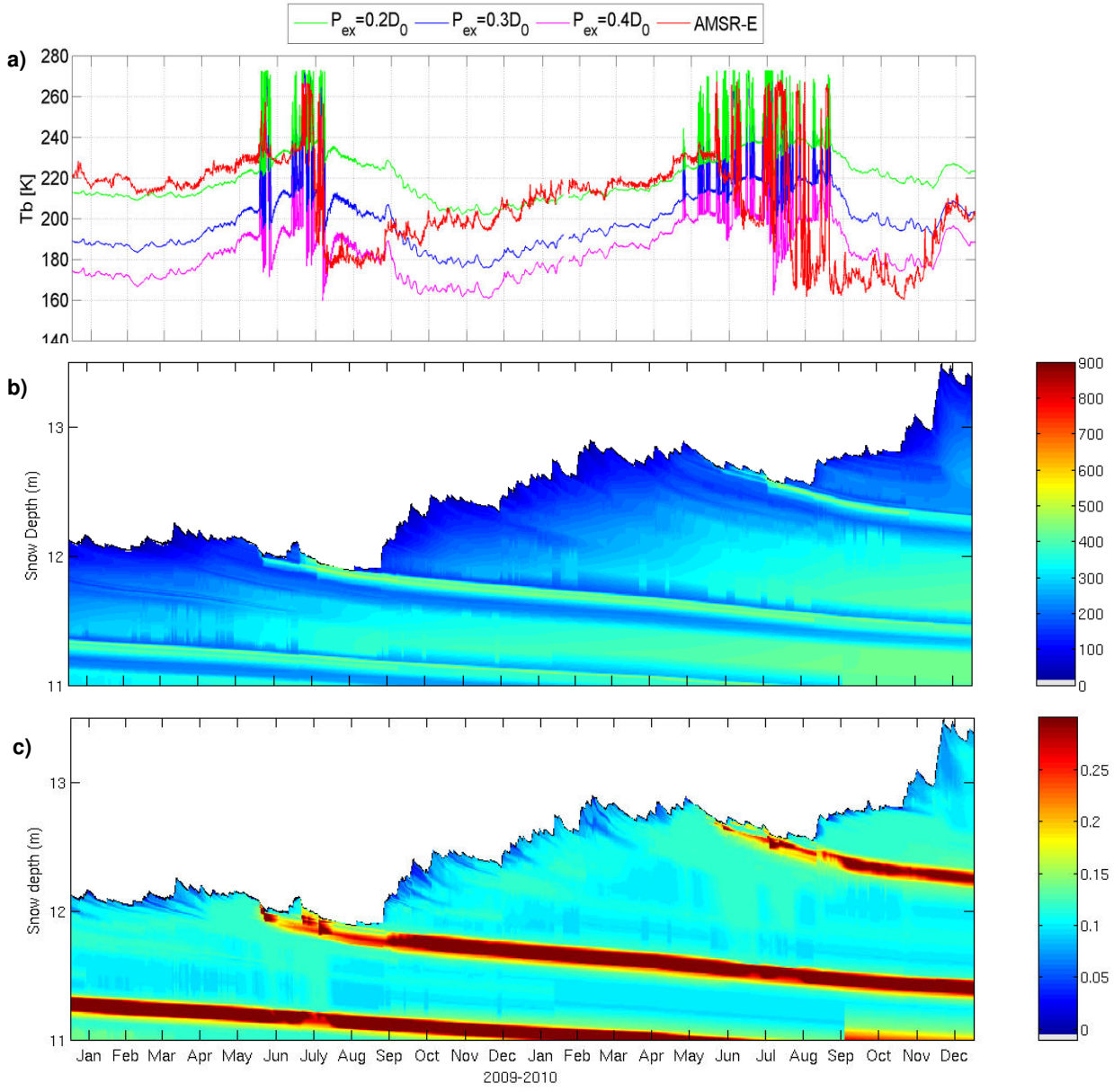

Figure 4.3 the same as Figure 4.2 but for the Crawford pixel

4.4.1.1.3 Simulation results for a sample pixel in the dry snow zone

Over the dry snow zone, sub-grid heterogeneity is less than the ablation and percolation zones and melting typically does not occur or only occurs in a few days period during extreme melt years such as 2009 and 2010. As a result, the vertical profile would also be less heterogeneous and characterizing the brightness temperature at the measured passive microwave scale (i.e. 25 km) using representative snow profile would involve less uncertainty. Figure 4.4a shows the time series of measured and predicted brightness temperature over a sample pixel in the dry snow zone (the location of the pixel has been marked with X in Figure 4.1b). As can be seen, the predicted brightness temperature using an α value of 0.2 is in agreement with the measured brightness temperature and the predicted value closely follows the measured brightness temperature. Both the predicted and measured brightness temperatures gradually decrease during the accumulation season to reach a minimum value and then gradually increase. Rosenfeld and Grody (2000) reported that brightness temperature minimum in the middle of accumulation season is typical in very cold regions with long winter period and perennial snow. For instance, in these regions, brightness temperatures at 36.5 GHz vertical polarization reach a minimum around January and then gradually increase after that. This phenomenon is more likely due to two competing processes: 1) the growth of ice crystals within the snowpack decreases single scattering albedo and makes the snowpack more transparent to passive microwave, which leads to an increase in brightness temperature (i.e., this is so-called aging), and 2) accumulation

of fresh snow in the beginning of accumulation season, which increases the scattering of the microwave signals and reduces the brightness temperature.

The predicted brightness temperature shows a similar pattern as the measured brightness temperature and decreases from July 2009 to early December 2009 and increases from December 2009 to May 2010. The decrease in brightness temperature is associated with the accumulation of fresh snow and the increase in brightness temperature is more likely due to the aging of the snowpack. Figure 4.4b and Figure 4.4c show the time evolution of the snowpack density and the snowpack exponential correlation length over the two-year period. During the melt season due to the increase in temperature and few melt events, the snowpack experiences different metamorphism mechanisms. While the metamorphism processes significantly influence the grain size and the exponential correlation length (Figure 4.4c), these mechanisms do not considerably affect the density of the snowpack (Figure 4.4b). The difference between the density profiles (Figure 4.3b and Figure 4.4b) can be a potential reason for the difference between the brightness temperatures after the melt period in the percolation and the dry snow zones.

In this section, time series of the predicted brightness temperatures for three pixels (JAR1, Crawford, pixel X) in the different mass balance zones (Figure 4.1) were compared with satellite-derived brightness temperatures from AMSR-E. These pixels show general structures of snow and ice profiles in the different mass balance zones. It was also hypothesized how these structures potentially affect the predicted brightness temperatures. However, there is significant uncertainty in the predicted brightness temperatures and it is almost impossible to generalize the

results obtained from the sample pixel in each mass balance zone to all pixels in that zone.

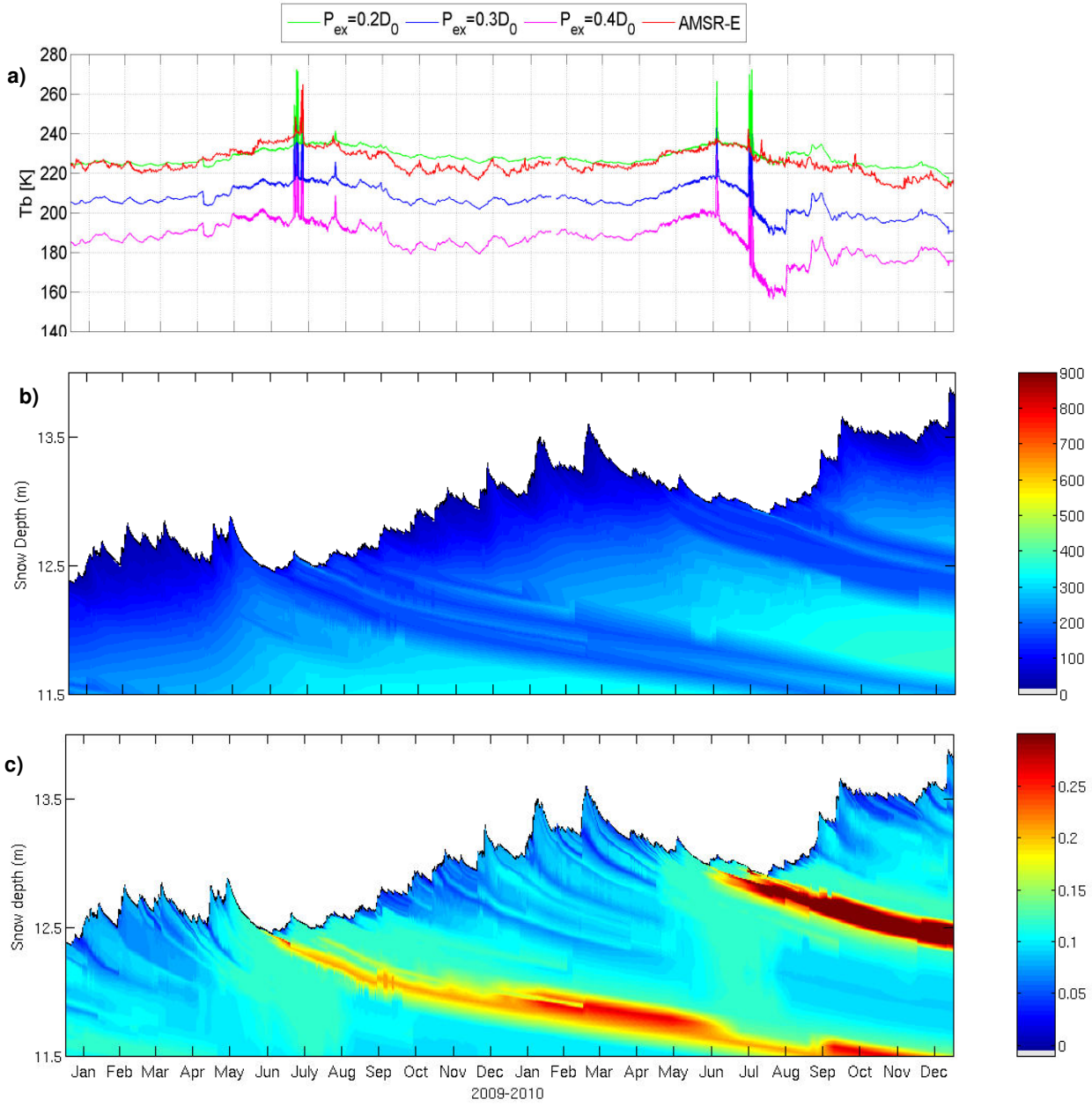

Figure 4.4 the same as Figure 4.2 but for the pixel X at the dry snow zone

4.4.1.2 Distributed results

Snow grain size plays a key role in many radiative transfer models. In MEMLS, the exponential correlation length is used to describe the snow grain size. A commonly used empirical equation utilizes a proportionality constant (i.e., α) to relate the grain size or optical grain diameter to the exponential correlation length. A more physically based model (Eq. 4.2) uses a volumetric fraction of ice to compute the exponential correlation length.

In many studies, the α value has been determined by minimizing the error between the predicted and the measured brightness temperature. This can be achieved by tuning the grain size model parameters (e.g., Durand et al., 2008) or by tuning the α value (e.g., Brucker et al., 2011). An overview of the previous studies shows that these methods have been generally used (1) in a small site equipped with a ground-based radiometer (Durand and Margulis 2008), (2) for the seasonal snowpack, and (3) during the winter when the snowpack is dry (e.g., Durand et al., 2008; Durand and Margulis 2008; Ally et al., 2011, Rees et al., 2010). It can be argued that over the GrIS it would be very difficult if not impossible to apply the same methodologies due to the following reasons: (1) A satellite-based passive microwave measurement is an aggregated brightness temperature over the 25 km by 25 km grid cell while the footprint of ground-based observation is more closely related to snow profiles from snowpits, hence, it is less likely to achieve the same accuracy which has been reported using ground-based measurements. (2) Wet snow acts like a black body, therefore in almost all studies passive microwave has been utilized

during the dry period to estimate SWE or snow depth; however, in order to estimate the surface mass fluxes over the GrIS, passive microwave must be used during both the dry and melt period. While during the melt period the modeled brightness temperature shows a constant value of ~273K, the measured brightness temperature is much smaller (i.e. ~260 K). One possible reason could be sub-grid heterogeneity. This large bias between the modeled and measured values is another issue that needs to be considered. (3) Results from different studies show that model parameters (e.g., α, β) are site specific and the parameters obtained from one site cannot necessarily be applied to other sites. (4) The snow/ice profiles over the GrIS are very heterogeneous and complex. The profiles are influenced by many meteorological and geographical parameters among other including temperature, wind speed, precipitation intensity, precipitation type, melt intensity, melt period, latitude, and elevation (e.g., Kokhanovsky, 2011). While snow profiles over the GrIS can be classified into three general categories based on the GrIS mass balance zones, snow profiles within the same mass balance zone, but from different elevations, are significantly different. Therefore, based on these reasons, it would be very difficult to find an optimum α value even for the pixels in the same mass balance zone.

In this chapter, MEMLS was run for three different α values of 0.2, 0.3, and 0.4 and the results were compared with the satellite-derived brightness temperature. This experiment would help to assess the possibility of using a constant α value over the different mass balance zones. Then a density dependent α value (Eq. 4.2) was implemented to further investigate the effect of the density dependent α on the predicted brightness temperature.

As shown in Figure 4.2a over the ablation zone where the bare ice is exposed during the summer, snow grain parameterization (i.e., α) does not play any role in the observed discrepancy between the predicted and measured brightness temperature. Error and uncertainty from input variables and sub-grid heterogeneity are likely responsible for the observed discrepancy. Table 4.1 shows the spatial mean RMSE and bias using different α values for the different mass balance zones. Over the ablation zone, using an α value of 0.4 leads to the lower bias and RMSE in comparison with other α values for the both 2009 and 2010. However, the large RMSEs indicate that the predicted brightness temperature contains significant error and uncertainty which makes the use of this data in a retrieval algorithm or a data assimilation framework disputable. Note that the RMSE and bias presented in Table 4.2 are an integrated value and represent all sources of error and uncertainty.

From Table 4.1, in the percolation zone close to the ice sheet margin using an α value of 0.4, the predicted brightness temperature better matches the measured value. Nevertheless, moving from the margin toward the ice sheet interior, a smaller α value provides a better match between the predicted and measured brightness temperature. In addition, obtaining an optimum α value is also subject to the inter-annual variability of the snowpack properties. For instance, in the percolation zone for year 2009 an α value of 0.3 shows a bias of 5 K while for year 2010 using an α value of 0.4 provides a low bias of -5 K (see Table 4.1). However, the spatial mean RMSE of the predicted brightness temperature in this zone is about 27 K for both α values of 0.3 and 0.4. As shown in Figure 4.3b-c, during the melt period, snowpack experiences significant

changes in grain size, density, and snow stratigraphy. These changes contribute to significant differences between the predicted and measured brightness temperature after the melt period and consequently lead to a large RMSE observed in this zone. It is clear that this uncertain data cannot be used in a data assimilation system. An inspection of the time series of brightness temperature for several pixels in the percolation zone using α values of 0.2, 0.3, and 0.4 shows that the predicted brightness temperature is very sensitive to the exponential correlation length. The sensitivity of the predicted brightness temperature to the layer exponential correlation length is about -0.4 K per percentage increase in the exponential correlation length.

Table 4.1 shows that over the dry snow zone, an α value of 0.2 provides better results. Similar to the percolation zone an inspection of the time series of brightness temperature for several pixels using different α values revealed that the sensitivity of the predicted brightness temperature to the layer exponential correlation length in the snow dry zone is about -0.4 K per percentage increase in the exponential correlation length. In this zone, while, the spatial mean bias of the predicted brightness temperature shows a low value of -3 K, the spatial mean RMSE is 24 K and 15 K for 2009 and 2010 respectively.

Figure 4.5 and Figure 4.6 show the spatial RMSE and bias for different α values for year 2009 and 2010. It is clear that using a smaller α value is more suitable for the GrIS interior (i.e. the dry zone) where the grain size can be characterized with a smaller exponential correlation length. Comparing the RMSE and bias maps from year 2009 and 2010 illustrates the inter-annual variability of the predicted and measured brightness temperature. For instance, a comparison

between Figure 4.5a and Figure 4.5d shows that while an α value of 0.2 leads to a very small RMSE in the interior area of the GrIS in 2010; using the same α value leads to a large RMSE in the same area in 2009. A further comparison between the RMSE and bias maps of the different α values for the same year shows the spatial variability of the predicted brightness temperature due to the change in exponential correlation length. For instance, a comparison between Figures 4.6d, e, and f shows that a smaller α value leads to a lower bias in the GrIS interior while a larger α value leads to a smaller bias in the GrIS margin. However, there is no distinct boundary between these regions and α values need to be adjusted based on snow properties and geographical information (i.e. latitude and elevation) to reduce the error due to imperfect α value while the error from other sources could be a reason for the differences between the predicted and measured brightness temperatures.

Table 4.1 The spatial mean RMSE and bias of 36.5 GHz vertical polarization in [K] using different α values over the different mass balance zones for years 2009 and 2010

		2009			2010		
		α=0.2	α=0.3	α=0.4	α=0.2	α=0.3	α=0.4
RMSE	Ablation zone	40	35	34	36	29	27
	Percolation zone	33	27	27	35	27	27
	Dry zone	24	34	46	15	23	37
Bias	Ablation zone	36	24	10	32	21	7
	Percolation zone	20	5	-10	27	11	-5
	Dry zone	-17	-31	-44	-3	-19	-35

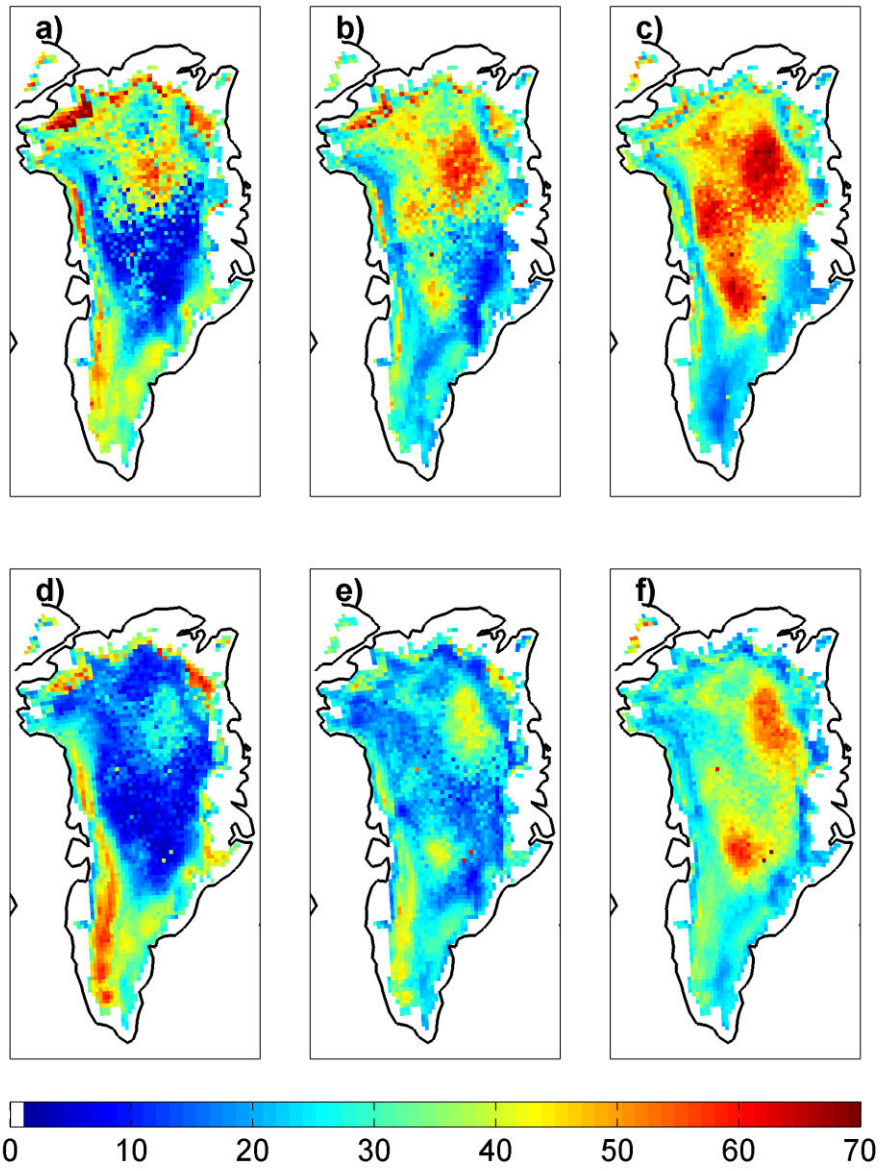

Figure 4.5 The RMSE of the predicted brightness temperatures at 36.5 GHz vertical polarization relative to the measured values in [K] using different α values for years 2009 and 2010, (a) the RMSE for α =0.2, (b) the RMSE for α =0.3, (c) the RMSE for α =0.4, the second row is the same as the first row but for year 2010.

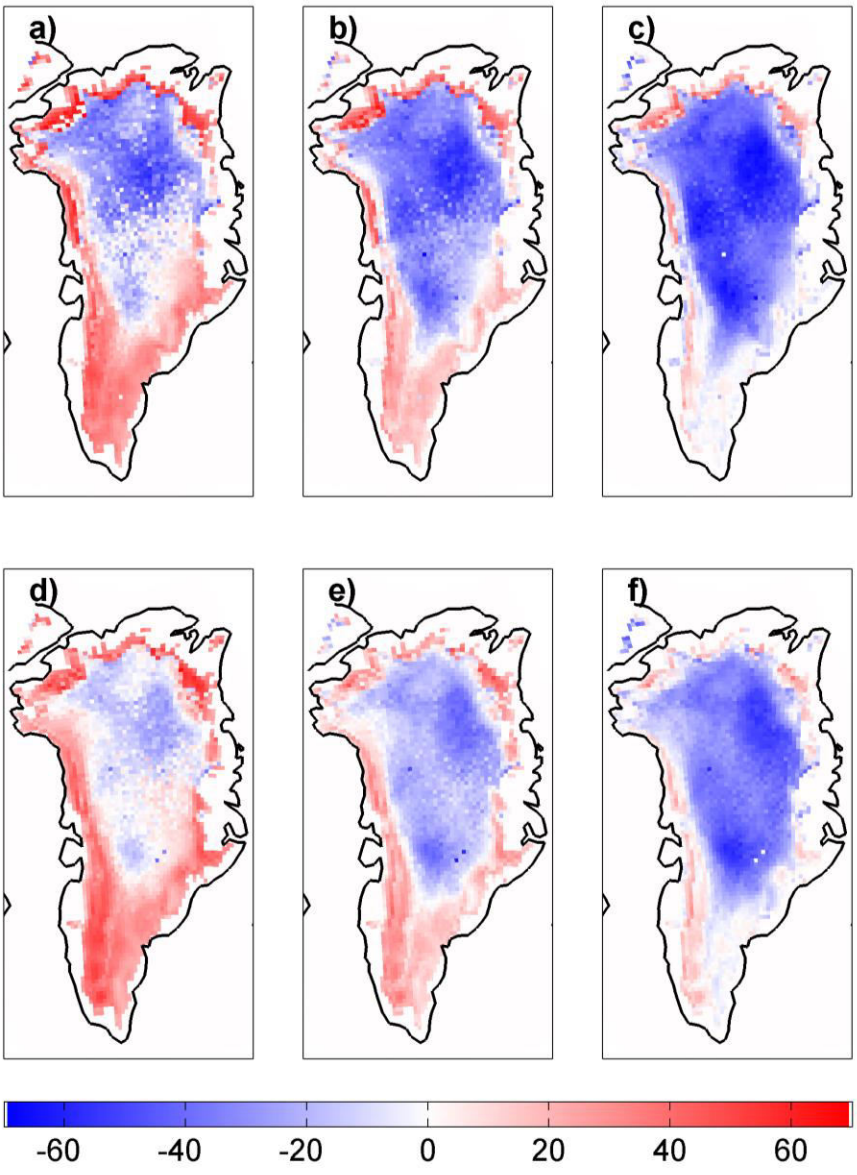

Figure 4.6 the same as Figure 4.5 but for the bias in [K]

To further evaluate the effect of α, the grain size parameterization using a constant α value was replaced with a density depended α (i.e., Eq. 4.2) and MEMLS was integrated in time for the sample pixels. As shown in Figure 4.7 the predicted brightness temperature is very similar to that of the constant α with a value of 0.4. The α value obtained from (Eq. 4.2) ranges from 0 to 0.4 for an ice layer and a typical new snow layer with a density of 150 kg/m^3 respectively. However, note that the brightness temperature is an integrated value over the surface layers up to an unknown penetration depth. The results (Figure 4.7) show that the unknown penetration depth is more likely limited to the low-density layers which yields to an α value of about 0.4. It would be instructive to further investigate the reasons for the similarities between the results from a constant and density dependent α values. However, these similarities and correlation between the predicted brightness temperatures from two parameterizations of grain size might be an indication that density-dependent grain size parameterization is overly simplified and does not adequately represent the temporal variation of brightness temperature.

To the best of my knowledge, no study has been done to characterize the error and uncertainty of the CROCUS snow grain parameters. Thus, it should be emphasized that for the further application of CROCUS-MEMLS system (1) more efforts are needed to characterize error and potentially improve the estimates of grain size parameters; (2) a physically based α value should be developed to take into account the spatial and temporal variability of the grain size parameters using snow layer properties. Treating the α value as a random variable and

estimating that using a data assimilation scheme could be a potential solution for this issue.

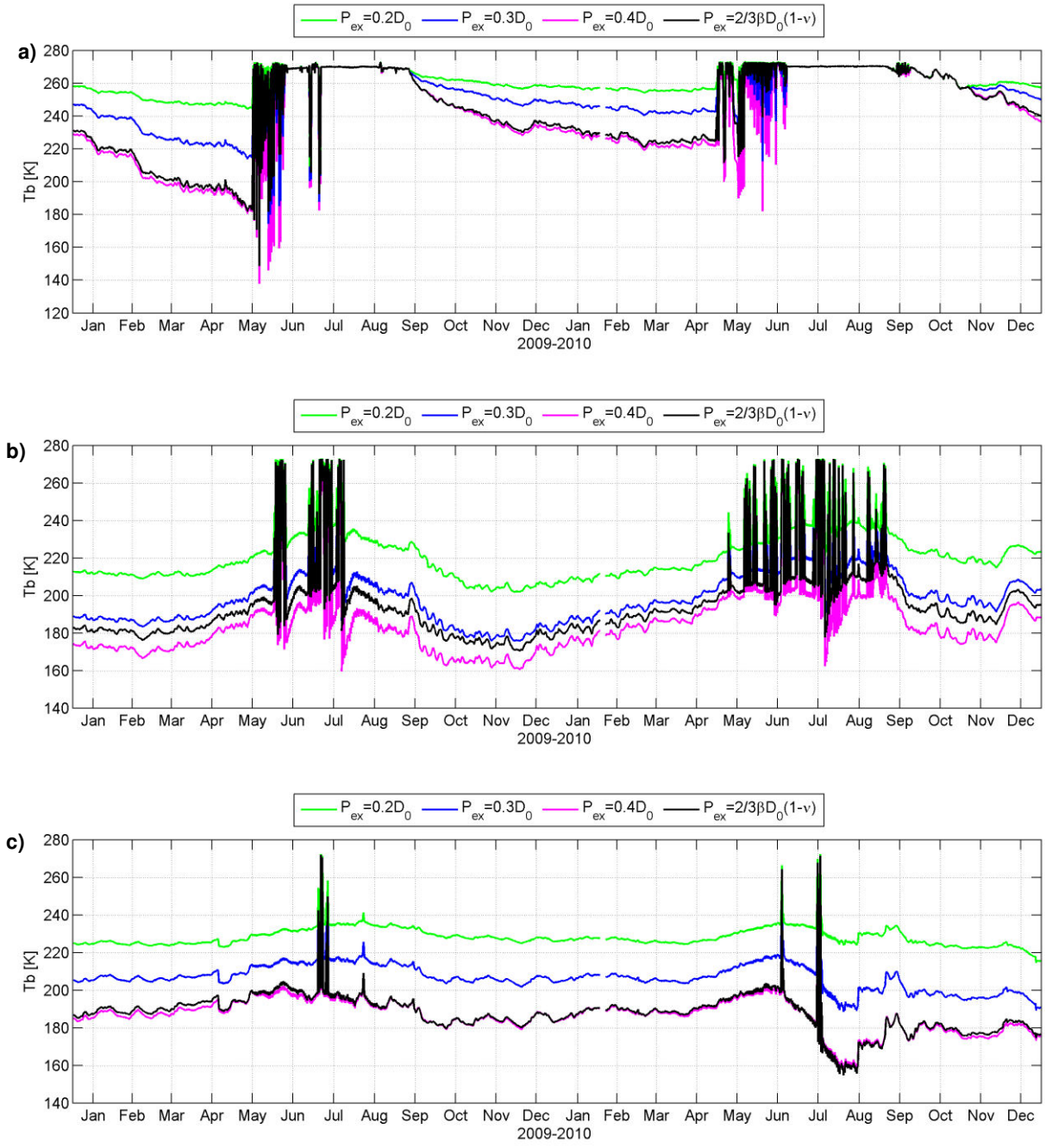

Figure 4.7 Time series of brightness temperatures at 36.5 GHz vertical polarization using a constant and a density depended α values, (a) for the JAR1 pixel, (b) for the Crawford pixel, (c) for the pixel X in the dry snow zone. The magenta, blue, green, and black lines represent the results for an α value of 0.2, 0.3, 0.4 and a density depended α value respectively.

4.4.2 Sensitivity analysis on layer density

The sensitivity of brightness temperature to snow density was investigated by repeating the baseline simulation (i.e., using snow profile from CROCUS outputs and a constant α value of 0.2 to compute the exponential correlation length) for different snow density. The snow layer density multiplied by a factor ranging from 0.75 to 1.25. Results show that for the sample pixel in the ablation zone the predicted brightness temperature does not change by changing the density of the shallow snowpack over the solid ice (Figure 4.8a). This is mainly due to the fact that the density of snowpack is about 150 kg/m^3 (Figure 4.2a) and by multiplying the density by a factor of 0.75 or 1.25 the total density does not change significantly to change the predicted brightness temperature. Therefore, it can be inferred that changes in the brightness temperature shown in Figure 4.2a are mainly due to changes in the exponential correlation length.

For the pixel in the percolation zone, there is a direct relationship between the density and brightness temperature (Figure 4.8b). An inspection of the time series of brightness temperature for several pixels in the percolation zone revealed that the sensitivity of the brightness temperature to the layer density is about 0.2 K per percentage increase in the layer density. Similar to the percolation zone, in the dry snow zone the brightness temperature increases with increasing density (Figure 4.8c). Similar inspection showed that the sensitivity of brightness temperature to density is about 0.2 K per percentage increase in the layer density, which is much smaller than the sensitivity of brightness temperature to exponential correlation length.

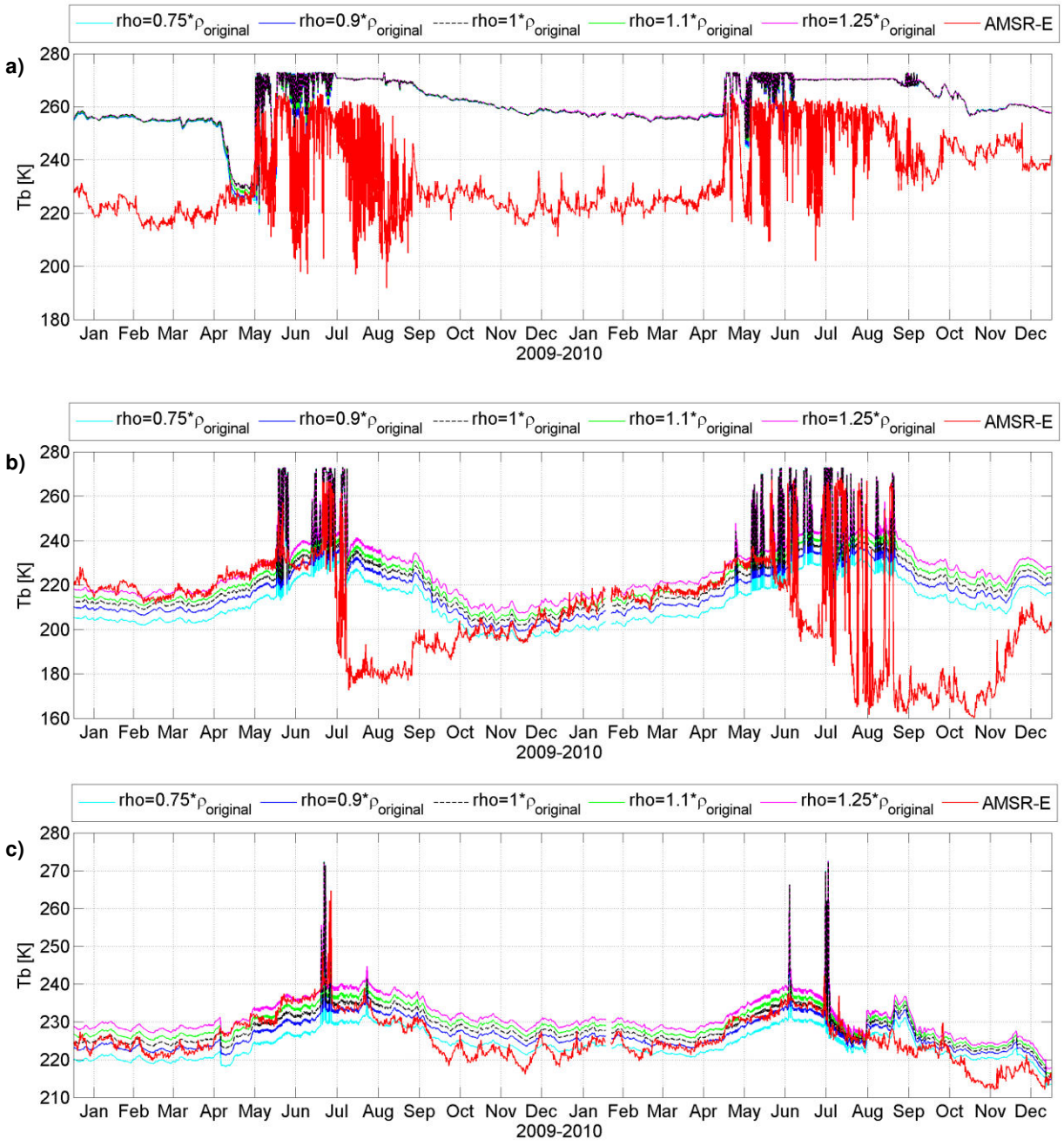

Figure 4.8 Sensitivity analysis on layer density using brightness temperature at 36.5 GHz vertical polarization, (a) for the JAR1 pixel, (b) for the Crawford pixel, (c) for the pixel X in the dry snow zone. The red line shows the measured brightness temperature, and the cyan, blue, black, green, and magenta lines show the predicted brightness temperature by multiplying the layers density by a factor of 0.75, 0.9, 1, 1.1, and 1.25 respectively and using a constant α value of 0.2.

4.4.3 The effect of sub-grid heterogeneity

Passive microwave brightness temperatures from AMSR-E are available at a spatial resolution of 25 km. The native spatial resolution (i.e., footprint) of these dataset depends on frequency and changes from about 5.4 km (89 GHz) to 56 km (6.9 GHz). Many studies (e.g., Kelly et al. 2003; Durand and Margulis 2006; De Lannoy et al., 2010) have highlighted that there are significant error and uncertainty in satellite-derived passive microwave brightness temperatures due to coarse spatial resolution of these datasets. However, it is very difficult to characterize the uncertainty of passive microwave brightness temperature due to the lack of availability of high-resolution dataset.

A comparison between high-resolution satellite-derived datasets like IST and albedo with coarse-resolution datasets (i.e., spatially aggregated data) could provide some insight about how aggregation can potentially introduce error and uncertainty into coarse-resolution passive microwave brightness temperature measurements. Here, high-resolution IST measurements were used to show the effect of sub-grid heterogeneity. Figure 4.9a-c shows fine resolution IST over the GrIS. A comparison between Figure 4.9b and Figure 4.9c shows that the variation of IST within a passive microwave resolution of 25 km is between 5-10 K. For the JAR1 and JAR2 stations the difference between the high-resolution IST temperature (Figure 4.9b) and aggregated IST at the co-located pixel (Figure 4.9c) is about 1-2 degree. A similar analogy can be made about aggregation of passive microwave brightness temperature at satellite sensors. Furthermore, IST data shows the sub-grid heterogeneity of the ice surface and does not provide any

information about subsurface heterogeneity while passive microwave can detect the vertical heterogeneity of the snowpack and measured brightness temperatures are an intergraded value that represents both the vertical and horizontal heterogeneity of the snowpack. This vertical heterogeneity makes the error structure of coarse-resolution passive microwave brightness temperature very complex. In general, it can be hypothesized that the valuable information of the passive microwave data that is directly related to the GrIS mass flux is lost through the aggregation at the sensor.

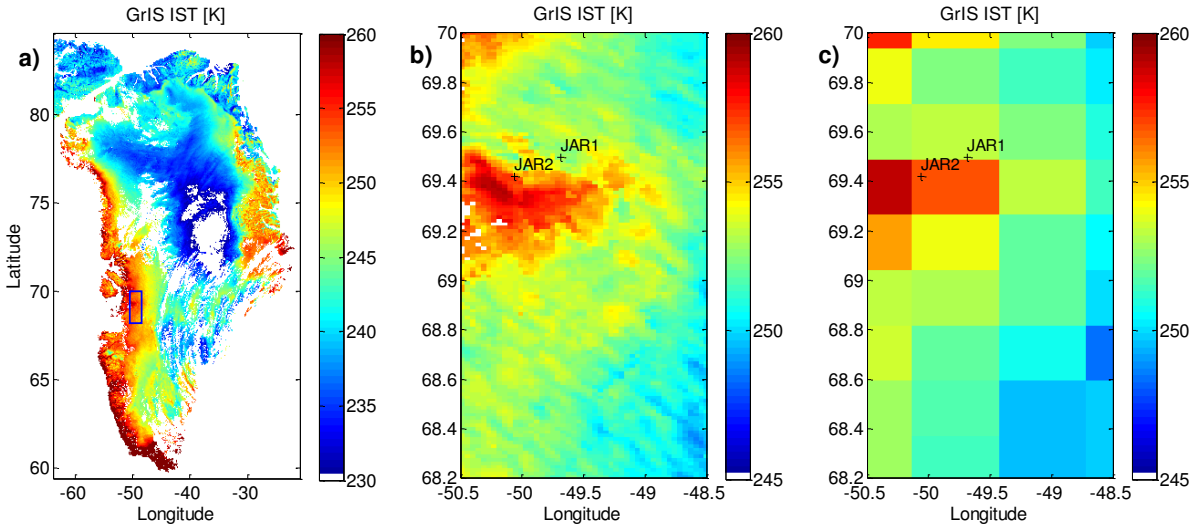

Figure 4.9 a) high-resolution IST for Feb 15, 2009, b) variation of IST in the rectangular area in (a)

4.4.4 Issues related to MAR snow profiles

MAR provides initial condition and forcing variables as inputs to the CROCUS snow model. Initial profile and forcing variables from the large-scale regional climate model are subject to errors and uncertainties. Different snow profiles were examined to detect possible errors in MAR outputs. The MAR issues are briefly summarized below.

Unusual first layer thickness and density: Figure 4.10a-b show the thickness and density of the first snow layer from MAR. As can be seen, the thickness of the first snow layer is very large and in some pixels it exceeds one meter. Similarly, the density of the first layer is about 300 kg/m^3. These issues can be mitigated by performing a model spin-up. A one-year model spin-up can effectively remove the anomalies observed in the first layer thickness and density. However, it is hard to know whether the snow profile is in a steady state condition after one-year spin-up or not. Predicted brightness temperatures from the CROCUS-MEMLS for sample pixels were closely investigated. The results show that, in some pixels in the dry snow zone, there is a large negative bias between the predicted and measured brightness temperatures at the beginning of the simulation. The bias gradually decreases over time and the predicted value moves toward the measured value. The reason why this occurs in the dry zone could be due to the fact that the snowpack in the dry zone has a longer memory than the other two zones. In the ablation zone, the snowpack memory resets every year after the snowpack completely melts. In the percolation zone, during the melt period, liquid water could obscure the microwave signal emitted from deep and old layers (i.e., no memory effect). During the dry period ice layers and layers with higher density could potentially reduce the penetration depth and the influences of the older snow layers from previous snow seasons. Over the dry zone, the penetration depth of the 37GHz channel reaches to more than one meter for a typical snowpack (i.e., T=270 K, ρ=300kg/m^3, P_{ex}=0.3 mm) (Matzler 2006). Therefore, snow layers from the previous snow seasons, which come from MAR through the initial condition, could influence the microwave signals. Note that inspection

of snow profile for several pixels in the dry snow zone show that the average accumulation rate during 2009-2010 is ~0.5 m/year (see Figure 4.4c). Over time, accumulation of new snow reduces the impact of old layers and gradually resets the memory of the snowpack.

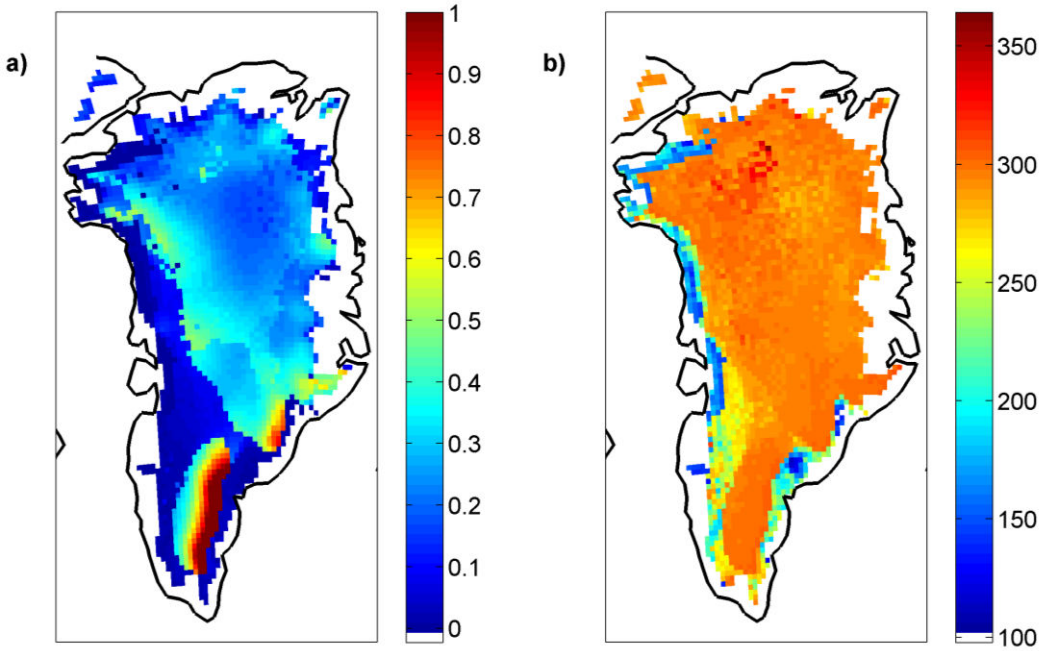

Figure 4.10 a) MAR surface layer thickness in [m], and b) MAR surface layer density in [kg/m^3]

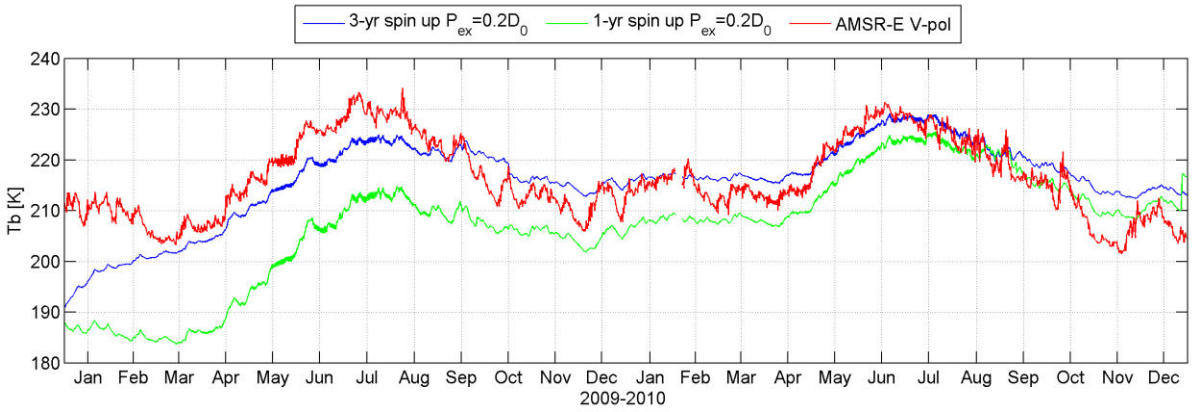

Figure 4.11 Predicted and measured brightness temperatures at 36.5 GHz vertical polarization at the Summit pixel, The red line show the measured brightness temperature and the green and blue lines show the predicted brightness temperature for 1-year and 3-yr spin-up period using an α value of 0.2.

A simple experiment was conducted to explore the effect of the duration of spin-up on the predicted brightness temperature. As stated before, for all simulations, a one-year spin-up was performed to eliminate the anomalies of the layer thickness and layer density from MAR. However, it appears that in some cases a one-year spin-up is not enough to reach the quasi-steady state condition; hence, the spin-up period was increased to 3 years. Figure 4.11 compares the effect of one-year and three-year spin-up on predicted brightness temperature for the pixel that encompasses the Summit station (Figure 4.1). As can be seen, this extra step can reduce the bias and potentially improve the predicted brightness temperature. Figure 4.12 show the initial snow profile after a one-year and three-year spin-up period. As can be seen, the layer temperatures from both simulations are the same. Layer densities are similar in the top 1.7 meters but gradually diverge after that. Optical grain diameters from these two simulations are slightly different. These differences are likely to be responsible for the differences between the one-year and three-year spin-up cases. It is worth noting that while the three-year spin-up performs better than the one-year spin-up, especially in some pixels over the dry snow zone; the duration of spin-up is still an open question.

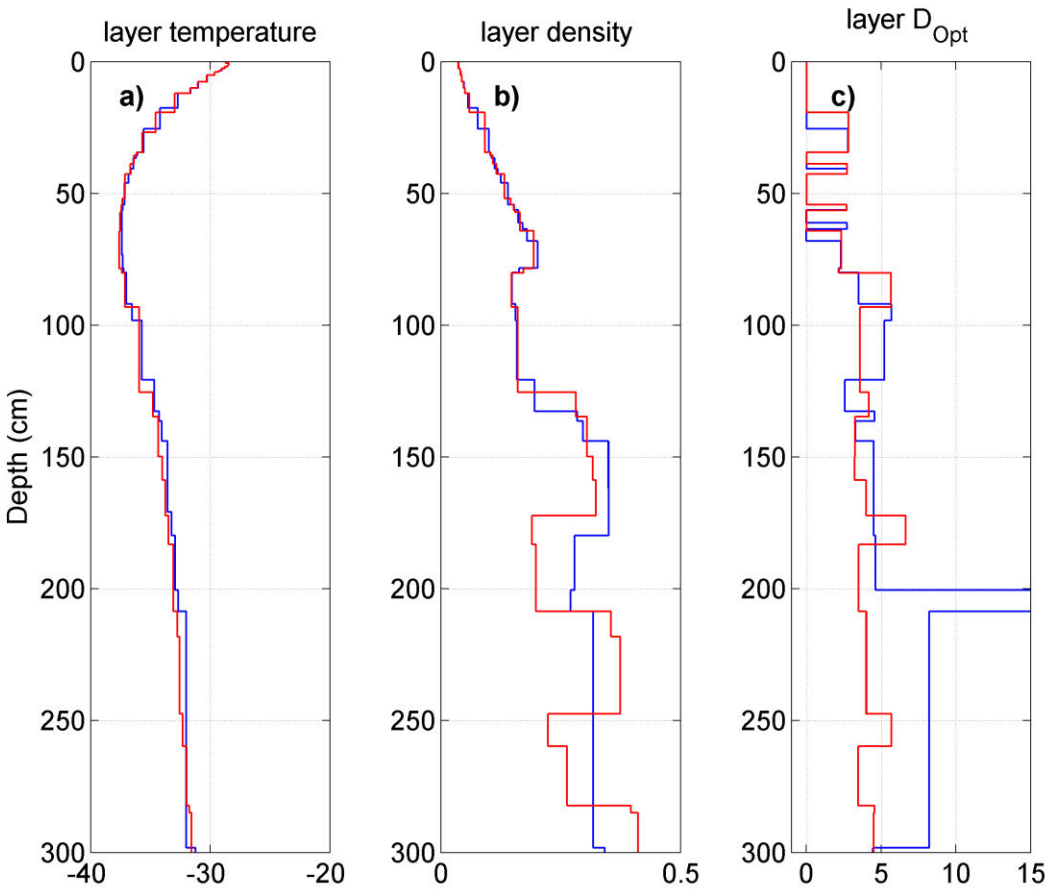

Figure 4.12 initial snow profile for the pixel that encompasses the Summit station. a) temperature in [ºC], b) density in [kg/m^3], and 3) optical grain diameter (D_{opt}) in [mm]. The blue and red lines represent the snow states for a one-year and a three-year period.

Uniform hourly precipitation rates: The MAR version 2 hourly precipitation contains an artifact whereby most precipitation values have a value of 1 mm/hr (Figure 4.13). This precipitation artifact might have a negative impact on albedo, brightness temperature, and mass and energy balance of the GrIS. A simple mitigation could be to compute the daily precipitation and apply that to a randomly selected hour of the corresponding day. Results from several sample pixels shown in Figure 4.14a-c. For the pixel in the ablation zone, there is no difference between the brightness temperatures from two different precipitation patterns. For the pixel in the

percolation and dry snow zones, daily precipitation leads to lower and higher brightness temperature during the accumulation season. These differences are likely due to 1) changes in layering structure because imposing daily precipitation in one hour forces the CROCUS to change the layer structure to accommodate new snow layers in one time step and 2) changes in precipitation pattern and consequently grain size parameters. However, it is very difficult to diagnose the main reason for these changes in brightness temperatures.

It seems that this precipitation pattern is an artifact in MAR version 2. Using real precipitation pattern would contribute to a better understanding of the optical behavior of surface layer (i.e., albedo and brightness temperature) which is highly influenced by snow grain size parameters.

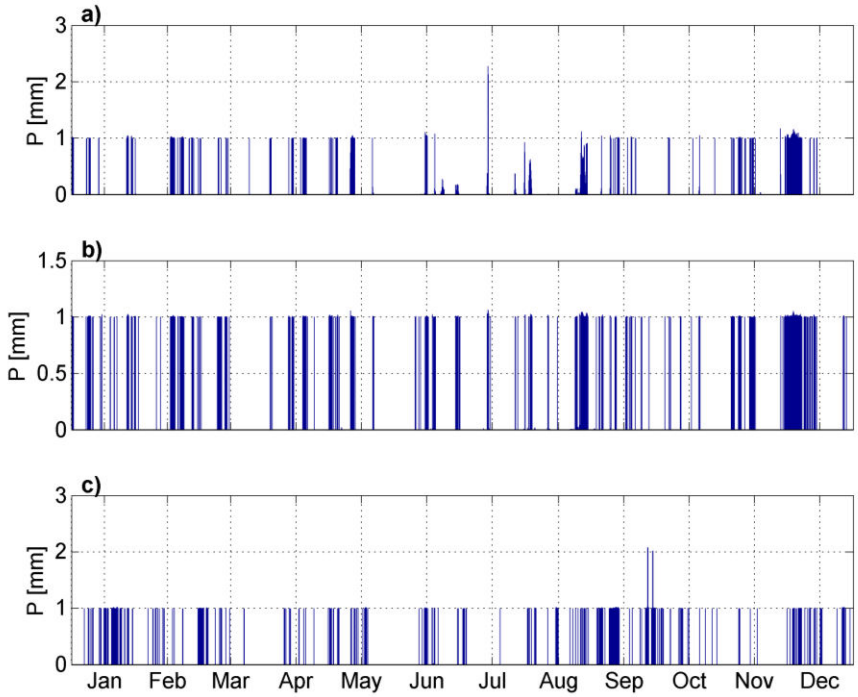

Figure 4.13: MAR hourly precipitation in [mm] for 2010, a) for the JAR1 pixel, b) for the Crawford pixel, c) for the pixel X.

Ice layer grain parameters: it seems that MAR uses relatively large values to describe the grain size of the ice layers (e.g. sphericity of 98[-] and grain size of 9.9 mm). The optical grain diameter obtained using these values is very large (i.e. 9.9 mm) (See Figure 4.2c). Such a large grain size has not been reported in the literature. The effect of this large optical grain size was investigated by replacing the exponential correlation length (which is the product of an α value of 0.2 times the optical grain diameter) with the maximum reported value of 0.71 mm (for coarsest grains) and 0.33 mm (for depth hoar) (e.g., Mätzler and Wiesmann 1999). There are no significant differences between the brightness temperatures by running MEMLS using these adjustments in the grain size for the sample pixels in each mass balance zone (Figure 4.15a-c). It could be due to the fact that the maximum reported value of 0.71 mm and 0.33 mm were used to replace the large exponential correlation length. However, MEMLS is very sensitive to grain size and caution must be taken in the future application of ice profile with such a large grain size.

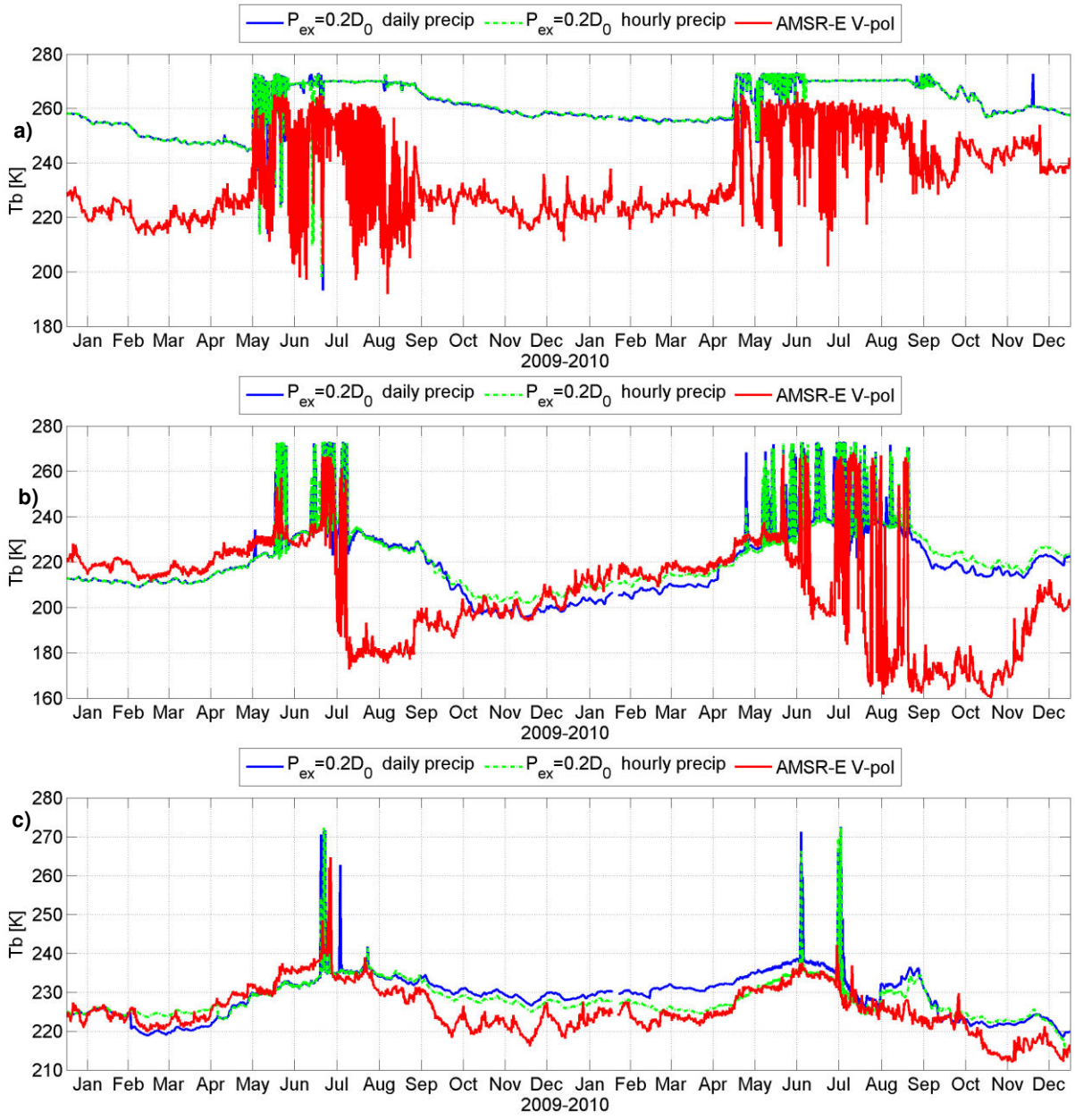

Figure 4.14 Comparison between the predicted brightness temperatures at 36.5 GHz vertical polarization using daily and hourly precipitation (a) for the JAR1 pixel (in the ablation zone), (b) for the Crawford pixel (in the percolation zone), and (c) the pixel X in the dry snow zone. The blue line shows the brightness temperature for the case that daily precipitation randomly assigned to one hour and the green line shows the results for the hourly precipitation (baseline simulation), and the red line shows the AMSR-E brightness temperature.

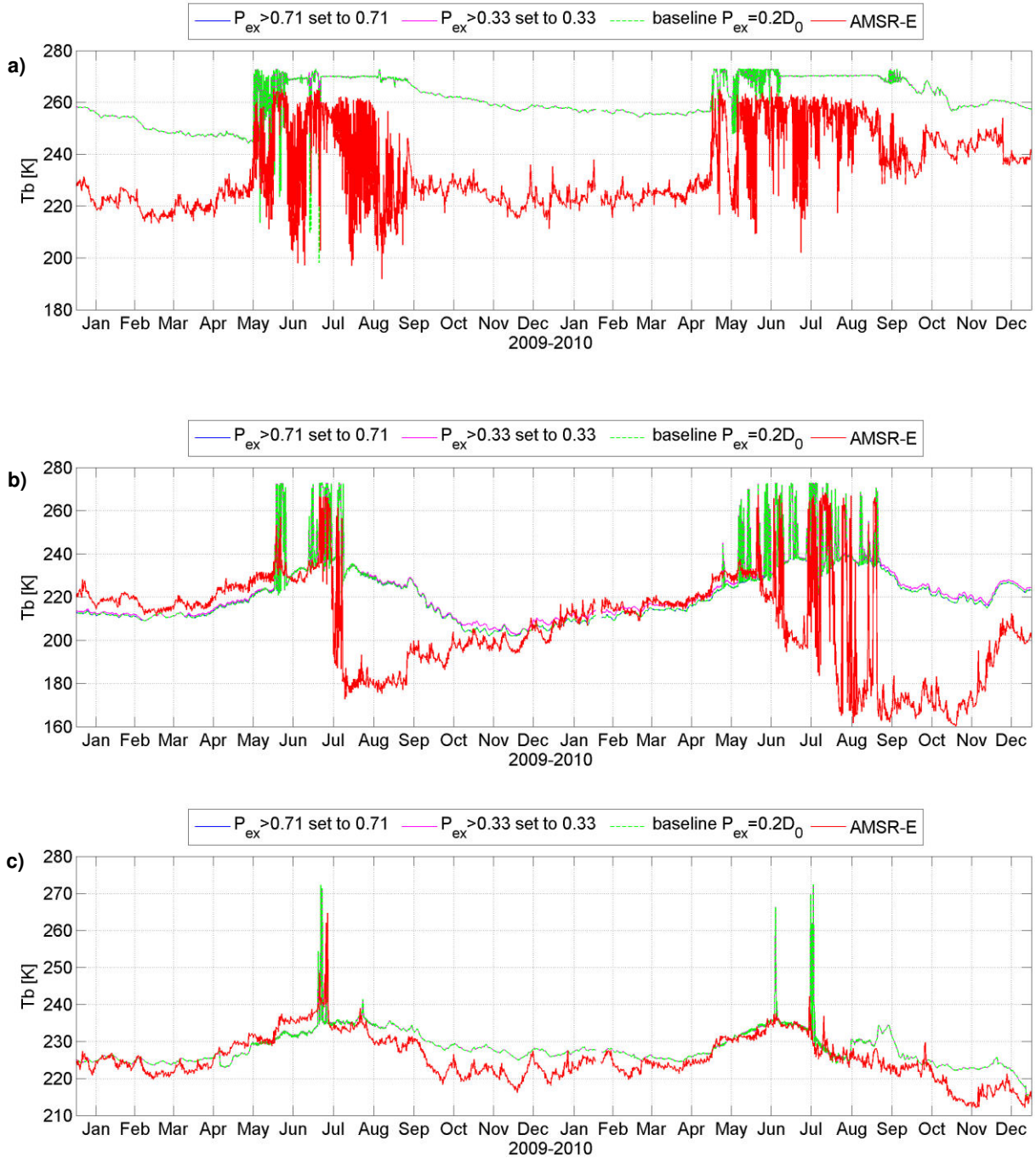

Figure 4.15 Comparison between the brightness temperature at 36.5 GHz vertical polarization by adjusting the ice layer grain size using an α value of 0.2 for different pixels (a) for the JAR1 pixel (in the ablation zone), (b) for the Crawford pixel (in the percolation zone), and (c) for the pixel X in the dry snow zone. The blue and magenta lines show the predicted brightness temperature for the cases that ice layer grain size have been adjusted to 0.71 mm and 0.33 mm and the green line shows the baseline simulation and the red line shows the measured brightness temperature from AMSR-E.

4.5 Summary

This chapter was an effort to briefly review the different applications of the passive microwave in the cryosphere and to understand the limitations associated with the application of passive microwave signals in a data assimilation framework. The main challenge in passive microwave radiance assimilation is the differences between the satellite-derived brightness temperatures and predicted brightness temperature using a measurement model (e.g., in this case, MEMLS). These errors and uncertainties come from different sources, for instance, errors in snow states from CROCUS can potentially degrade the predicted brightness temperatures. In addition, sub-grid heterogeneity is likely to be an important source of error in predicted brightness temperature which has not been properly investigated. Moreover, error in satellite-derived brightness temperatures (e.g., horizontal and vertical aggregation at satellite sensor) is another possibility for the differences between the measured and predicted brightness temperatures. Finally, error in grain size parameterization is another source of error in predicted brightness temperature that leads to the differences between the predicted and measured brightness temperatures. The sensitivity results showed that errors in the predicted brightness temperature are not a simple function of density and grain size, which can be reduced by adjusting the grain size parameters. The metamorphism mechanisms, especially during the melt period have a significant impact on the snowpack structure and snow properties. These changes cannot adequately be represented by the current parameterization of grain size (i.e., Eq. 4.2). While the accuracy of the grain size estimate needs to be improved the grain size

parameterization should also adequately represent the metamorphism mechanisms (i.e., change in layer structure, temporal and spatial variations of grain parameters). Furthermore, using passive microwave data in their native resolutions (i.e., footprint resolution) which are smaller than the EASE-Grid resolution for the 36.5 and 89 GHz channels could be a potential solution to reduce the error and uncertainty of the measured brightness temperature (e.g., Li et al., 2015a,b). Moreover, future investigation should also benefit from higher resolution RCM outputs to provide better estimates of snow profiles over the GrIS.

5 Conclusion and Future Work

5.1 Conclusion and original contribution

The three studies described above were conducted to: (1) examine the feasibility of improving a priori regional climate model estimates of the Greenland ice sheet (GrIS) surface mass loss through assimilation of synthetically generated ice surface temperatures; (2) apply the developed methodology using the satellite-derived ice surface temperature data to characterize the GrIS surface mass fluxes; (3) assess the possibility of extending the methodology to the passive microwave brightness temperature. This dissertation addresses the following overarching question: Can incorporation of remote sensing observations overcome significant uncertainties and biases in surface mass flux estimates from a regional climate model? A combination of pixel scale and spatially distributed experiments in the context of synthetic and real experiments were conducted to address this question.

In chapter 2, the performance of the proposed EnBS methodology was investigated within an OSSE framework using synthetically generated ice surface temperature measurements. Our analysis showed that error in forcing variables is responsible for most of the uncertainty in the GrIS surface mass fluxes. The EnBS reduces the uncertainty of the posterior estimates of forcing variables and effectively removes any of the prior biases. The information content in the ice surface temperature contributes an integrated sum of 452 ($MJ/m^2/year$), 375 ($MJ/m^2/year$), 14 (ºC-day), and 257 (ºC-day) to correct the shortwave, longwave, PPD, and NDD. Our findings showed that the data assimilation framework improves the RMSE of the posterior estimates of

runoff, sublimation/evaporation, surface condensation and surface mass loss fluxes by 61%, 64%, 76%, and 62%, respectively, over the nominal a priori climate model estimates.

In chapter 3, the satellite-derived ice surface temperature data was integrated into a priori snow/ice model estimates to generate reanalysis estimates of the GrIS surface mass fluxes. It was illustrated that the data assimilation framework removes both positive and negative biases in the prior estimates of the surface temperature. It was also showed that the posterior surface temperatures from the EnBS framework are in better agreement with the satellite–derived IST in comparison with the prior surface temperatures. Verification of snow state (i.e. surface temperature) is important and straightforward, but it is not sufficient. Verification of surface mass fluxes is a critical part of this study, but heavily limited by the lack of suitable verification datasets. The melt extent and melt duration from the AMSR-E data using the well-known DAV method were compared with the melt extent and melt duration from the prior and posterior simulation. While the time series of melt extent from AMSR-E are in agreement with the time series of the prior and posterior estimates of the melt extent from CROCUS, similarities between the prior and posterior estimates indicate that the melt extent and melt duration are bulk metrics and they are not adequate to assess the data assimilation results.

Pixel-scale surface mass balance estimates were also compared with the point scale in situ surface mass balance measurements (van de Wal et al., 2012) along the K-transect. The posterior estimate of the surface mass balance in the pixels that are co-located with the SHR and S10 stations are in good agreement with the point scale in situ measurements. But both the prior and

posterior simulations fail to properly estimate the SMB in the pixels that co-located with the S6, S7, and S8 stations. This is more likely due to the positive albedo feedback in these pixels, which are located in the GrIS dark zone. The presence of liquid water in different forms significantly decreases the albedo and enhances surface melt which is a possible reason for the difference between the predicted and measured SMB in the S9 station.

In chapter 4, CROCUS was coupled with MEMLS to evaluate the possibility of incorporation of passive microwave data into the developed algorithm. The measured brightness temperatures were compared with the predicted brightness temperatures for both the dry and melt periods. Significant bias and uncertainty between the predicted and measured values are from different sources including error in states variables from CROCUS, error due to sub-grid heterogeneity, error in satellite sensor, error in data processing operations, error in MEMLS physics and grain size parameterization. Characterizing error and uncertainty from all sources is important but, beyond the scope of this study. Here, uncertainty of predicted brightness temperatures due to error in snow states and grain size parameterization was investigated. It was found that, besides the error from above mentioned sources grain size parameterization is an important source of error in predicted brightness temperatures. It is especially important in the percolation zones where the metamorphism mechanisms significantly impact the snowpack structure. It was hypothesized that the current parameterization of the grain size in CROCUS-MEMLS system (i.e. Eq. 4.2) is unable to take into account the metamorphism mechanisms especially in the percolation zone. Further development of the exponential

correlation length should integrate the knowledge of the metamorphism processes into the current parameterization of grain size. Inconsistency between the predicted and measured brightness temperatures during the melt period in the ablation zone is another important issue that needs to be addressed. In the ablation zone, the role of grain size parameterization is minimal especially where bare ice is exposed and melting occurs from the bare ice. In this zone, the possible reason for the differences between the predicted and measured brightness temperatures is sub-grid heterogeneity. The coarse resolution of both satellite-derived measurements and predicted measurements are probably responsible for this inconsistency. Therefore, using techniques to downscale the measured brightness temperatures and also using high-resolution RCM outputs would contribute to reducing the differences between the predicted and measured brightness temperatures. In addition, snow layer density plays an important role in predicted brightness temperatures; accurate estimates of layer density would reduce the error and uncertainty of the predicted brightness temperatures.

In summary, it was shown that IST measurements contain valuable information that can be exploited by a data assimilation framework to improve the estimates of the GrIS surface mass loss. This study supports the conclusion that coarse resolution passive microwave brightness temperature with current grain size parameterization cannot be used in a data assimilation framework to improve the GrIS surface mass loss.

Several important caveats include: 1) clouds introduce error into IST measurements leading to errors in surface mass loss estimates. 2) It has been reported that IST measurements suffer

from cold bias. This bias could impact the posterior estimates of mass fluxes, especially during the melt season. 3) In the assimilation of IST, the predicted IST should be available at the measurement time. However, the acquisition time of the IST product is 17:00 ± 1:00 UTC. This 2-hour range would introduce uncertainties in the posterior estimates of the surface mass fluxes. These caveats highlight the need for future work to further develop the methodology and take advantage of the other relevant remotely sensed data.

5.2 Future work

Future work should focus on extending this methodology to generate a reanalysis surface mass balance of the GrIS. The steps in moving toward this goal include: 1) improving the CROCUS albedo and meltwater production schemes; 2) integrating other RS data such as albedo and radar altimetry data into the framework to further constrain the GrIS SML; 3) using other data assimilation techniques to further evaluate the information content of the IST measurements; 4) further evaluating the method using independent datasets including in situ measurements and airborne data; 5) generating a posteriori estimates of precipitation to provide a complete picture of the GrIS surface mass balance; 6) obtaining forcing variables from high-resolution regional climate models or downscaling the forcing variables to the scale of IST data (i.e. 1.5 km).

The modularity of data assimilation techniques makes it possible to combine nearly any land surface model with multi-scale, multi-resolution satellite-based or ground-based measurements. Therefore, extending the developed algorithm to extract the information content of other remote sensing data such as MODIS albedo, radar altimetry data, and Gravity Recovery and Climate

Experiment (GRACE) data would help to further constrain the GrIS SMB. Furthermore, the developed methodology can be used in other locations such as ice caps and high altitude glaciers to estimate different components of the mass balance (i.e. runoff, sublimation, evaporation, and condensation).

Bibliography

Abdalati, W. and Steffen, K.: Greenland ice sheet melt extent: 1979-1999, 106(D24), 983–988, 2001.

Abdalati, W. and Steffen, K.: Passive microwave derived snow melt regions on the Greenland Ice Sheet, Geophys. Res. Lett., 22(7), 787–790, 1995.

Abdalati, W. and Steffen, K.: Snowmelt on the Greenland Ice Sheet as Derived from Passive Microwave Satellite Data, J. Clim., 10(2), 165–175, 1997.

Alexander, P. M., Tedesco, M., Fettweis, X., van de Wal, R. S. W., Smeets, C. J. P. P. and van den Broeke, M. R.: Assessing spatio-temporal variability and trends (2000–2013) of modelled and measured Greenland ice sheet albedo, Cryosph. Discuss., 8, 3733–3783, doi:10.5194/tcd-8-3733-2014, 2014.

Al-Yaari, a., Wigneron, J.-P., Ducharne, a., Kerr, Y., de Rosnay, P., de Jeu, R., Govind, a., Al Bitar, a., Albergel, C., Muñoz-Sabater, J., Richaume, P. and Mialon, a.: Global-scale evaluation of two satellite-based passive microwave soil moisture datasets (SMOS and AMSR-E) with respect to Land Data Assimilation System estimates, Remote Sens. Environ., 149, 181–195, doi:10.1016/j.rse.2014.04.006, 2014.

Andreadis, K. M. and Lettenmaier, D. P.: Assimilating remotely sensed snow observations into a macroscale hydrology model, Adv. Water Resour., 29(6), 872–886, doi:10.1016/j.advwatres.2005.08.004, 2006.

Apgar, J. D., Ramage, J. M., McKenney, R. A. and Maltais, P., AMSR-E algorithm for snowmelt onset detection in sub-arctic heterogeneous terrain. Hydrol. Process., 21: 1587–1596. doi: 10.1002/hyp.6721, 2007.

Bamber, J. L. and Layberry, R. L.: 1 . Measurement , data reduction , and errors ice sheet was reestimated and found to have a value at a sample, J. Geophys. Res., 106(D24), 33773–33780, 2001.

Bateni and Entekhabi 2012

Bateni, S. M. and Entekhabi, D.: Surface heat flux estimation with the ensemble Kalman smoother: Joint estimation of state and parameters, Water Resour. Res., 48(8), 1–16, doi:10.1029/2011WR011542, 2012.

Bateni, S., Huang, C. and Margulis, S.: Feasibility of Characterizing Snowpack and the Freeze–Thaw State of Underlying Soil Using Multifrequency Active/Passive Microwave Data, , 51(7), 4085–4102, 2013.

Bateni, S., Margulis, S., Podest, E. and McDonald, K.: Characterizing Snowpack and the Freeze–Thaw State of Underlying Soil via Assimilation of Multifrequency Passive/Active Microwave Data: A Case Study (NASA CLPX 2003) , 53(1), 173–189 , 2015.

Biancamaria, S., Mognard, N. M., Boone, A., Grippa, M. and Josberger, E. G.: A satellite snow depth multi-year average derived from SSM/I for the high latitude regions, Remote Sens. Environ., 112(5), 2557–2568, doi:10.1016/j.rse.2007.12.002, 2008.

Box, J. E. and Steffen, K.: Sublimation on the Greenland ice sheet from automated weather station

observations, J. Geophys. Res., 106(D24), 33965–33981, doi:10.1029/2001JD900219, 2001.

Box, J. E., Bromwich, D. H., Veenhuis, B. a., Bai, L.-S., Stroeve, J. C., Rogers, J. C., Steffen, K., Haran, T. and Wang, S.-H.: Greenland Ice Sheet Surface Mass Balance Variability (1988–2004) from Calibrated Polar MM5 Output, J. Clim., 19(12), 2783–2800, doi:10.1175/JCLI3738.1, 2006.

Box, J. E., Fettweis, X., Stroeve, J. C., Tedesco, M., Hall, D. K. and Steffen, K.: Greenland ice sheet albedo feedback: thermodynamics and atmospheric drivers, Cryosph., 6(4), 821–839, doi:10.5194/tc-6-821-2012, 2012.

Box, J. E.: Greenland ice sheet surface mass balance 1991–2000: Application of Polar MM5 mesoscale model and in situ data, J. Geophys. Res., 109(D16), D16105, doi:10.1029/2003JD004451, 2004.

Braithwaite, R. J. and Olesen, O. B.: INCREASED ABLATION AT THE MARGIN OF THE GREENLAND, Ann. Glaciol. 14:20–22., 1990.

Brandt, O., Langley, K., Giannopoulos, A., Hamran, S. E. and Kohler, J.: Radar response of firn exposed to seasonal percolation, validation using cores and FDTD modeling, IEEE Trans. Geosci. Remote Sens., 47(8), 2773–2786, doi:10.1109/TGRS.2009.2016555, 2009.

Bromwich, H., Chen, Q., Bai, L. and Cassano, N.: Modeled precipitation over te Greenland ice sheet, J. Geophys. Res., 106, 891–908, 2001.

Brucker, L., Royer, a., Picard, G., Langlois, a. and Fily, M.: Hourly simulations of the microwave brightness temperature of seasonal snow in Quebec, Canada, using a coupled snow

evolution–emission model, Remote Sens. Environ., 115(8), 1966–1977, doi:10.1016/j.rse.2011.03.019, 2011.

Brun, B. E., Martin, E., Simon, V. and Gendre, C.: An energy and mass model of snow cover sidtable for operational avalanche forecasting, 35(12), 333–342, 1989.

Brun, E., David, P., Sudul, M. and Brunot, G.: A numerical model to simulate snow-cover stratigraphy for operational avalanche forecasting, J. Glaciol., 38(128), 13–22, 1992.

Burgers, G., Jan van Leeuwen, P. and Evensen, G.: Analysis Scheme in the Ensemble Kalman Filter, Mon. Weather Rev., 126(6), 1719–1724, doi:10.1175/1520-0493(1998)126<1719:ASITEK>2.0.CO;2, 1998.

Burgess, E. W., Forster, R. R., Box, J. E., Mosley-Thompson, E., Bromwich, D. H., Bales, R. C. and Smith, L. C.: A spatially calibrated model of annual accumulation rate on the Greenland Ice Sheet (1958–2007), J. Geophys. Res., 115(F2), F02004, doi:10.1029/2009JF001293, 2010.

Change, A.T.C, Foster, J.L, Hall, D. .: Nimbus-7 SMMR Derived Monthly Global Snow Cover and Snow Depth, Ann. Glaciol., 39–44, 1987.

Church, J. a. and White, N. J.: A 20th century acceleration in global sea-level rise, Geophys. Res. Lett., 33(1), n/a–n/a, doi:10.1029/2005GL024826, 2006.

Crow, W. T. and Ryu, D.: A new data assimilation approach for improving runoff prediction using remotely-sensed soil moisture retrievals, Hydrol. Earth Syst. Sci., 13(1), 1–16, doi:10.5194/hess-13-1-2009, 2009.

Crow, W. T. and Van Loon, E.: Impact of Incorrect Model Error Assumptions on the Sequential Assimilation of Remotely Sensed Surface Soil Moisture, J. Hydrometeorol., 7(3), 421–432, doi:10.1175/JHM499.1, 2006.

Cuffey, K. M., and Paterson. W. S. B.: The physics of glaciers, 4th edition, Academic Press, United States of America, 704pp, 2010.

De Lannoy, G. J. M., Reichle, R. H., Arsenault, K. R., Houser, P. R., Kumar, S., Verhoest, N. E. C. and Pauwels, V. R. N.: Multiscale assimilation of Advanced Microwave Scanning Radiometer–EOS snow water equivalent and Moderate Resolution Imaging Spectroradiometer snow cover fraction observations in northern Colorado, Water Resour. Res., 48(1), W01522, doi:10.1029/2011WR010588, 2012.

De Lannoy, G. J. M., Reichle, R. H., Houser, P. R., Arsenault, K. R., Verhoest, N. E. C. and Pauwels, V. R. N.: Satellite-Scale Snow Water Equivalent Assimilation into a High-Resolution Land Surface Model, J. Hydrometeorol., 11(2), 352–369, doi:10.1175/2009JHM1192.1, 2010.

Dee, D. P., Uppala, S. M., Simmons, a. J., Berrisford, P., Poli, P., Kobayashi, S., Andrae, U., Balmaseda, M. a., Balsamo, G., Bauer, P., Bechtold, P., Beljaars, a. C. M., van de Berg, L., Bidlot, J., Bormann, N., Delsol, C., Dragani, R., Fuentes, M., Geer, a. J., Haimberger, L., Healy, S. B., Hersbach, H., Hólm, E. V., Isaksen, L., Kållberg, P., Köhler, M., Matricardi, M., McNally, a. P., Monge-Sanz, B. M., Morcrette, J.-J., Park, B.-K., Peubey, C., de Rosnay, P., Tavolato, C., Thépaut, J.-N. and Vitart, F.: The ERA-Interim reanalysis: configuration and performance of the data assimilation system, Q. J. R. Meteorol. Soc., 137(656), 553–597, doi:10.1002/qj.828, 2011.

Dumont, M., Brun, E., Picard, G., Michou, M., Libois, Q., Petit, J.-R., Geyer, M., Morin, S. and Josse, B.: Contribution of light-absorbing impurities in snow to Greenland's darkening since 2009, Nat. Geosci., 7(7), 509–512, doi:10.1038/ngeo2180, 2014.

Dunne, S. and Entekhabi, D.: An ensemble-based reanalysis approach to land data assimilation, Water Resour. Res., 41(2), 1–18, doi:10.1029/2004WR003449, 2005.

Durand, M. and Margulis, S. a.: Correcting first-order errors in snow water equivalent estimates using a multifrequency, multiscale radiometric data assimilation scheme, J. Geophys. Res., 112(D13), 1–15, doi:10.1029/2006JD008067, 2007.

Durand, M. and Margulis, S. a.: Effects of uncertainty magnitude and accuracy on assimilation of multiscale measurements for snowpack characterization, J. Geophys. Res., 113(D2), 1–17, doi:10.1029/2007JD008662, 2008.

Durand, M. and Margulis, S.: Feasibility test of multifrequency radiometric data assimilation to estimate snow water equivalent, J. Hydrometeorol., 443–457, doi: http://dx.doi.org/10.1175/JHM502.1, 2006.

Durand, M., Kim, E. J. and Margulis, S. a.: Radiance assimilation shows promise for snowpack characterization, Geophys. Res. Lett., 36(2), 1–5, doi:10.1029/2008GL035214, 2009.

Durand, M., Kim, E. J., Member, S. and Margulis, S. A.: Quantifying Uncertainty in Modeling Snow Microwave Radiance for a Mountain Snowpack at the Point-Scale, Including Stratigraphic Effects, 46(6), 1753–1767, 2008.

Durand, M., Molotch, N. P. and Margulis, S. a.: A Bayesian approach to snow water equivalent

reconstruction, J. Geophys. Res., 113(D20), 1–15, doi:10.1029/2008JD009894, 2008.

Enderlin, E. M., Howat, I. M., Jeong, S., Noh, M.-J., van Angelen J. H., and van den Broeke, M. R.: An improved mass budget for the Greenland ice sheet. Geophys. Res. Lett., 41, 866–872, doi:10.1002/2013GL059010, 2014.

Ettema, J., van den Broeke, M. R., van Meijgaard, E., van de Berg, W. J., Bamber, J. L., Box, J. E. and Bales, R. C.: Higher surface mass balance of the Greenland ice sheet revealed by high-resolution climate modeling, Geophys. Res. Lett., 36(12), 1–5, doi:10.1029/2009GL038110, 2009.

Ettema, J., van den Broeke, M. R., van Meijgaard, E., van de Berg, W. J., Box, J. E. and Steffen, K.: Climate of the Greenland ice sheet using a high-resolution climate model – Part 1: Evaluation, Cryosph., 4(4), 511–527, doi:10.5194/tc-4-511-2010, 2010.

Evensen, G. : Data Assimilation: The Ensemble Kalman Filter, 2nd edition, Springer, 307pp, 2009.

Fettweis X. :Reconstruction of the 1979-2005 greenland ice sheet surface mass balance using satellite data and the regional climate model MAR, Ph.D. thesis, Universit´e catholique de Louvain, Leuven, Belgium, 2006.

Fettweis, X., Franco, B., Tedesco, M., van Angelen, J. H., Lenaerts, J. T. M., van den Broeke, M. R. and Gallée, H.: Estimating the Greenland ice sheet surface mass balance contribution to future sea level rise using the regional atmospheric climate model MAR, Cryosph., 7(2), 469–489, doi:10.5194/tc-7-469-2013, 2013.

Fettweis, X., Gallée, H., Lefebre, F. and Van Ypersele, J. P.: The 1988–2003 Greenland ice sheet melt extent using passive microwave satellite data and a regional climate model, Clim. Dyn., 27(5), 531–541, doi:10.1007/s00382-006-0150-8, 2006.

Fettweis, X., Gallée, H., Lefebre, F. and Ypersele, J.-P.: Greenland surface mass balance simulated by a regional climate model and comparison with satellite-derived data in 1990–1991, Clim. Dyn., 24(6), 623–640, doi:10.1007/s00382-005-0010-y, 2005.

Fettweis, X., Tedesco, M., van den Broeke, M. and Ettema, J.: Melting trends over the Greenland ice sheet (1958–2009) from spaceborne microwave data and regional climate models, Cryosph., 5(2), 359–375, doi:10.5194/tc-5-359-2011, 2011.

Fettweis, X., van Ypersele, J.-P., Gallée, H., Lefebre, F. and Lefebvre, W.: The 1979–2005 Greenland ice sheet melt extent from passive microwave data using an improved version of the melt retrieval XPGR algorithm, Geophys. Res. Lett., 34(5), 1–5, doi:10.1029/2006GL028787, 2007.

Fettweis, X.: Reconstruction of the 1979–2006 Greenland ice sheet surface mass balance using the regional climate model MAR, Cryosph. Discuss., 1(1), 123–168, doi:10.5194/tcd-1-123-2007, 2007.

Flanner, M. G. and Zender, C. S.: Linking snowpack microphysics and albedo evolution, J. Geophys. Res., 111(D12), D12208, doi:10.1029/2005JD006834, 2006.

Forman, B. a. and Margulis, S. a.: Assimilation of multiresolution radiation products into a downwelling surface radiation model: 1. Prior ensemble implementation, J. Geophys. Res.,

115(D22), 1–14, doi:10.1029/2010JD013920, 2010.

Forman, B. A., Reichle, R. H. and Rodell, M.: Assimilation of terrestrial water storage from GRACE in a snow-dominated basin, Water Resour. Res., 48(1), W01507, doi:10.1029/2011WR011239, 2012.

Foster, J. L., Sun, C., Walker, J. P., Kelly, R., Chang, A., Dong, J. and Powell, H.: Quantifying the uncertainty in passive microwave snow water equivalent observations, Remote Sens. Environ., 94(2), 187–203, doi:10.1016/j.rse.2004.09.012, 2005.

Franco, B., Fettweis, X. and Erpicum, M.: Future projections of the Greenland ice sheet energy balance driving the surface melt, Cryosph., 7(1), 1–18, doi:10.5194/tc-7-1-2013, 2013.

Franz, K. J., Hogue, T. S., Barik, M. and He, M.: Assessment of SWE data assimilation for ensemble streamflow predictions, J. Hydrol., 519, 2737–2746, doi:10.1016/j.jhydrol.2014.07.008, 2014.

Gallée, H. and Duynkerke, P.: Air-snow interactions and the surface energy and mass balance over the melting zone of west Greenland during the Greenland Ice Margin Experiment, J. Geophys. Res., 102(D12), 13813–13824, 1997.

Gallée, H. and Schayes, G.: Development of a Three-Dimensional Meso-γ Primitive Equation Model: Katabatic Winds Simulation in the Area of Terra Nova Bay, Antarctica, Mon. Weather Rev., 122(4), 671–685, doi:10.1175/1520-0493(1994)122<0671:DOATDM>2.0. CO;2, 1994.

Girotto, M., Cortés, G., Margulis, S. A. and Durand, M.: Examining spatial and temporal variability in snow water equivalent using a 27-year reanalysis: Kern River watershed, Sierra

Nevada, Water Resour. Res., 50(4), 446, doi:10.1002/2014WR015346, 2014.

Girotto, M., Margulis, S. and Durand, M.: Probabilistic SWE reanalysis as a generalization of deterministic SWE reconstruction techniques, Hydrol. Process., 28(12), 3875–3895, doi:10.1002/hyp.9887, 2014.

Goldberg, D. N. and Heimbach, P.: Parameter and state estimation with a time-dependent adjoint marine ice sheet model, Cryosph., 7(6), 1659–1678, doi:10.5194/tc-7-1659-2013, 2013.

Hall, D. K., Comiso, J. C., DiGirolamo, N. E., Shuman, C. a., Box, J. E. and Koenig, L. S.: Variability in the surface temperature and melt extent of the Greenland ice sheet from MODIS, Geophys. Res. Lett., 40(10), 2114–2120, doi:10.1002/grl.50240, 2013.

Hall, D. K., Comiso, J. C., Digirolamo, N. E., Shuman, C. a., Key, J. R. and Koenig, L. S.: A satellite-derived climate-quality data record of the clear-sky surface temperature of the Greenland ice sheet, J. Clim., 25(14), 4785–4798, doi:10.1175/JCLI-D-11-00365.1, 2012.

Hall, D. K., Nghiem, S. V., Schaaf, C. B., DiGirolamo, N. E. and Neumann, G.: Evaluation of surface and near-surface melt characteristics on the Greenland ice sheet using MODIS and QuikSCAT data, J. Geophys. Res., 114(F4), 1–13, doi:10.1029/2009JF001287, 2009.

Hall, D. K., Williams, R. S., Casey, K. a., DiGirolamo, N. E. and Wan, Z.: Satellite-derived, melt-season surface temperature of the Greenland Ice Sheet (2000–2005) and its relationship to mass balance, Geophys. Res. Lett., 33(11), L11501, doi:10.1029/2006GL026444, 2006.

Hall, D., Box, J., Casey, K., Hook, S., Shuman, C. and Steffen, K.: Comparison of satellite-derived and in-situ observations of ice and snow surface temperatures over Greenland, Remote Sens.

Environ., 112(10), 3739–3749, doi:10.1016/j.rse.2008.05.007, 2008.

Hamill, T. M.: Interpretation of Rank Histograms for Verifying Ensemble Forecasts, Mon. Weather Rev., 129(3), 550–560, doi:10.1175/1520-0493(2001)129<0550:IORHFV>2.0.CO;2, 2001.

Hanna, E. and Huybrechts, P.: Runoff and mass balance of the Greenland ice sheet: 1958–2003, J. Geophys. Res., 110(D13), 1–16, doi:10.1029/2004JD005641, 2005.

Hanna, E., Huybrechts, P., Cappelen, J., Steffen, K., Bales, R. C., Burgess, E., McConnell, J. R., Peder Steffensen, J., Van den Broeke, M., Wake, L., Bigg, G., Griffiths, M. and Savas, D.: Greenland Ice Sheet surface mass balance 1870 to 2010 based on Twentieth Century Reanalysis, and links with global climate forcing, J. Geophys. Res., 116(D24),121, doi:10.1029/2011JD016387, 2011.

Hanna, E., Jones, J. M., Cappelen, J., Mernild, S. H., Wood, L., Steffen, K. and Huybrechts, P.: The influence of North Atlantic atmospheric and oceanic forcing effects on 1900-2010 Greenland summer climate and ice melt/runoff, Int. J. Climatol., 33(4), 862–880, doi:10.1002/joc.3475, 2013.

Hansen, J., Sato, M., Hearty, P., Ruedy, R., Kelley, M., Masson-Delmotte, V., Russell, G., Tselioudis, G., Cao, J., Rignot, E., Velicogna, I., Kandiano, E., von Schuckmann, K., Kharecha, P., Legrande, A. N., Bauer, M., and Lo, K.-W.: Ice melt, sea level rise and superstorms: evidence from paleoclimate data, climate modeling, and modern observations that 2 °C global warming is highly dangerous, Atmos. Chem. Phys. Discuss., 15, 20059-20179, doi:10.5194/acpd-15-20059-2015, 2015.

Harper, J., Humphrey, N., Pfeffer, W. T., Brown, J. and Fettweis, X.: Greenland ice-sheet contribution to sea-level rise buffered by meltwater storage in firn., Nature, 491(7423), 240–3, doi:10.1038/nature11566, 2012.

Hook, S. and Vaughan, R.: in-flight validation of mid infrared and thermal infrared data from ASTER and MODIS on the Terra spacecraft using the Lake Tahoe, CA/NV, USA, automated validation, IEEE Trans. Geosci. Remote Sens, 45(6), 1798–1807, doi:10.1109/TGRS.2007.894564, 2007.

Huang, C., Li, X. and Lu, L.: Retrieving soil temperature profile by assimilating MODIS LST products with ensemble Kalman filter, Remote Sens. Environ., 112(4), 1320–1336, doi:10.1016/j.rse.2007.03.028, 2008.

Huang, C., Margulis, S. a., Durand, M. T. and Musselman, K. N.: Assessment of Snow Grain-Size Model and Stratigraphy Representation Impacts on Snow Radiance Assimilation: Forward Modeling Evaluation, IEEE Trans. Geosci. Remote Sens., 50(11), 4551–4564, doi:10.1109/TGRS.2012.2192480, 2012.

Intergovernmental Panel on Climate Change (IPCC) 2001, Third Assessment Report - Climate Change 2001, chapter 11: change in sea level.

Jansen, E., J. Overpeck, K.R. Briffa, J.-C. Duplessy, F. Joos, V. Masson-Delmotte, D. Olago, B. Otto-Bliesner, W.R. Peltier, S. Rahmstorf, R. Ramesh, D. Raynaud, D. Rind, O. Solomina, R. Villalba and D. Zhang, 2007: Palaeoclimate. In: Climate Change 2007: The Physical Science Basis. Contribution of Working Group I to the Fourth Assessment Report of the

Intergovernmental Panel on Climate Change [Solomon, S., D. Qin, M. Manning, Z. Chen, M. Marquis, K.B. Averyt, M. Tignor and H.L. Miller (eds.)]. Cambridge University Press, Cambridge, United Kingdom and New York, NY, USA.

Kelly, R. E., Chang, A. T., Tsang, L. and Foster, J. L.: A prototype AMSR-E global snow area and snow depth algorithm, IEEE Trans. Geosci. Remote Sens., 41(2 PART 1), 230–242, doi:10.1109/TGRS.2003.809118, 2003.

Key, J. R., Collins, J. B., Fowler, C., and Stone, R. S. :High-latitude surface temperature estimates from thermal satellite data. Remote Sens. Environ., 63, 302−309, 1997.

Key, J., & Haefliger, M. :Arctic ice surface temperature retrieval from AVHRR thermal channels. Journal of Geophysical Research, 97(D5), 5885−5893, 1992

Khan, S. a., Kjær, K. H., Bevis, M., Bamber, J. L., Wahr, J., Kjeldsen, K. K., Bjørk, A. a., Korsgaard, N. J., Stearns, L. a., van den Broeke, M. R., Liu, L., Larsen, N. K. and Muresan, I. S.: Sustained mass loss of the northeast Greenland ice sheet triggered by regional warming, Nat. Clim. Chang., 4(4), 292–299, doi:10.1038/nclimate2161, 2014.

Kokhanovsky, Alexander A., ed. Light Scattering Reviews, Vol. 6: Light Scattering and Remote Sensing of Atmosphere and Surface. Vol. 6. Springer Science & Business Media, 2011.

Krabill, W.: Greenland Ice Sheet: Increased coastal thinning, Geophys. Res. Lett., 31(24), 2–5, doi:10.1029/2004GL021533, 2004.

Larour, E., Utke, J., Csatho, B., Schenk, a., Seroussi, H., Morlighem, M., Rignot, E., Schlegel, N. and Khazendar, a.: Inferred basal friction and surface mass balance of the Northeast Greenland

Ice Stream using data assimilation of ICESat (Ice Cloud and land Elevation Satellite) surface altimetry and ISSM (Ice Sheet System Model), Cryosph., 8(6), 2335–2351, doi:10.5194/tc-8-2335-2014, 2014.

Lefebre, F., Fettweis, X., Gallée, H., Van Ypersele, J. P., Marbaix, P., Greuell, W. and Calanca, P.: Evaluation of a high-resolution regional climate simulation over Greenland, Clim. Dyn., 25(1), 99–116, doi:10.1007/s00382-005-0005-8, 2005.

Lefebre, F.: Modeling of snow and ice melt at ETH Camp (West Greenland): A study of surface albedo, J. Geophys. Res., 108(D8), 4231, doi:10.1029/2001JD001160, 2003.

Lei, L., Stauffer, D. R., Haupt, S. E. and Young, G. S.: A hybrid nudging-ensemble Kalman filter approach to data assimilation. Part I: application in the Lorenz system, Tellus A, 64, 1–14, doi:10.3402/tellusa.v64i0.18484, 2012.

Lenaerts, J. T. M., van den Broeke, M. R., van Angelen, J. H., van Meijgaard, E. and Déry, S. J.: Drifting snow climate of the Greenland ice sheet: a study with a regional climate model, Cryosph., 6(4), 891–899, doi:10.5194/tc-6-891-2012, 2012.

Lewis, S. and Smith, L.: Hydrologic drainage of the Greenland ice sheet, Hydrol. Process., 2011(May 2009), 2004–2011, doi:10.1002/hyp, 2009.

Li, D., Durand, M. and Margulis, S. A.: Large-Scale High-Resolution Modeling of Microwave Radiance of a Deep Maritime Alpine Snowpack, , 53(5), 2308–2322, 2015.

Li, D., Durand, M. and Margulis, S. a.: Potential for hydrologic characterization of deep mountain snowpack via passive microwave remote sensing in the Kern River basin, Sierra Nevada, USA,

Remote Sens. Environ., 125, 34–48, doi:10.1016/j.rse.2012.06.027, 2012.

Li, D., Durand, M. and Margulis, S. A.: Quantifying Spatiotemporal Variability of Controls on Microwave Emission From Snow-Covered Mountainous Regions, IEEE J. Sel. Top. Appl. Earth Obs. Remote Sens., 1–11, doi:10.1109/JSTARS.2015.2440332, 2015.

Löwe, H. and Picard, G.: Microwave scattering coefficient of snow in MEMLS and DMRT-ML revisited: the relevance of sticky hard spheres and tomography-based estimates of stickiness, Cryosph. Discuss., 9(2), 2495–2542, doi:10.5194/tcd-9-2495-2015, 2015.

Maätzler, C.: Relation between grain-size and correlation length of snow, J. Glaciol., 48(162), 461–466, doi:10.3189/172756502781831287, 2002.

Margulis, S. a., Girotto, M., Cortés, G. and Durand, M.: A Particle Batch Smoother Approach to Snow Water Equivalent Estimation, J. Hydrometeorol., 150504130725006, doi:10.1175/JHM-D-14-0177.1, 2015.

Margulis, S. a., McLaughlin, D., Entekhabi, D. and Dunne, S.: Land data assimilation and estimation of soil moisture using measurements from the Southern Great Plains 1997 Field Experiment, Water Resour. Res., 38(12), 35–1–35–18, doi:10.1029/2001WR001114, 2002.

Matzler, C. :Microwave Properties of Ice and Snow, in Solar System Ices, edited by B. Schmitt et al., Astrophys. and Space Sci. Library, Vol. 227 ~Kluwer Academic Publishers, Dordrecht, pp. 241–257, 1998

Mätzler, C. and Wiesmann, A.: Extension of the microwave emission model of layered snowpacks to coarse-grained snow, Remote Sens. Environ., 70(3), 317–325,

doi:10.1016/S0034-4257(99)00047-4, 1999.

Matzler, C.: Microwave permittivity of dry snow, IEEE Trans. Geosci. Remote Sens., 34(2), 573–581, doi:10.1109/36.485133, 1996.

Mätzler, Christian. Thermal microwave radiation: applications for remote sensing. Vol. 52. Iet, 2006

Monahan, P. a. and Ramage, J.: AMSR-E melt patterns on the Southern Patagonia Icefield, J. Glaciol., 56(198), 699–708, doi:10.3189/002214310793146197, 2010.

Morlighem, M., Seroussi, H., Larour, E. and Rignot, E.: Inversion of basal friction in Antarctica using exact and incomplete adjoints of a higher-order model, J. Geophys. Res. Earth Surf., 118(3), 1746–1753, doi:10.1002/jgrf.20125, 2013.

Mote, T. L., and M. R. Anderson,: Variations in snowpack melt on the Greenland ice sheet based on passive microwave-measurements. J. Glaciol., 41, 51–60, 1995.

Navari, M., Margulis, S. A., Bateni, S. M., Tedesco, M., Alexander, P., and Fettweis, X.: Improving a priori regional climate model estimates of Greenland ice sheet surface mass loss through assimilation of measured ice surface temperatures, The Cryosphere Discuss., 9, 3205-3255, doi:10.5194/tcd-9-3205-2015, 2015

Nghiem, S. V., Hall, D. K., Mote, T. L., Tedesco, M., Albert, M. R., Keegan, K., Shuman, C. a., DiGirolamo, N. E. and Neumann, G.: The extreme melt across the Greenland ice sheet in 2012, Geophys. Res. Lett., 39(20), 1–6, doi:10.1029/2012GL053611, 2012.

Peña, S. De, Howat, I. M., Nienow, P. W., Broeke, M. R. Van Den, Price, S. F., Mair, D., Noël, B. and Sole, A. J.: Changes in the firn structure of the western Greenland Ice Sheet caused by recent warming, , 1203–1211, doi:10.5194/tc-9-1203-2015, 2015.

Picard, G., Brucker, L., Roy, a., Dupont, F., Fily, M., Royer, a. and Harlow, C.: Simulation of the microwave emission of multi-layered snowpacks using the Dense Media Radiative transfer theory: the DMRT-ML model, Geosci. Model Dev., 6(4), 1061–1078, doi:10.5194/gmd-6-1061-2013, 2013.

Pritchard, H. D., Arthern, R. J., Vaughan, D. G. and Edwards, L. a: Extensive dynamic thinning on the margins of the Greenland and Antarctic ice sheets., Nature, 461(7266), 971–5, doi:10.1038/nature08471, 2009.

Qiu, Y. Q. Y., Shi, J. S. J., Jiang, L. J. L. and Mao, K. M. K.: Study of Atmospheric effects on AMSR-E microwave brightness temperature over Tibetan Plateau, 2007 IEEE Int. Geosci. Remote Sens. Symp., (90302008), 1873–1876, doi:10.1109/IGARSS.2007.4423189, 2007.

Rae, J. G. L., Aðalgeirsdóttir, G., Edwards, T. L., Fettweis, X., Gregory, J. M., Hewitt, H. T., Lowe, J. a., Lucas-Picher, P., Mottram, R. H., Payne, a. J., Ridley, J. K., Shannon, S. R., van de Berg, W. J., van de Wal, R. S. W. and van den Broeke, M. R.: Greenland ice sheet surface mass balance: evaluating simulations and making projections with regional climate models, Cryosph., 6(6), 1275–1294, doi:10.5194/tc-6-1275-2012, 2012.

Rahmstorf, S., Box, J. E., Feulner, G., Mann, M. E., Robinson, A., Rutherford, S. and Schaffernicht, E. J.: Exceptional twentieth-century slowdown in Atlantic Ocean overturning

circulation, Nat. Clim. Chang., 5(May), doi:10.1038/nclimate2554, 2015.

Ramage, J. M. and Isacks, B. L.: Interannual variations of snowmelt and refreeze timing on southeast-Alaskan icefields, U.S.A., J. Glaciol., 49, 102–116, doi:10.3189-172756503781830908, 2003.

Ramage, Joan M., and Bryan L. Isacks. "Determination of melt-onset and refreeze timing on southeast Alaskan icefields using SSM/I diurnal amplitude variations." Annals of Glaciology 34, no. 1: 391-398, 2002.

Reeh, B. N.: Parameterization of Melt Rate and Surfaee Temperature on the Greenland lee Sheet, Polarforschung 59,no.3, 113–128, 1991.

Rees, A., Lemmetyinen, J., Derksen, C., Pulliainen, J. and English, M.: Observed and modelled effects of ice lens formation on passive microwave brightness temperatures over snow covered tundra, Remote Sens. Environ., 114(1), 116–126, doi:10.1016/j.rse.2009.08.013, 2010.

Reichle, R. H., McLaughlin, D. B. and Entekhabi, D.: Hydrologic Data Assimilation with the Ensemble Kalman Filter, Mon. Weather Rev., 130(1), 103–114, doi:10.1175/1520-0493(2002)130<0103:HDAWTE>2.0.CO;2, 2002.

Rignot, E., Box, J. E., Burgess, E. and Hanna, E.: Mass balance of the Greenland ice sheet from 1958 to 2007, Geophys. Res. Lett., 35(20), L20502, doi:10.1029/2008GL035417, 2008.

Rignot, E., Koppes, M. and Velicogna, I.: Rapid submarine melting of the calving faces of West Greenland glaciers, Nat. Geosci., 3(3), 187–191, doi:10.1038/ngeo765, 2010.

Rignot, E., Velicogna, I., van den Broeke, M. R., Monaghan, a. and Lenaerts, J. T. M.: Acceleration of the contribution of the Greenland and Antarctic ice sheets to sea level rise, Geophys. Res. Lett., 38(5), n/a–n/a, doi:10.1029/2011GL046583, 2011.

Rignot, E., Velicogna, I., van den Broeke, M. R., Monaghan, a. and Lenaerts, J. T. M.: Acceleration of the contribution of the Greenland and Antarctic ice sheets to sea level rise, Geophys. Res. Lett., 38, L05503, doi:10.1029/2011GL046583, 2011.

Rosenfeld, S. and Grody, N.: Anomalous microwave spectra of snow cover observed from Special Sensor Microwave/Imager measurements, J. Geophys. Res., 105(Dll), 14913, doi:10.1029/1999JD900486, 2000.

Roy, A., Royer, A., St-Jean-Rondeau, O., Montpetit, B., Picard, G., Mavrovic, A., Marchand, N. and Langlois, A.: Microwave snow emission modeling uncertainties in boreal and subarctic environments, Cryosph. Discuss., 9(5), 5719–5773, doi:10.5194/tcd-9-5719-2015, 2015.

Schutz, B. E. "Spaceborne laser altimetry: 2001 and beyond." Book of Extended Abstracts, edited by: Plag, HP, WEGENER-98, Norwegian Mapping Authority, Honefoss, Norway, 1998.

Shuman, C. A., Hall, D. K., DiGirolamo, N. E., Mefford, T. K. and Schnaubelt, M. J.: Comparison of Near-Surface Air Temperatures and MODIS Ice-Surface Temperatures at Summit, Greenland (2008–13), J. Appl. Meteorol. Climatol., 53(9), 2171–2180, doi:10.1175/JAMC-D-14-0023.1, 2014.

Smith, L. C., Chu, V. W., Yang, K., Gleason, C. J., Pitcher, L. H., Rennermalm, A. K., Legleiter, C. J., Behar, A. E., Overstreet, B. T., Moustafa, S. E., Tedesco, M., Forster, R. R., LeWinter, A. L.,

Finnegan, D. C., Sheng, Y. and Balog, J.: Efficient meltwater drainage through supraglacial streams and rivers on the southwest Greenland ice sheet, Proc. Natl. Acad. Sci., 2000, 201413024, doi:10.1073/pnas.1413024112, 2015.

Steffen, K., Abdalati, W. and Stroeve, J.: Meteorology , and Atmospheric Physics Climate Sensitivity Studies of the Greenland Ice Sheet Using Satellite AVHRR , SMMR , SSM [I and In Situ Data, , 258, 239–258, 1993.

Straneo, F. and Heimbach, P.: North Atlantic warming and the retreat of Greenland's outlet glaciers., Nature, 504(7478), 36–43, doi:10.1038/nature12854, 2013.

Straneo, F. and Heimbach, P.: North Atlantic warming and the retreat of Greenland's outlet glaciers., Nature, 504(7478), 36–43, doi:10.1038/nature12854, 2013.

Tedesco, M. and Kim, E. J.: Intercomparison of Electromagnetic Models for Passive Microwave Remote Sensing of Snow, IEEE Trans. Geosci. Remote Sens., 44(10), 2654–2666, doi:10.1109/TGRS.2006.873182, 2006.

Tedesco, M. and Kokhanovsky, a. a.: The semi-analytical snow retrieval algorithm and its application to MODIS data, Remote Sens. Environ., 111(2-3), 228–241, doi:10.1016/j.rse.2007.02.036, 2007.

Tedesco, M., Fettweis, X., Mote, T., Wahr, J., Alexander, P., Box, J. E. and Wouters, B.: Evidence and analysis of 2012 Greenland records from spaceborne observations, a regional climate model and reanalysis data, Cryosph., 7(2), 615–630, doi:10.5194/tc-7-615-2013, 2013.

Tedesco, M., Fettweis, X., van den Broeke, M. R., van de Wal, R. S. W., Smeets, C. J. P. P., van de

Berg, W. J., Serreze, M. C. and Box, J. E.: The role of albedo and accumulation in the 2010 melting record in Greenland, Environ. Res. Lett., 6(1), 014005, doi:10.1088/1748-9326/6/1/014005, 2011.

Tedesco, M., Kim, E. J., England, A. W., De Roo, R. D. and Hardy, J. P.: Brightness Temperatures of Snow Melting/Refreezing Cycles: Observations and Modeling Using a Multilayer Dense Medium Theory-Based Model, IEEE Trans. Geosci. Remote Sens., 44(12), 3563–3573, doi:10.1109/TGRS.2006.881759, 2006.

Tedesco, M., Serreze, M. and Fettweis, X.: Diagnosing the extreme surface melt event over southwestern Greenland in 2007, Cryosph. Discuss., 2(3), 383–397, doi:10.5194/tcd-2-383-2008, 2008.

Tedesco, M.: Snowmelt detection over the Greenland ice sheet from SSM/I brightness temperature daily variations, Geophys. Res. Lett., 34(2), 1–6, doi:10.1029/2006GL028466, 2007.

Thomas, R. Frederick,m E, Krabill, W, Manizade, S, Martin, C, :Progressive increase in ice loss from Greenland, Geophysical Res. Letters, 33(10), pp.2-5, 2006.

Toure, A. M., Goïta, K., Royer, A., Kim, E. J., Durand, M., Margulis, S. A. and Lu, H.: A Case Study of Using a Multilayered Thermodynamical Snow Model for Radiance Assimilation, , 49(8), 2828–2837, 2011.

Van Angelen, J. H., Lenaerts, J. T. M., Lhermitte, S., Fettweis, X., Kuipers Munneke, P., van den Broeke, M. R., van Meijgaard, E. and Smeets, C. J. P. P.: Sensitivity of Greenland Ice Sheet surface mass balance to surface albedo parameterization: a study with a regional climate model,

Cryosph., 6(5), 1175–1186, doi:10.5194/tc-6-1175-2012, 2012.

Van Angelen, J. H., Lenaerts, J. T. M., Lhermitte, S., Fettweis, X., Kuipers Munneke, P., van den Broeke, M. R., van Meijgaard, E. and Smeets, C. J. P. P.: Sensitivity of Greenland Ice Sheet surface mass balance to surface albedo parameterization: a study with a regional climate model, Cryosph., 6(5), 1175–1186, doi:10.5194/tc-6-1175-2012, 2012.

Van de Wal, R. S. W., Boot, W., Smeets, C. J. P. P., Snellen, H., van den Broeke, M. R. and Oerlemans, J.: Twenty-one years of mass balance observations along the K-transect, West Greenland, Earth Syst. Sci. Data, 4(1), 31–35, doi:10.5194/essd-4-31-2012, 2012.

Van den Broeke, M., Bamber, J., Ettema, J., Rignot, E., Schrama, E., van de Berg, W. J., van Meijgaard, E., Velicogna, I. and Wouters, B.: Partitioning recent Greenland mass loss., Science, 326(5955), 984–6, doi:10.1126/science.1178176, 2009.

van den Broeke, M., Smeets, P. and Ettema, J.: Surface layer climate and turbulent exchange in the ablation zone of the west Greenland ice sheet, Int. J. Climatol., 29(15), 2309–2323, doi:10.1002/joc.1815, 2009.

van den Broeke, M., Smeets, P., Ettema, J., van der Veen, C., van de Wal, R. and Oerlemans, J.: Partitioning of melt energy and meltwater fluxes in the ablation zone of the west Greenland ice sheet, Cryosph., 2(2), 179–189, doi:10.5194/tc-2-179-2008, 2008.

VANDEWAL, R. and OERLEMANS, J.: An energy balance model for the Greenland ice sheet, Glob. Planet. Change, 9(1-2), 115–131, doi:10.1016/0921-8181(94)90011-6, 1994.

Vernon, C. L., Bamber, J. L., Box, J. E., van den Broeke, M. R., Fettweis, X., Hanna, E. and

Huybrechts, P.: Surface mass balance model intercomparison for the Greenland ice sheet, Cryosph., 7(2), 599–614, doi:10.5194/tc-7-599-2013, 2013.

Watson, C. S., White, N. J., Church, J. a., King, M. a., Burgette, R. J. and Legresy, B.: Unabated global mean sea-level rise over the satellite altimeter era, Nat. Clim. Chang., 5(May), 1–5, doi:10.1038/nclimate2635, 2015.

Wegmuller, U. and Matzler, C.: Rough bare soil reflectivity model, IEEE Trans. Geosci. Remote Sens., 37(3), 1391–1395, doi:10.1109/36.763303, 1999.

Wientjes, I. G. M., Van de Wal, R. S. W., Reichart, G. J., Sluijs, A. and Oerlemans, J.: Dust from the dark region in the western ablation zone of the Greenland ice sheet, Cryosph., 5(3), 589–601, doi:10.5194/tc-5-589-2011, 2011.

Wiesmann, A. and Mätzler, C.: Microwave Emission Model of Layered Snowpacks, Remote Sens. Environ., 70(3), 307–316, doi:10.1016/S0034-4257(99)00046-2, 1999.

Wouters, B., Bamber, J. L., van den Broeke, M. R., Lenaerts, J. T. M. and Sasgen, I.: Limits in detecting acceleration of ice sheet mass loss due to climate variability, Nat. Geosci., 6(8), 613–616, doi:10.1038/ngeo1874, 2013.

Xu, T., Liu, S., Liang, S. and Qin, J.: Improving Predictions of Water and Heat Fluxes by Assimilating MODIS Land Surface Temperature Products into the Common Land Model, J. Hydrometeorol., 12(2), 227–244, doi:10.1175/2010JHM1300.1, 2011.

Zhang, Y.-F., Hoar,T. J., Yang, Z.-L., Anderson, J. L., Toure, A. M. and Rodell, M.: Assimilation of MODIS snow cover through the Data Assimilation Research Testbed and the Community Land

Model version 4, J. Geophys. Res. Atmos., 119, 7091–7103, doi:10.1002/2013JD021329, 2014.